Journal of Advanced Ceramics
先进陶瓷
ISSN 2226-4108
CN 10-1154/TQ
清华大学出版社 Tsinghua University Press
SciOpen

J Adv Ceram 2026, **15**: 9221343

https://doi.org/10.26599/JAC.2026.9221343

Review

Transparent ferroelectric ceramics: From multifunctional coupling to optoelectronic integration

Yaqi Wang[1,†], Chengwu Li[1,†], Jianyi Liu[1], Zhiyan Chen[1], Yalin Qin[1,*] ,

Yongcheng Zhang[1,*],Shujun Zhang[2,*]

[1]*College of Physics, Qingdao University, Qingdao 266000, China*

[2]*Department of Chemistry, City University of Hong Kong, Hong Kong, China*

†These authors contributed equally to this work.

*Correspondence authors.

E-mail: Y. Qin, yalinqin@qdu.edu.cn;

Y. Zhang, qdzhyc@qdu.edu.cn;

S. Zhang, s.j.zhang@cityu.edu.hk

Received: April 24, 2026; Revised: June 15, 2026; Accepted: July 3, 2026

Abstract

The convergence of optics and electronics, driven by intelligent systems and wearable technologies, demands materials that seamlessly integrate optical transparency with robust electrical and mechanical functionalities. Transparent ferroelectric ceramics (TFCs) have emerged as a pivotal platform in this endeavor, uniquely bridging high optical transmittance with strong ferroelectric, piezoelectric, and electro-optic responses. This review comprehensively charts the evolution of TFCs, from fundamental material design to cutting-edge device applications. We systematically analyze the core strategies for achieving transparency in two representative transparent ferroelectric ceramic systems, namely lead-based $(Pb(Mg_{1/3}Nb_{2/3})O_3–PbTiO_3$, abbreviated as PMN–PT) and lead-free ($(K,Na)NbO_3$, abbreviated as KNN) systems), while also discussing other important systems such as $(Pb,La)(Zr,Ti)O_3$ (PLZT), $BaTiO_3$ (BTO), and $(Bi_{0.5}Na_{0.5})TiO_3$ (BNT) where appropriate for comparison. Critical mechanisms such as grain and domain engineering, refractive-index matching, phase-structure tuning, and defect control. Representative functionalities—including transparent piezoelectricity, electro-optic modulation, energy storage, photoluminescence, and photochromism—are highlighted, with their potential applications evaluated across photoacoustic imaging, adaptive optics, transparent robotics, smart windows, and optical communication. Finally, we identify key challenges and future opportunities, such as high Curie temperature (T_c) design, texture engineering, and multifunctional co-integration. Overall, this review aims to provide theoretical insights and material-design foundations for next-generation multifunctional transparent ferroelectric devices, accelerating their adoption in intelligent sensing, integrated photonics, and transparent optoelectronic systems.

Keywords: transparent ferroelectric ceramics; piezoelectricity; electro-optic; energy storage; luminescence; photochromism

1. Introduction

As a type of functional material that can couple electrical and mechanical performances, the ferroelectric ceramics have been accelerated in fields of electronics, optoelectronics, sensing, energy and communication, since their emergence at the beginning of 1920s [1-6]. Due to their outstanding performance in key properties such as ferroelectricity, piezoelectric effect and electro-optic response, ferroelectric ceramics have become an important foundation for the development of modern electronic and optoelectronic technologies. As technology advances, ferroelectric ceramics are gradually evolving from a single-function material with electrical-mechanical coupling to a multi-field coupling-responsive multifunctional material, making them indispensable for modern microelectronic and optoelectronic technologies. Meanwhile, as the application boundaries continue to expand, in emerging fields such as flexible electronics and wearable sensors, ferroelectric ceramics also demonstrate broad application prospects, where their thin-filmization and flexible characteristics are giving rise to a series of innovative devices [7-10].

1.1. Traditional Ferroelectric Ceramics and Their Representative Applications

Ferroelectric ceramics such as $BaTiO_3$ (BTO), $Pb(Zr,Ti)O_3$ (PZT), $Pb(Mg_{1/3}Nb_{2/3})O_3$–$PbTiO_3$ (PMN–PT), $(Bi,Na)TiO_3$ (BNT) and $(K,Na)NbO_3$ (KNN) are widely used in high-performance capacitors, infrared detectors, ultrasonic transducers, microelectromechanical systems (MEMS) and resonators due to their high dielectric permittivity, large remanent polarization, strong piezoelectric response, high electromechanical conversion efficiency, and large field-induced strain [11-17]. In numerous technical systems such as wireless communication networks, medical imaging, and intelligent control, ferroelectric ceramics serve as reliable and sensitive components that ensure stable operation. Furthermore, as the degree of integration continues to increase, the durability and thermal stability of conventional ceramics have been validated and optimized for miniaturized and high-frequency applications [18-20].

1.2. Emerging Transparent Ferroelectric Ceramics: Motivation and Prospects

Optical transparency is a key enabler for multiphysical-field coupling involving light, electricity,

and mechanical force in ferroelectric ceramics. It not only plays an important role in traditional fields such as optical windows and display panels, but also shows broad application potential in emerging scenarios, including intelligent sensing, transparent displays, high-speed optical communication, optical imaging, and next-generation lasers [5, 21-26]. However, although conventional ferroelectric ceramics perform well in electrical and mechanical aspects, their optical properties, especially the light transmission ability in the visible and near-infrared bands, have obvious limitations. Generally, the grain boundaries, pores, and other microstructural defects in ceramics act as dense scattering centers, which induce strong scattering and absorption during light propagation [27], and thereby limit their applications in optical displays, electro-optic modulators, and integrated photonic circuits. Therefore, achieving high optical transmittance while preserving original electrical properties is a central challenge for next-generation optoelectronic devices based on ferroelectric ceramics. Against this backdrop, transparent ferroelectric ceramics (TFCs) have emerged as a promising solution. Advanced fabrication methods, including hot isostatic pressing (HIP), hot-press sintering (HPS), atmosphere-controlled pressureless sintering, and two-step sintering, have been widely used to optimize grain size and distribution, increase densification, and reduce refractive-index mismatch and microdefects, thereby significantly reducing light scattering and absorption losses within the material [28-32].

Meanwhile, through precise microstructural design, dopant engineering, nanoscale modulation, and multi-physics field collaborative optimization, researchers have been constantly exploring the collaborative maintenance and compatibility strategies of optical transparency with ferroelectric, piezoelectric, and electro-optic functionalities [28, 33]. Recently, low-temperature sintering and composite designs have been developed in response to the demands for ultrafast optoelectronic response and flexible integration, expanding the application space of transparent ferroelectric ceramics.

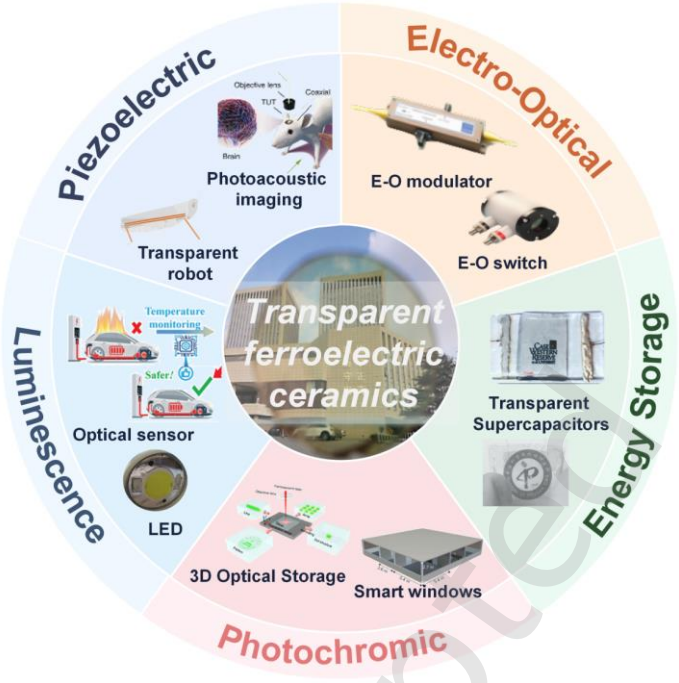

Fig. 1. The multifunctional coupling characteristics and diverse applications of transparent ferroelectric ceramics.

TFCs couple optical properties with mechanical, electrical, acoustic, and energy-storage performances, exhibiting promising potential for applications in several frontier fields, as illustrated in Fig. 1. (1) In optical communications, TFCs exhibit large electro-optic coefficient, low half-wave voltage, and fast response speed. These metrics enable high-speed electro-optic switches (nanosecond level), modulators, and filters used in fiber-optic links, laser modulation, and phased-array radar systems [34-37]. (2) For energy storage, ferroelectric ceramics are known for a high dielectric constant and strong breakdown strength. After achieving transparency, they retain high energy density and allow the design of transparent storage components [38-41]. Such capacitors could be integrated into future optoelectronic terminals to combine energy management and information display. (3) For biomedicine, these materials combine optical transparency with piezoelectricity to realize transparent piezoelectric transducers that assist in resolving the problem of the difficulty in coaxial alignment of light and sound in the new generation of photoacoustic imaging technology, meanwhile enhancing the imaging resolution, simplifying device design, and reducing the device size. It can also achieve simultaneous photoacoustic-ultrasonic-optical tri-modal imaging,

significantly improving the imaging quality and enhancing the comprehensiveness and accuracy of clinical diagnosis [42-49]. (4) For smart buildings, TFCs with excellent photochromic behavior and polarization response capability can regulate incident light flux via optoelectronic control, serving as key materials for smart windows and energy-efficient light-modulation systems [50-53]. (5) For optical sensing, their outstanding luminescent properties and optical response characteristics enable coupled sensing of multiple physical fields such as light, electricity, and temperature, demonstrating broad application prospects in scenarios like high-temperature safety alarms, smart displays, and biomedical monitoring [54-56]. In summary, TFCs have demonstrated great potential in the integration of multi-functional devices, opening up new directions for future optoelectronic fusion and intelligent applications.

1.3. Overview of Representative Transparent Ferroelectric Ceramic Systems

Current research on TFCs involves several material families, including the lead-based PMN–PT system, lead-free KNN system, and other systems such as $(Pb,La)(Zr,Ti)O_3$ (PLZT), BTO, and BNT-based compositions. Among them, PMN–PT and KNN have become two representative research lines because they correspond to typical lead-based and lead-free transparent ferroelectric ceramic platforms, respectively, and cover most of the major functional directions of TFCs, including piezoelectricity, electro-optic modulation, energy storage, photoluminescence, and photochromism. Each system shows distinct features in composition, crystal structure, processing route, and multifunctional coupling behavior. The following sections briefly summarize their defining characteristics.

PMN–PT ceramics are solid solutions of PMN and PT, and their phase structures and physical properties vary with composition and temperature. As shown in Fig. 2(a), with the variation of PT content and temperature, PMN–PT experiences multiple crystalline phases, including rhombohedral (R), rhombohedral–tetragonal (R–T) coexistence, and tetragonal (T) phases. Different crystalline phases often correspond to differentiated light transmittance and have a significant impact on

piezoelectric, electro-optic, and luminescent properties. Generally, excellent electro-optic performances often emerge when PT content below 25 mol% [5, 57-59], whereas components at the morphotropic phase boundary (MPB) with a PT content ranging from 28% to 32% tend to exhibit superior piezoelectric properties [58, 60-63]. Further, through appropriate rare-earth doping and auxiliary element modification, the crystal symmetry can be optimized, the grain size can be refined, and polar nanoregions (PNRs) are introduced, yielding transparent ceramics with high transmittance and strong multifunctional performance. For example, the introduction of rare earth elements such as La, Sm, and Pr can effectively regulate the phase boundary structure within PMN–PT, forming fine and uniform nanoscale ferroelectric domains, thereby enabling high optical transparency together with high electro-optical coefficient or piezoelectric response [58, 64-66].

Fig. 2(b) is a simple phase diagram of KNN, which is a representative lead-free ferroelectric system possessing a perovskite structure and good ferroelectric properties [67, 68]. However, conventionally sintered KNN ceramics typically exhibit semi-transparent behavior with limited optical transmittance [69]. Recently, transparent KNN has gradually achieved breakthroughs via hot-press sintering, rare-earth doping, and addition of sintering aids such as Li and Bi [33, 70]. During fabrication, grain-size refinement to below 200–300 nm and suppression of grain-boundary scattering are essential for improving optical transmittance. Meanwhile, phase-boundary regulation is also important for maintaining favorable piezoelectric performance. Unlike the composition-driven MPB in lead-based PMN–PT, the rhombohedral-orthorhombic (R–O) or orthorhombic–tetragonal (O–T) phase transition regions in KNN-based systems are temperature-dependent and named polymorphic phase boundary (PPB). Chemical modification can shift the polymorphic phase-transition temperatures, such as the rhombohedral–orthorhombic transition temperature ($T_{R–O}$) or orthorhombic–tetragonal transition temperature ($T_{O–T}$), toward room temperature, thereby facilitating polarization rotation and improving piezoelectric response. Therefore, by combining grain-size control, PPB regulation, and scattering suppression, the optical transmittance of KNN ceramics can

be significantly improved while preserving useful piezoelectric properties [28]. In addition, the KNN system also shows certain advantages in energy storage, photochromism and electro-optic regulation *etc*., offering new options for lead-free multifunctional ceramics [40, 71, 72]. Compared with PMN–PT, KNN is more in line with the requirements of green manufacturing due to its lead-free feature, but its piezoelectric and electro-optic performance still needs further optimization and improvement.

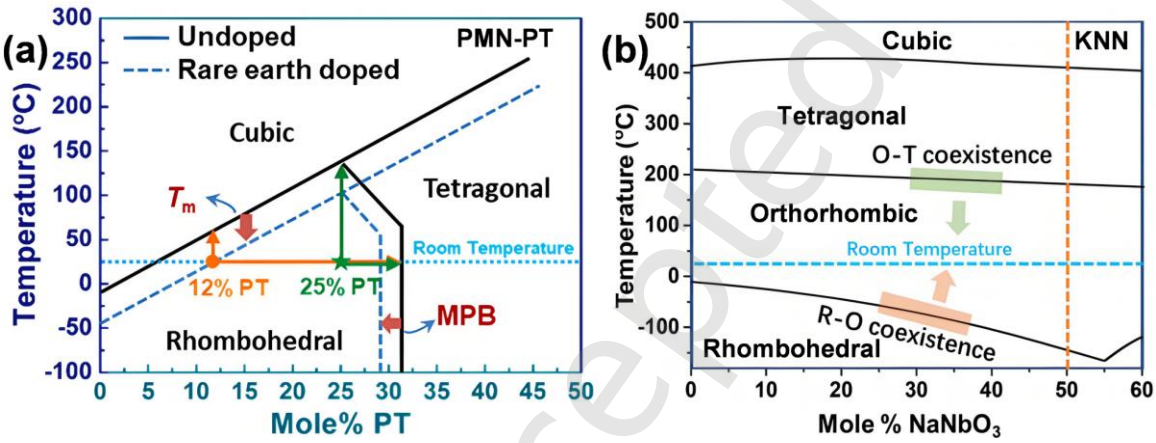

Fig. 2. (a) Phase diagram of PMN–PT ceramics. Reproduced with permission from Ref. [73], © Elsevier BV 2022. (b) Phase diagram of KNN ceramics.

Beyond PMN–PT and KNN, other candidates, including PLZT, BTO, and BNT, have also been investigated for the preparation of transparent ferroelectric ceramics. PLZT is a classical transparent electro-optic ceramic and remains an important benchmark for electro-optic modulation and optical device applications. BTO and BNT-based transparent ferroelectric ceramics have also been explored, especially for dielectric and energy-storage-related applications. However, compared with PMN–PT and KNN, the reported studies on these systems are relatively scattered, and many of them mainly focus on optical transmittance or basic dielectric behavior rather than systematic multifunctional coupling. Therefore, this review mainly uses PMN–PT and KNN as representative systems, while incorporating PLZT, BTO, BNT, and other related systems where appropriate for comparison and scope expansion[74-77].

In summary, conventional ferroelectric ceramics have performed well in electronic and

optoelectronic applications, but limited optical transparency still constrains their use in highly integrated optoelectronic devices. The emergence of transparent ferroelectric ceramics, together with recent design and processing innovations, enables the integration of traditional electrical functionalities with optical performance. Currently, both lead-based PMN–PT and lead-free KNN have made notable advances in structural design and processing, laying the groundwork for practical, high-performance transparent ferroelectric ceramics.

Looking ahead, key challenges remain: grain-boundary defect control, refractive-index matching, long-term stability evaluation, and scalable, low-cost manufacturing. For integrated devices, maintaining high transmittance while further enhancing ferroelectric, electro-optic, and piezoelectric properties will be pivotal for industrial adoption. Future work should therefore pursue multiscale structural tuning, diversification of material systems, advanced integration strategies, and application-driven design. Together with emerging nanomanufacturing and flexible-substrate technologies, transparent ferroelectric ceramics are poised to enable breakthrough applications in wearable optoelectronics, biosensing, and safety monitoring.

This review is structured to guide the reader from the foundational principles of TFCs to their frontier applications. We begin by deconstructing the core challenge: the intricate balance between transparency and functionality (**Section 2**). Here, we detail the optical loss mechanisms and the advanced processing and microstructural engineering strategies required to mitigate them. Subsequently, the review pivots to a functionality-centric analysis **(Section 3)**, providing a comprehensive survey of five key material classes: transparent piezoelectric, electro-optic, energy-storage, luminescent, and photochromic ceramics. For each, we dissect the underlying physics, chart the progress in both lead-based (PMN-PT) and lead-free (KNN) systems, and summarize performance benchmarks. The promise of TFCs is ultimately realized in devices. **Section 4** showcases this translational potential, presenting compelling proof-of-concept applications across biomedicine, robotics, adaptive optics, acoustics, information technology, and intelligent control.

Finally, **Section 5** synthesizes the current landscape, identifying persistent challenges in composition design, thermal stability, and process scalability, while outlining a forward-looking roadmap centered on intelligent design, texture engineering, and multifunctional integration.The structure of this review is outlined in Fig. 3. Our goal is to provide not only a detailed technical resource but also a strategic vision. We aim to illuminate how TFCs are evolving from laboratory curiosities into enabling components for the next generation of intelligent, interactive, and optically transparent technologies.

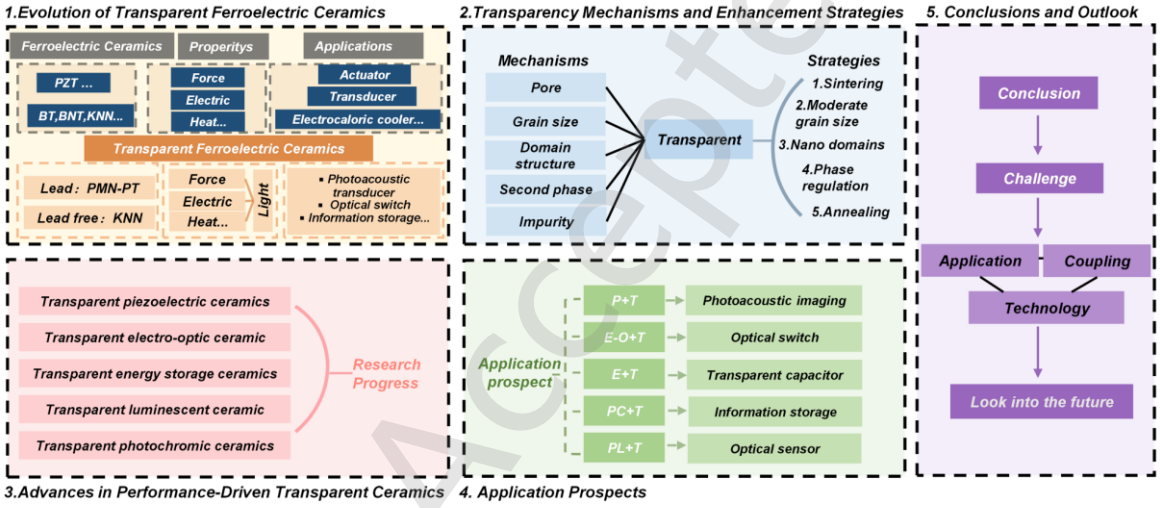

Fig. 3. Overall framework of this review.

2. Influencing Factors and Regulation Strategies for the Transparency

Achieving high optical transparency in inherently scattering polycrystalline ferroelectrics requires the coordinated suppression of multiple optical loss channels. This section dissects the fundamental mechanisms that govern light transmission and outlines the key material design and processing strategies developed to suppress optical losses while preserving functional properties.

2.1. Fundamental Mechanisms Controlling Optical Transparency

The optical transmittance of TFCs is not governed by a single factor, but by the combined effects of intrinsic material absorption, interfacial reflection, and microstructure-induced scattering [78, 79], as shown in Fig. 4(a). In a more intuitive sense, achieving high transparency requires the

synergistic reduction of absorption, reflection, and scattering losses caused by pores, grain boundaries, ferroelectric domains, and other microstructural defects. Different loss sources dominate at different wavelength ranges and structural length scales, and their coupling collectively governs macroscopic light-transmission behavior. Owing to the ubiquitous presence of multiscale microstructural features, their spatial distributions, orientation relationships, and coupling effects are highly complex. As a result, a unified transmittance model that can fully describe realistic microstructural conditions has not yet been established, and current understanding therefore remains incomplete.

For clarity, these optical loss contributions can be approximately decomposed under reasonable approximation conditions to establish a quantitative physical framework. By neglecting strong multiple-scattering coupling effects, the overall transmittance can be written as the combined contributions from absorption, reflection, and scattering processes, as expressed below [80]:

$$T = (1 - R_s)\exp[-(\gamma + \alpha) \cdot t] \quad (1)$$

where R_s represents reflection losses arising from sample surfaces and internal interfaces, α denotes the absorption coefficient, γ denotes the scattering coefficient associated with microstructural inhomogeneities, and t represents the sample thickness. This equation also indicates that transmittance depends on both wavelength and sample thickness. Scattering losses generally decrease at longer wavelengths, whereas absorption and scattering accumulate with increasing thickness. Therefore, the transmittance values summarized in this review should be compared together with their reported wavelength and thickness, and are used mainly to indicate material trends rather than strict one-to-one ranking. Based on this transmittance decomposition, the dominant physical mechanisms governing the optical transparency of ferroelectric ceramics are discussed separately in the following subsections, namely material absorption, interfacial reflection, and microstructure-induced scattering. It should be noted that Eq. (1) is a simplified decoupling approximation, in which R_s, α, and γ are treated as approximately separable effective loss terms. This

approximation is mainly applicable to room-temperature in-line transmittance measurements in the visible-to-near-infrared transparent window, where intrinsic absorption and multiple scattering are relatively weak; it may become less accurate near the ultraviolet absorption edge, in strong infrared phonon-absorption regions, or at temperatures close to phase-transition regions where optical constants, domain structures, and defect states may change significantly.

2.1.1 Optical Losses Induced by Material Absorption

Material absorption is one of the intrinsic factors governing the optical transparency of ferroelectric ceramics. Its origin is primarily associated with the electronic band structure and lattice vibrational characteristics of the material. When the photon energy matches allowed electronic transitions or phonon absorption processes, a portion of the optical energy is converted into electronic excitation or lattice vibration, leading to attenuation of the transmitted light intensity. For most oxide-based TFCs, intrinsic absorption in the visible spectral range is generally weak. However, interband transitions in the ultraviolet region and multiphonon absorption in the mid-infrared region can still introduce noticeable optical losses [81].

In practical material systems, extrinsic absorption often plays a dominant role in limiting optical transparency. Structural imperfections, such as oxygen vacancies, impurity ions, and valence-related defects, may introduce localized states within the bandgap, thereby creating additional absorption channels. These defect-related absorption processes not only reduce the overall transmittance but can also induce a redshift of the absorption edge or spectral broadening, thereby narrowing the transparent window. Therefore, the use of high-purity raw materials, precise compositional control, and optimized sintering atmospheres is essential to suppress absorption-related losses.

From the perspective of light propagation in materials, absorption induced attenuation of transmitted light generally becomes more pronounced with increasing propagation distance. Under idealized conditions in which interfacial reflection and microscopic scattering effects are neglected, the transmitted light intensity decreases monotonically with increasing sample thickness. This

thickness dependence indicates that normalization or correction with respect to sample thickness is required when comparing the optical transparency of different materials or samples.

2.1.2. Interfacial Reflection Losses

Interfacial reflection losses originate from the electromagnetic boundary conditions that must be satisfied when light propagates across interfaces between media with different refractive indices and therefore constitute an unavoidable source of optical loss in transparent ferroelectric ceramics. When light is incident from air onto a ceramic material with a higher refractive index, a portion of the incident light is reflected back toward the incident direction even under normal incidence, thereby reducing the effective light intensity transmitted through the sample. Consequently, even under ideal conditions where the ceramic is fully dense and free of pronounced scattering centers, the optical transparency of TFCs is intrinsically limited by interfacial reflection losses.

In the ideal case where only a single flat interface between air and the ceramic is considered, the reflection behavior can be described using the Fresnel equations. For normal incidence, the reflectance of a single interface (r_S) can be expressed as follows [82]:

$$r_s = \left(\frac{n-1}{n+1}\right)^2 \tag{2}$$

where n denotes the refractive index of the ceramic material, and the incident medium is air with n = 1. This relation indicates that the reflection loss at a single interface increases significantly as the refractive index increases. Since TFCs generally exhibit relatively high refractive indices, the reflection effect at an individual surface cannot be neglected.

In practical samples, incident light successively passes through both the entrance and exit surfaces of the ceramic. To simplify the estimation of interfacial reflection losses, it is commonly assumed that the upper and lower surfaces of the ceramic are parallel, and that absorption and scattering within the bulk are neglected. Under this approximation, when only one reflection event at each surface is considered, the overall reflection loss can be approximated as the accumulation of

two single interface reflections. This treatment corresponds to a single reflection approximation.

However, in practical optical propagation processes, light reflected from the lower surface is not entirely lost, because it may continue to propagate within the ceramic and subsequently emerge from the sample after multiple internal reflections. Based on this consideration, reflection loss analyses of conventional transparent ceramics often incorporate models that account for multiple internal reflections to correct the overall reflection loss. Under the assumptions that absorption and scattering are negligible and that the refractive indices of the upper and lower surfaces are identical, the overall reflection loss R_s can be expressed solely as a function of the refractive index n of the material [82]:

$$R_s = \frac{2r_s}{1 + r_S} \tag{3}$$

This equation demonstrates that, when multiple internal reflections are taken into account, the interfacial reflection loss of a ceramic is no longer equivalent to a simple superposition of single interface reflectances. Instead, it is determined by the cumulative effect of multiple reflection processes, and its magnitude is ultimately constrained by the intrinsic refractive index of the material.

For conventional transparent ceramics such as alumina and magnesium fluoride, optical anisotropy is generally weak, and birefringence effects at grain boundaries can often be neglected. As a result, the above reflection model can reasonably describe interfacial reflection losses. In contrast, transparent ferroelectric ceramics typically exhibit pronounced optical anisotropy associated with both the grains and ferroelectric domains. Refractive index discontinuities may exist across grain boundaries and domain walls, thereby introducing additional reflection behavior. These factors are not fully considered in the above idealized model and may lead to deviations from experimental observations. This indicates that the quantitative relationship between interfacial reflection processes and complex microstructural features still requires further systematic investigation.

2.1.3. Microscopic Light Scattering

Microscopic scattering losses mainly originate from spatial inhomogeneity of the refractive

index within TFCs and represent a major cause of deviation of transmitted light from its original propagation direction. When light propagates through the material and encounters microstructural units with different sizes, orientations, or optical properties, local variations in the refractive index disrupt its original propagation path. As a result, part of the optical energy is deflected from the forward direction, resulting in scattering losses.

In the description of microscopic scattering behavior, a scattering coefficient is commonly introduced to characterize the overall attenuation of light intensity induced by microstructural features. Under the approximation that strong multiple scattering coupling effects can be neglected, scattering induced attenuation of transmitted light progressively accumulates with increasing propagation distance. The magnitude of scattering is closely related to the density of scattering centers, their characteristic size, and the refractive index contrast with respect to the surrounding matrix. Because multiple types of microstructural features coexist in TFCs, the resulting scattering behavior typically exhibits pronounced multiscale characteristics.

According to the origin and formation mechanisms of microstructures, the main scattering sources in TFCs can be classified into the following categories:

1) Pores and abnormal particle packing: During ceramic forming and sintering, insufficient powder dispersion or improper control of the densification process may lead to residual pores or low-density regions associated with abnormal particle packing. The effective refractive index of pores is significantly lower than that of the ceramic matrix, leading to a large refractive-index contrast at the pore and matrix interface [83, 84]. When the pore size approaches the wavelength of the incident light, scattering effects become pronounced. The scattering intensity associated with pores depends not only on pore size but also strongly on the pore volume fraction. When pore sizes are much smaller than the optical wavelength, scattering approximately follows the Rayleigh scattering mechanism. In this regime, the pore-induced scattering coefficient can be described in a simplified scaling form as [84, 85]:

$$\alpha_{sca} \propto f_P r^6 \lambda^{-4} \quad (4)$$

where α_{sca} denotes the scattering coefficient representing scattering losses in the material, f_p is the pore volume fraction, r is the characteristic pore radius, and λ is the wavelength of the incident light. This relation indicates a strong wavelength dependence, with shorter wavelengths being more strongly scattered. As pore sizes gradually approach the optical wavelength scale, the scattering characteristics change, and the forward scattering component becomes more significant, leading to a more pronounced reduction in-line transmittance.

In recent years, quantitative descriptions of pore scattering behavior have been reported. Zhao *et al.* established a scattering model for nanoscale spherical pores in transparent ceramics based on the Rayleigh scattering approximation and systematically analyzed the effects of pore size and volume fraction on optical transmittance [83]. Their results indicate that, when pore sizes are much smaller than the optical wavelength, the pore volume fraction has a more pronounced influence on in-line transmittance than the individual pore size. This model can explain experimentally observed transmittance trends to some extent. However, its applicability relies on assumptions such as simplified pore morphology and a uniform distribution of scattering centers.

In practical TFCs, pores often exhibit nonuniform size distributions and irregular morphologies and coexist with other scattering sources, which further complicates pore scattering behavior. Therefore, improving forming uniformity and optimizing sintering processes to reduce the pore volume fraction remain effective engineering approaches for suppressing pore related scattering losses.

2) Impurity and secondary-phase interference: Low-purity raw materials, compositional inhomogeneity, or improper control during sintering can induce the precipitation of secondary or impurity phases in TFCs. These heterophases often differ markedly from the matrix in chemical composition, crystal structure, and optical constants, thereby forming interfacial regions with significant refractive index discontinuities. When incident light propagates through the material and

encounters such interfaces, abrupt variations in the optical field occur. As a result, the secondary phase regions act as strong scattering centers [84].

Unlike grain boundary related scattering, scattering induced by impurity or secondary phases is generally more random and less controllable. Its intensity depends not only on the size and volume fraction of the secondary phases but also on their spatial distribution and interfacial integrity. In particular, when the characteristic size of secondary phases approaches the wavelength of visible light or when they exhibit irregular morphologies, their detrimental effect on in line transmittance becomes significantly enhanced [86].

Moreover, in TFCs, the presence of secondary phases may disrupt the continuity of the local phase structure and induce enhanced local optical anisotropy. This effect can further amplify interfacial scattering. Therefore, suppressing the formation of impurity and secondary phases through the use of high purity precursors, precise compositional control, and carefully optimized sintering atmospheres and heating profiles is a necessary prerequisite for achieving high optical transparency in ferroelectric ceramics.

3) Grain boundaries and random orientation: TFCs are typically composed of a large number of randomly oriented grains. Orientation mismatch between neighboring grains leads to spatial fluctuations in the effective refractive index, thereby forming scattering interfaces at grain boundaries. Even under fully dense conditions without obvious secondary phases, grain boundary scattering may still represent an important factor limiting optical transparency [84]. For birefringent TFCs, different grain orientations correspond to different optical responses, making grain boundary scattering more pronounced than in optically isotropic ceramics. Reducing grain orientation mismatch to suppress effective refractive index fluctuations represents a potential approach to mitigating grain boundary scattering.

4) Ferroelectric domain-wall scattering: Ferroelectric domain walls are internal structural interfaces with specific orientation relationships and spatial distribution characteristics in TFCs.

Because polarization directions and lattice distortion states differ across domain walls, their optical responses may also differ. When propagating light intersects domain walls, local variations in the refractive index cause deviations in the propagation direction, thereby inducing scattering.

In TFCs, domain sizes are often comparable to visible wavelengths, which leads to strong light scattering. When domains are much smaller than the wavelength, scattering follows the Rayleigh mechanism. In this case, the scattering intensity is inversely proportional to the fourth power of the wavelength, and shorter wavelengths scatter more strongly. Conversely, when domains are comparable to or larger than the wavelength, scattering follows the Mie regime. This regime is commonly characterized by the size parameter [87, 88]:

$$x = \frac{2\pi r}{\lambda} \tag{5}$$

where x is the dimensionless size parameter, r is the characteristic domain size, and λ is the wavelength of the incident light. When $x \sim 1$ or larger, the wavelength dependence of scattering is weakened and forward scattering becomes increasingly dominant (Fig. 4(b)). Reducing domain sizes well below the optical wavelength effectively suppresses Mie scattering. For visible light, this generally requires domain sizes below several tens of nanometers, whereas for infrared wavelengths the corresponding Rayleigh-scattering regime can extend to substantially larger length scales [73, 89, 90].

Beyond qualitative analysis, theoretical modeling of ferroelectric domain wall scattering has also been explored. Xiong *et al.* [89] performed quantitative calculations of domain wall scattering effects on optical transmittance in ferroelectric single crystals based on refractive index ellipsoid projection and scattering theory, revealing a strong dependence of scattering behavior on domain wall type and orientation. This work provides important theoretical insight into the anisotropic nature of domain wall scattering. It should be noted that, compared with single crystal systems, TFCs generally exhibit the coexistence of multiple domain types and orientations with highly complex

spatial distributions. Meanwhile, refinement of domain size is often accompanied by simultaneous grain size reduction, and excessively small grains may adversely affect mechanical properties and ferroelectric performance [33]. Therefore, achieving coordinated control of grain size and domain scale while maintaining optical transparency remains a key technical challenge in the structural design of TFCs.

Following the above discussion, the transmittance of TFCs discussed in this section refers specifically to the effective in line transmittance, which corresponds to transmitted light that maintains its propagation direction with minimal angular deviation. This definition more accurately reflects the combined effects of absorption, reflection, and small angle scattering on light propagation. In contrast, total transmittance measured using an integrating sphere includes both directly transmitted light and light scattered at large angles, resulting in values that are typically much higher than the in line transmittance. For TFCs, in which pores, grain boundaries, and ferroelectric domain walls can induce pronounced angular scattering, reliance solely on total transmittance measurements may overestimate the effective optical performance in practical device applications. Accordingly, transmittance related discussions in this section are consistently based on the definition of in line transmittance to ensure physical consistency with the actual optical behavior of TFCs.

Overall, the optical transmittance of transparent ceramics depends on the coupled effects of intrinsic absorption and microstructure-induced scattering. Throughout fabrication, from raw-material selection and powder processing to uniform compaction, sintering densification, and surface finishing, each optimization of structural design and interfacial control plays a decisive role in the final optical performance. Especially in TFCs, suppressing scattering while maintaining polarization stability is essential for simultaneous optimization of optical and electrical functionalities, is still the core technical challenge till now.

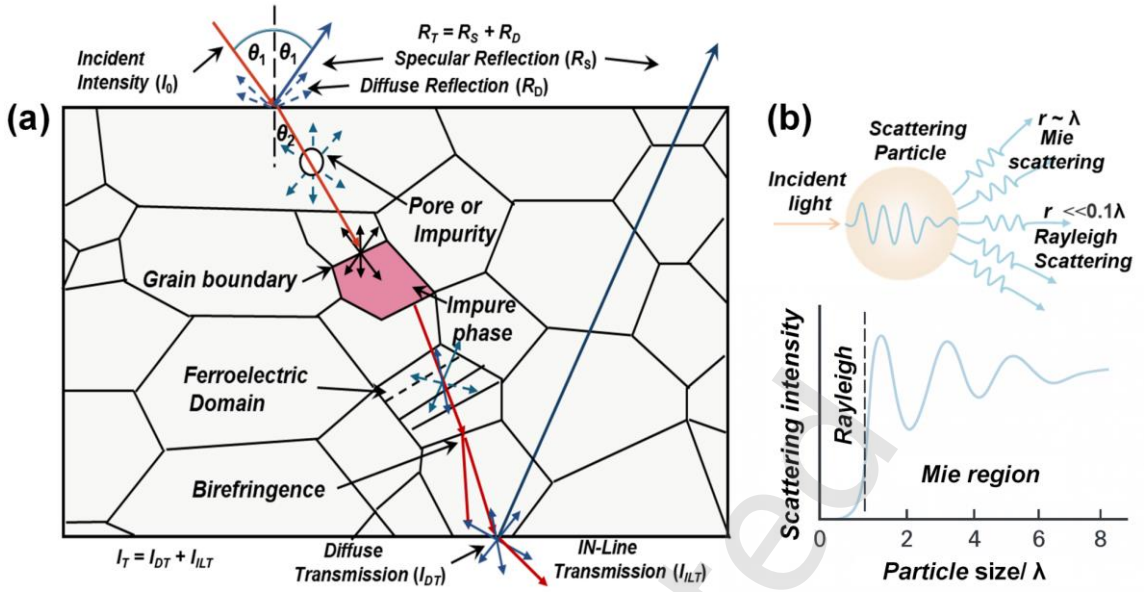

Fig. 4. (a) Various factors influencing the transmittance of ceramics. (b) Principles of Rayleigh and Mie scattering.

2.2. Strategies to Enhance the Transparency

The high light transmittance of transparent ceramics is the foundation for achieving excellent optical and functional performance, and enhancing transparency has always been the core goal of material design and process optimization. Because ceramics are polycrystalline, factors such as interfacial irregularities, pores, impurity phases, grain-size variations, and lattice distortions can all cause scattering and absorption, leading to transmittance reduction. Therefore, to enhance the transparency of ceramics, efforts should be made simultaneously from the aspects of microstructure regulation and macroscopic densification processes, comprehensively reducing various scattering and absorption losses of light. The following will provide a detailed introduction to the key strategies for achieving high density through sintering process optimization and reducing optical scattering through microstructure regulation.

2.2.1. Optimization of Sintering Processes for Enhanced Densification

Achieving high densification is essential for fabricating transparent ceramics. Conventional sintering often leaves residual pores, uneven grain boundaries, and inhomogeneous intergranular phases, which induce light scattering and reduce optical transparency. To overcome these challenges,

advanced sintering techniques such as HIP, HPS, and their modified combinations have been widely applied (Fig. 5). These methods eliminate pores, increase bulk density, and smooth grain boundaries, thereby suppressing optical scattering.

Both HPS and HIP densify ceramics through the synergistic effect of heat and pressure, differing mainly in pressure applying mode: HPS applies uniaxial pressure, while HIP uses isotropic gas pressure, typically with argon. Typically, external pressures of 10 to 50 MPa are applied under vacuum or controlled atmospheres to accelerate particle deformation and diffusion. Compared with conventional sintering, applying a pressure field lowers the sintering activation energy, reduces the densification temperature by 100 to 200℃, and suppresses the volatilization of volatile elements such as Pb, K, and Na. Meanwhile, applied uniaxial or isostatic stress restricts grain-boundary migration, refines grain size, and removes subsurface defects in pre-sintered compacts. High-density transparent ceramics have been obtained by HIP at relatively low temperatures and short holding times. For example, near-theoretical density and excellent transmittance were reported in PZT and $Pb(Ni,Nb)O_3$-$PbZrO_3$-$PbTiO_3$ systems [91-93]. However, the high cost of HIP equipment limits its wide application, while HPS is more widely used. In the KNN system, HPS significantly lowers the sintering temperature and improves the microstructure, achieving over 60% transmittance in the 800 to 900 nm wavelength range [71, 94]. Further studies confirmed that HPS effectively reduces porosity and transforms opaque samples into transparent ones [95], demonstrating its practicality and advantages for TFCs.

Spark plasma sintering (SPS) uses pulsed current and pressure to achieve rapid densification. It offers a fast heating rate, lower sintering temperature, short dwell time, and controllable grain growth. Compared with conventional sintering, SPS offers distinct advantages for transparent ceramics, including high density at low temperature, suppression of porosity and abnormal grain growth, and fewer light-scattering centers, resulting in enhanced optical transmittance. SPS is also well suited for difficult-to-sinter or thermally sensitive systems, such as nanocrystalline transparent ceramics, doped

laser ceramics, and multiphase composites. Early studies showed that SPS could produce dense, fine-grained transparent lead-based ferroelectric ceramics in systems such as $PbZrO_3$–$PbTiO_3$–$Pb(Zn,Nb)O_3$ and PLZT. These ceramics were typically spark-plasma-sintered at 900°C for 10 min under a vacuum of ~6 Pa and a uniaxial pressure of 29 MPa, followed by post-annealing in a PbO-rich atmosphere to compensate PbO volatilization and re-oxidize partially reduced samples [96, 97]. Recent studies extended SPS to complex systems such as $(Pb,La)(Mg,Nb)O_3$–$PbTiO_3$ [98], showing that it produces uniform microstructures and excellent optical quality while minimizing unwanted secondary phases. However, the rapid densification may cause slight compositional deviations, affecting dielectric behavior. Overall, SPS is an efficient densification method with great potential for structural optimization and miniaturization of multifunctional transparent electronic devices.

Sintering in an oxygen atmosphere further promotes densification by reducing grain-boundary energy and enhancing boundary mobility, which facilitates particle rearrangement and pore elimination. Oxygen also suppresses impurity segregation and reduces oxygen-vacancy concentration, improving diffusion kinetics and intergranular bonding. This approach is especially effective for lead-based systems. Studies show that combining oxygen sintering with other processing methods markedly improves the microstructure and transparency of PMN–PT ceramics. For example, ball-milled La-doped PMN–PT sintered in oxygen achieved about 68% transmittance at wavelength of 2000 nm, comparable to hot-pressed samples [99]. Using sol–gel-derived powders with oxygen sintering, a relative density of 98% and transmittance of 54 to 69% across 633 nm to 1550 nm were achieved [100, 101]. These results demonstrate that oxygen sintering effectively enhances densification and provides a cost-effective route to high-performance transparent ferroelectric ceramics.

Combining an oxygen atmosphere with pressure-assisted sintering further improves density and optical performance. Oxygen eliminates residual pores and reduces oxygen vacancies, which refines the microstructure and enhances transparency. For instance, Li *et al.* [32] used oxygen hot pressing to

fabricate 3 mol% La-doped 75PMN–25PT transparent ceramics, achieving about 65% transmittance in the near-infrared region . Similarly, Zeng *et al.* [65] reported high transmittance and excellent electrical properties in 3 mol% Pr-doped 70PMN–30PT ceramics near the morphotropic phase boundary. A common preparation route is pre-sintering in oxygen to remove pores, followed by hot pressing for final densification. Building on this concept, Zeng and Wei *et al.* [102, 103] produced high-quality Er-doped PMN–PT by a two-step sintering approach. Using similar methods, Song, Gao, and Zheng *et al.* [64, 104, 105] fabricated La-PMN–PT, Sm-PMN–PT, and Sm-PIN–PMN–PT transparent ceramics. These findings confirm that combining an oxygen atmosphere with a pressure field is crucial method for achieving high-density, high-transparency ferroelectric ceramics.

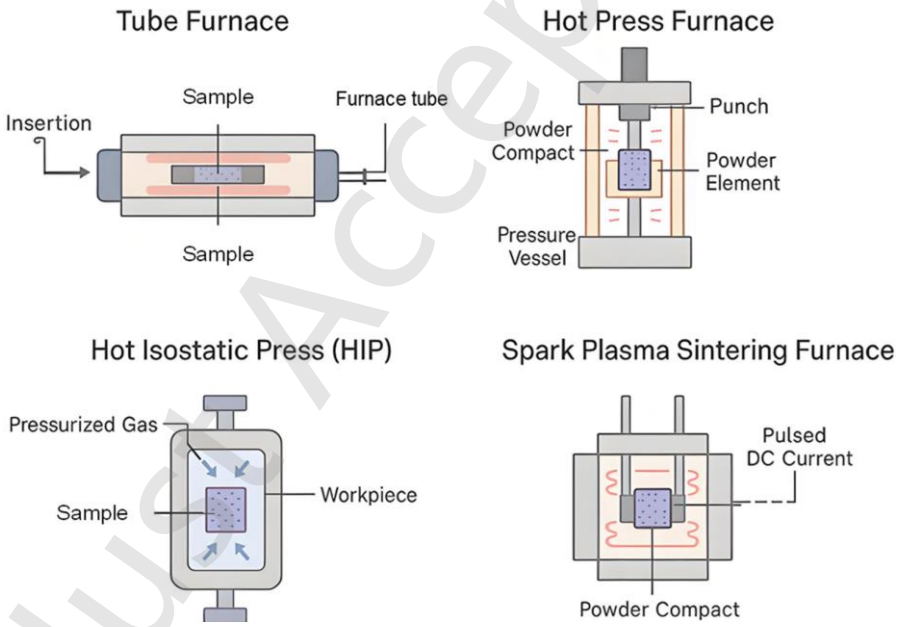

Fig. 5. Different sintering methods for fabricating transparent ceramics.

2.2.2. Grain-Size Control to Suppress Grain-Boundary Scattering

As shown in Fig. 4(b), when scattering centers are much smaller than the wavelength of incident light, Rayleigh scattering dominates and the scattering efficiency is low. When the grain size approaches or exceeds the wavelength, scattering increases markedly. Therefore, transparent ceramics typically require grain refinement to the nano- or sub-micrometer regime to reduce interfacial scattering and enhance in-line transmittance. In the KNN system, this mechanism has

been validated. Zhao *et al.* [83] established a Rayleigh-based porosity model (via Sm doping) that revealed the effects of pore size and volume fraction on transmittance. When the pore size is about 30 nm and the volume fraction is about 0.3%, the transmittance at 780 nm reaches about 67%, in close agreement with the theoretical predictions. These results prove subwavelength pore scattering is the key controlling factor for transparency.

In practice, dopant engineering is the primary method for regulating grain growth. Transition-metal doping can generate a transient liquid phase during sintering, which effectively suppresses coarsening. Representative results show that KNN–$Sr(Sc_{0.5}Nb_{0.5})O_3$ (KNN–SSN) ceramics have about 70% transmittance at 780 nm with a grain size of about 340 nm [106], and KNN–$Sr(Al_{0.5}Nb_{0.5})O_3$ (KNN–SAN) samples have about 60% transmittance at 1064 nm with a grain size of about 200 nm [107]. Rare-earth dopants are likewise effective. Sm-doped KNN reaches about 55% at 780 nm (grain size about 160 nm) [51], Tb-doped KNN reaches about 67% at 780 nm (about 154 nm) [53], Pr-doped KNN achieves about 73% at 900 nm (about 170 nm) [52], Eu-doped KNN attains about 75% at 1000 nm (about 320 nm) [108].

Moreover, co-doping together with sintering aids can further refine the microstructure and improve transparency. For example, Er/La-doped KNN shows nearly 70% transmittance at 900 nm with a grain size of about 140 nm. Tb/Eu co-doped ceramics show about 48% transmittance at 780 nm with a grain size of about 140 nm [109]. Rare-earth co-doping combined with Li_2CO_3/Bi_2O_3 sintering aids yields series such as e (K,Na,Li)(Nb,Bi)O_3-Er/Ho (KNLNB-Er/Ho) and KNN-$ErBiO_3$ (KNN-EB), both maintaining about 55% transmittance at 780 nm with grain sizes near 200 nm [109, 110]. Yu *et al.* and Wu *et al.* [50, 111] further reported Ba/Pr and Sr/Pr co-doping strategies that achieved 62 to 66% transmittance at 780 nm, with the minimum grain size reduced to 83 nm.

Overall, transparency in KNN-based ceramics is largely governed by subwavelength control of grains and pores. Whether through transition-metal or rare-earth single doping, or through rare-earth/sintering-aid co-doping, these routes suppress grain coarsening and optimize porosity, thereby

effectively enhancing optical transmittance. These studies provide a rich set of material systems and technical paths toward highly transparent, high-performance ferroelectric ceramics.

2.2.3. Domain-Size Engineering to Reduce Domain-Wall Scattering

Beyond grain boundaries, ferroelectric domain walls can also play a critical role in optical scattering in transparent ceramics. In dense lead-based perovskite ceramics such as PMN–PT, where residual pores are minimized and grains are usually much larger than visible wavelengths, grain-boundary scattering may be relatively weak, and domain-wall-related scattering can become an important optical-loss channel. However, this contribution is not universal and depends strongly on crystallographic orientation, domain-wall type, domain spacing, measurement wavelength, and transmittance-measurement geometry. Refractive-index contrast across domain walls and associated local stress fields can perturb light propagation, with the effect becoming more pronounced when the characteristic domain size or domain spacing approaches the incident wavelength. Consequently, domain engineering has emerged as an important route to enhance transparency, including suppressing micron-scale coarse domains and refining them into nanoscale domains or PNRs well below the optical wavelength.

Existing studies have revealed how domain structures evolve under different doping conditions through microscopic characterization. The domain sizes discussed here are mainly characteristic values reported from PFM, TEM, or optical-microscopy observations in the original studies, and are used for comparison with the optical wavelength. Zhou *et al.* [112] used Piezoresponse Force Microscopy (PFM) to reveal a progressive refinement from large domains to uniformly distributed, fingerprint-like microdomains (hundreds of nanometers) in Eu-doped 75PMN–25PT, accompanied by suppressed optical scattering (Fig. 6(a)). Li *et al.* [90] further quantified the correlation between domain size and transparency in Eu-75PMN–25PT. Increasing Eu^{3+} drives a transition from irregular large domains to layered domains (about 200 nm) and island-like nanodomains (about 50 nm), and at 3 mol% Eu doping a labyrinthine pattern forms with a pronounced rise in transmittance (Fig. 6(b)).

Yan *et al*. [60] reported that in Eu-doped 72PMN–28PT, small "water-mark" domains favor high optical transmittance, whereas stripe domains correlate with higher piezoelectric coefficients (Fig. 6(c)). Collectively, these results indicate that refining domains to about 50 to 200 nm and improving their uniformity are effective strategies to suppress scattering and to boost in-line transmittance.

Rare-earth doping has recently been consolidated as an efficient lever for domain engineering. Lattice distortion induced by rare-earth ions disrupts long-range order and promotes nanodomain formation, thereby reducing optical scattering. For example, Ruan *et al*. [113] observed in La-doped 75PMN–25PT that domains refine from large irregular, fingerprint-like patterns to smaller scale ones, accompanied by a marked increase in transparency, which underscores the role of domain refinement in mitigating scattering. Hu *et al*. [58] reported small domains of 150 to 200 nm in La-doped PMN–PT, corresponding to about 69% transmittance at 1550 nm (Fig. 6(d)) . Guo *et al*. [61] showed that irregular "water-mark" domains and curved domain walls produced by Eu doping reduce optical anisotropy and improve near-infrared transmittance. Collectively, regardless of the specific ion type, rare earth doping generally suppresses scattering through domain refinement and domain configuration regulation, providing a feasible path for improving transparency.

Overall, the optical performance of PMN–PT transparent ceramics depends not only on densification and grain size but also, more strongly, on domain scale and configuration. Through rare-earth doping, targeted domain-engineering design, and process optimization, the long-range ferroelectric domains can be effectively regulated. Such domain engineering reduces the density of optically active domain walls that contribute to light scattering and promotes a more ordered domain configuration, thereby significantly enhancing optical transparency. In parallel, selecting appropriate crystal phases with low birefringence and suppressing color-center absorption associated with defects and oxygen vacancies are essential to achieve high transparency at wavelengths above 400 nm while maintaining excellent electrical properties.

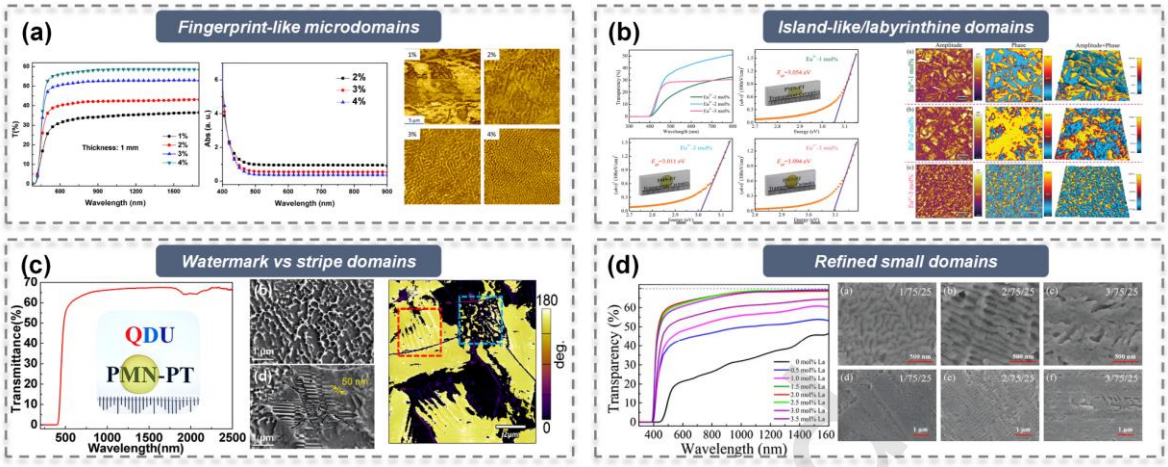

Fig. 6. Relationship between transmittance and domain structure. (a) Evolution from large domains to fingerprint-like microdomains. Reproduced with permission from Ref. [112], © Wiley-Blackwell 2016. (b) Transition from layered domains to island-like and labyrinthine domains. Reproduced with permission from Ref. [90], © Royal Society of Chemistry 2021. (c) Comparison between water-mark and stripe domains. Reproduced with permission from Ref. [60], © American Chemical Society 2021. (d) Effect of domain refinement on optical transmittance. Reproduced with permission from Ref. [58], © Tsinghua University Press 2023.

2.2.4. Phase Engineering to Minimize Birefringence and Phase-Boundary Scattering

In transparent ceramics and single crystals, the crystal structure is a primary determinant of optical transmittance (Fig. 7). High-symmetry cubic (C) phase is optically isotropic and therefore free of birefringence, which effectively minimizes scattering and absorption during light propagation. For example, stabilized cubic zirconia and yttria show excellent transparency from the visible to the near-infrared because of their high symmetry, uniform refractive index, and small grain-boundary optical-path differences. In ferroelectric ceramics, most high-transmittance materials also reside in cubic or pseudo-cubic states. Examples include La-doped 75PMN–25PT and 88PMN–12PT [104, 114], as well as some KNN-based systems such as KNN-3Pr, KNN-3Sm, and KNN-2Eu [51, 52, 108], whose transmittance approaches theoretical values.

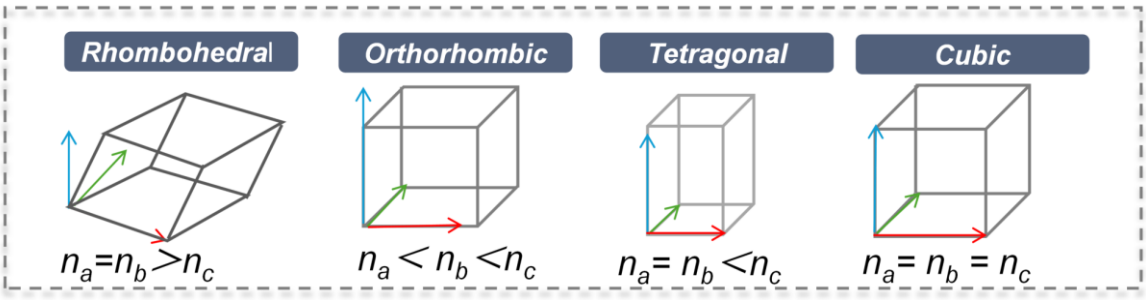

Fig. 7. Schematic illustration of refractive-index anisotropy in four typical crystal structures.

In contrast, low-symmetry structures such as R, O, and T phases exhibit pronounced optical anisotropy. Refractive-index differences along different crystallographic directions lead to birefringence and interference enhancement, which significantly reduce overall transmittance. Such structures are often accompanied by lattice distortion and residual-stress concentration, which readily generate strong scattering centers at grain or phase boundaries. For example, KNN–SAN (O phase, transmittance ≈ 55%), KNLNB-Sr/Ba and KNLNB-Er (T phase, transmittance ≈ 60%), and KNN–BNN-Ta (O–T phases, transmittance ≈ 61%) ceramics all exhibit considerable scattering and do not reach theoretical transmittance levels [28, 107, 115, 116]. Similar behavior is also observed in PZT-based and Sm-doped PIN–PMN–PT ceramics, where low structural symmetry markedly constrains optical performance [64, 117-119].

In multiphase ceramics, significant refractive-index mismatches between phases may generate strong interfacial scattering and severely impair transparency. The key strategy is to minimize refractive-index contrast through compositional regulation. Optimizing solid-solution ratios, precisely controlling dopant concentrations, and introducing secondary phases with optical properties similar to the matrix can markedly reduce interfacial reflection and scattering. When the refractive-index difference is constrained within a narrow range, overall transmittance can approach the theoretical limit of single-phase systems. In PMN–PT ceramics, researchers commonly use doping to stabilize a cubic-like rhombohedral state while introducing a small fraction of T phase or PNRs, thereby maintaining excellent electrical properties together with enhanced transparency. For example,

Eu-doped 72PMN–28PT achieves high transmittance and favorable electrical performance through the cooperative effect of a rhombohedral matrix with a minor tetragonal component [60].

In summary, controlling phase symmetry and matching refractive indices at multiphase interfaces to construct microstructures with low birefringence and reduced scattering is a key route to enhance the optical performance of transparent ceramics and single crystals.

2.2.5. Defect Regulation via Atmosphere Annealing and Dopant Engineering

Another key issue affecting transparent ceramics is the presence of intrinsic defects, such as oxygen vacancies, and PbO-related compositional heterogeneities. In lead-based transparent ceramics, excess PbO segregation at grain boundaries or within secondary phases induces local refractive-index fluctuations, thereby increasing light scattering and reducing optical transmittance. In recent years, various post-treatment strategies, including oxygen-atmosphere annealing, prolonged heat treatment, and surface polishing, have been employed to improve transparency. Among these approaches, oxygen annealing is particularly effective in suppressing oxygen vacancies and mitigating PbO-related scattering centers.

Representative studies have demonstrated the strong effectiveness of these approaches. Londono *et al.* [120] annealed hot-pressed $(Pb_{1-x}La_x)TiO_3$ (PLT) transparent ceramics in oxygen. Adjusting heating rate and holding time (5 to 10 h) consistently improved transmittance by removing excess PbO. Kong *et al*. [121] similarly reported that thermal treatment of PMN–PT removed excess lead oxide and converted opaque ceramics into semi-transparent ones. Bartscherer *et al.* [122] observed that, for PLZT, annealing after 72 h of HIP transformed reddish semi-transparent samples into colorless transparent ones. Wu *et al.* [97] found that appropriate annealing temperatures markedly reduced pore fraction in SPS-sintered PLZT, thereby enhancing transparency. Huang *et al.* [123] reported that oxygen annealing of Ba/Ho/Yb co-doped KNN suppressed oxygen vacancies, lightened coloration, and improved transmittance, although photochromic and luminescent tunability decreased. These results indicate that well-controlled annealing can substantially improve

transparency and, in many cases, electrical performance, even with partial trade-offs in specific optical functionalities. Collectively, these examples highlight that appropriate thermal treatment and atmosphere control are crucial for eliminating pores and defect-related heterogeneities.

In parallel, careful control of dopant introduction and processing can mitigate dopant-induced local defects, and enable higher transparency without sacrificing electrical performance. Taken together, coupling defect-healing with process optimization is pivotal to achieving high transmittance while retaining functional properties in TFCs.

In summary, TFCs can achieve high optical transmittance together with excellent electrical performance only through a multi-pronged strategy that combines sintering optimization for densification, grain refinement, refractive-index matching, and systematic defect management—all orchestrated to navigate the delicate compromise between optical clarity and functional potency. This integrated approach provides a reliable foundation for advanced device applications.

3. Functional classification and performance regulation

The true potential of TFCs is revealed not only by their individual physical responses, but also by the coupling among optical transparency, ferroelectric polarization, piezoelectricity, electro-optic effect, energy storage, photoluminescence, photochromism, and defect-related responses. These functions are not independent: they are jointly governed by grain/domain configuration, phase symmetry, refractive-index matching, defect chemistry, rare-earth luminescent centers, and polarization dynamics. Therefore, the key scientific issue in TFCs is not single-property maximization, but coupled optimization of transparency, functionality, and reliability. This section categorizes TFCs based on their primary functionalities, including piezoelectric, electro-optic, energy-storage, photoluminescent, and photochromic properties, while emphasizing the material-design principles, coupling mechanisms, performance milestones, and inherent trade-offs for each class. The parallel development of lead-based PMN–PT and lead-free KNN systems provides a comparative narrative of progress and challenge.

3.1. Transparent Piezoelectric Materials

3.1.1. Piezoelectric Effect and Application

As illustrated in Fig. 8, piezoelectricity—the generation of electric charge under mechanical stress and vice versa—is harnessed in sensors, actuators, and transducers.

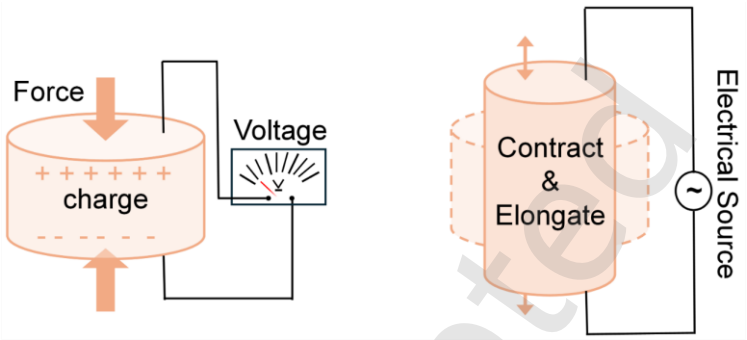

Fig. 8. Schematic illustration of the principle of the piezoelectric effect.

Transparent piezoelectrics enable devices where optical access and mechanical transduction must coexist, such as in transparent ultrasonic transducers for simplified, high-resolution photoacoustic imaging, and in see-through actuators for robotics and adaptive optics [61, 124, 125]. Current transparent or semi-transparent piezoelectric platforms for photoacoustic imaging can be broadly categorized into flexible polymer films, oxide single crystals, and transparent ferroelectric ceramics. Polyvinylidene fluoride (PVDF) films offer flexibility and acoustic-impedance matching, whereas $LiNbO_3$ (LN) and PMN–PT single crystals provide mature or high-sensitivity benchmarks. In comparison, PMN–PT and KNN-based transparent ceramics offer advantages in compositional tunability, machinability, cost control, and potential array fabrication. These different material forms follow distinct processing routes, microstructural characteristics, and device-integration strategies, and should therefore be distinguished when comparing their application performance.

For example, photoacoustic imaging (PAI) systems using commercial PVDF have achieved three-dimensional imaging of letters and have shown promise for wearable devices [126]. Park *et al.* [47] developed transparent PMN–PT single crystals with a piezoelectric coefficient (d_{33}) of about 1500 pC N^{-1} and a transmittance of about 80% at 650 nm, enabling a handheld transparent ultrasonic

transducer for in vivo photoacoustic imaging of mice. These film and single-crystal examples provide useful device-level benchmarks for transparent piezoelectric systems. In contrast, transparent ferroelectric ceramics remain attractive for future scalable and integrated devices because of their compositional flexibility, ceramic processability, and potential for array fabrication.

The piezoelectric effect enables efficient coupling between mechanical and electrical signals, and high transmittance reduces scattering for optical imaging and real-time monitoring. However, a fundamental trade-off persists between transparency and piezoelectric performance. Increasing the density of ferroelectric domains and domain walls enhances polarization response but also intensifies optical scattering and degrades transparency. Resolving this conflict remains a central challenge to further improving the performance of this class of ceramics.

3.1.2. Progress and Optimization Strategies in PMN–PT

In general, ceramics with high piezoelectric activity possess a dense population of ferroelectric domains, high-density domain walls have a strong scattering effect on light. Therefore, achieving transparent piezoelectric ceramics that combine high piezoelectric performance with high optical transmittance remains highly challenging. PMN–PT based transparent piezoelectric materials can be divided into several stages, as shown in Fig. 9.

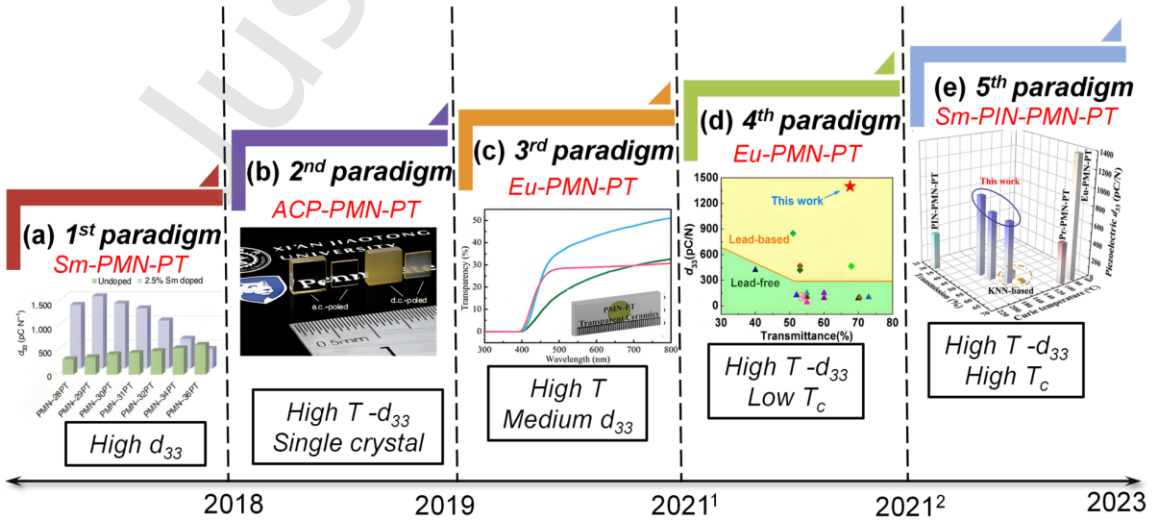

Fig. 9. Development progress of PMN–PT transparent piezoelectric materials (the 1st paradigm represents non-

transparent samples. (a) Sm-PMN–PT ceramics with high d_{33}. Reproduced with permission [127], © Springer Nature 2018. (b) Sm-PMN–PT transparent piezoelectric single crystals subjected to ACP. Reproduced with permission from Ref. [128], © Springer Nature 2020. (c) PMN–PT transparent ceramics with moderate d_{33}. Reproduced with permission from Ref. [90], © Royal Society of Chemistry 2021. (d) PMN–PT transparent ceramics with high d_{33}. Reproduced with permission from Ref. [60], © American Chemical Society 2021. (e) PIN–PMN–PT transparent piezoelectric ceramics with a high T_c. Reproduced with permission from Ref. [64], © American Chemical Society 2023.

Before 2018, highly transparent PMN–PT ceramics had already been developed. However, their compositions typically contained more than 75 mol% PMN content with relatively low piezoelectric coefficients (d_{33} < 250 pC N^{-1}), and studies mainly focused on electro-optic and luminescent behavior. The d_{33} of most lead-based piezoelectric ceramics rarely exceeded 1000 pC N^{-1}, and the previous record reported is the d_{33} of $Pb(Hf,Ti)O_3$–$Pb(Ni,Nb)O_3$ on the order of 970 pC N^{-1}. In recent years, rare-earth doping has markedly improved the piezoelectric performance of PMN–PT ceramics [62]. In 2018, Li *et al.* [127] fabricated PMN–PT ceramics with a highest d_{33} of 1510 pC N^{-1} by Sm^{3+} doping. The key mechanism is the flattening of the free-energy profile induced by local structural heterogeneity. A-site substitution of Pb^{2+} by Sm^{3+} introduces local random fields and configurational perturbations, forming nanoscale polar regions. The interfacial energy between these regions and the matrix, including elastic, electrostatic, and polarization-gradient contributions, collectively modifies the free-energy landscape and improves polarization mobility. Phase-field simulations further confirmed that structural heterogeneity enhances dielectric and piezoelectric properties, providing theoretical support for performance optimization [66, 127]. Eu^{3+} doping likewise improves the piezoelectric properties of PMN–PT through a similar mechanism. Guo *et al.* [129] reported that Eu^{3+} in PMN–PT created local valence mismatch and size perturbations, which enhanced structural heterogeneity and strengthened the relaxor component, facilitating polarization rotation and domain-wall motion. Meanwhile, Eu^{3+} doping drove the phase structure toward the morphotropic phase boundary, enabling multiphase coexistence and flattening the free-energy surface. A pivotal advance

came in 2020, when Qiu *et al.* [128] used alternating-current poling (ACP) to suppress the light-scattering 71° domain walls in [001]-oriented rhombohedral PMN–PT single crystals, while mainly retaining 109° lamellar domain walls that do not cause obvious light scattering. This process yielded, for the first time, ferroelectric crystals that simultaneously exhibited ultrahigh piezoelectric performance and high optical transmittance. This work represented a major breakthrough in PMN–PT research and demonstrated strong potential for advanced optoelectronic applications [37, 124, 128]. Since around 2021, significant progress has been achieved in advancing the optoelectric properties of PMN–PT ceramics. The introduction of the two-step sintering method enabled PMN–PT ceramics to exhibit both high transmittance and a relatively high d_{33} [90]. Subsequently, through further optimization of processing parameters and doping strategies, researchers first realized PMN–PT ceramics exhibiting both high transmittance and high d_{33} [60]. Building on this progress, later studies further achieved simultaneous enhancement of transmittance, piezoelectric response, and Curie temperature (T_c) [64], thereby establishing a solid foundation for their use in advanced optoelectronic devices.

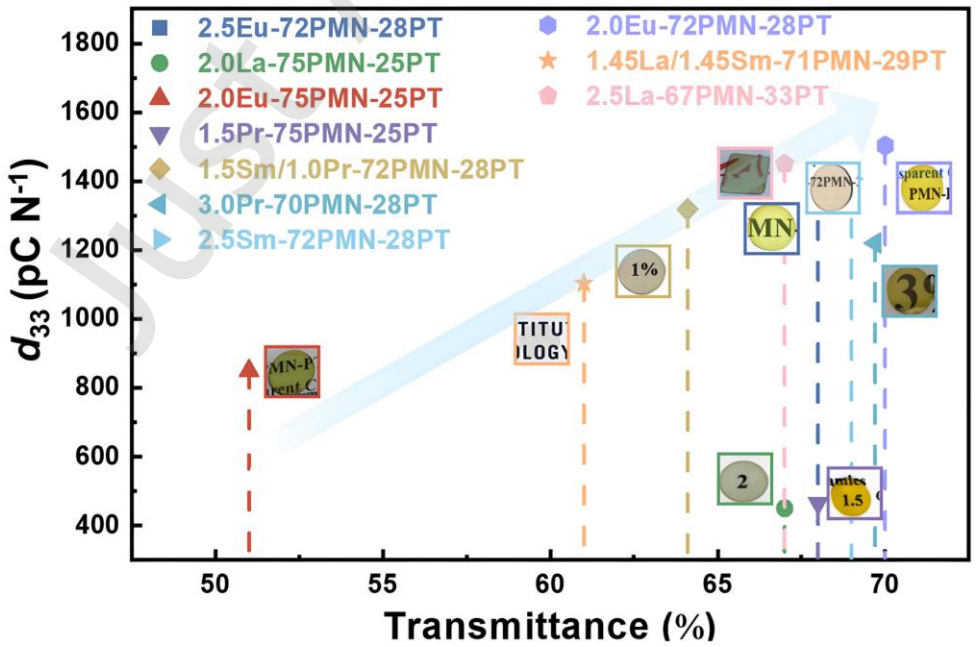

Fig. 10. Research progress on the performance of PMN–PT transparent piezoelectric ceramics.

In the PMN–PT system, researchers commonly combine rare-earth doping with MPB composition optimization to achieve synergistic enhancements in transmittance and d_{33}. In recent years, a clear development path has emerged, progressing from single rare-earth doping to multicomponent systems and then to co-doping and external-field regulation. The overall optoelectronic performance of transparent piezoelectric ceramics has gradually approached that of single crystals and, in some cases, has even rivaled it (Fig. 10). Specific advances are summarized in Table 1.

Table 1. Research progress of transparent piezoelectric ceramics

Classification	Component	Transmittance [%]	Wavelength [nm]	thickness [mm]	d_{33} [pC N^{-1}]	T_C [℃]	k_p	ε_r @1kHz	Refs.
Lead based	Eu-75PMN–25PT	51	800	--	850	87	--	7100@27℃	[90]
	Pr-75PMN–25PT	68	900	0.7	465	101	--	7076@25℃	[73]
	Eu-72PMN–28PT	68	2500	0.4	1400	80	0.64	13300@25℃	[60]
	Sm-PIN–PMN–PT	63	2500	0.4	905	179	0.66	4292@25℃	[64]
	La-75PMN–25PT	69	1550	0.5	472	--	--	--	[58]
	La-PIN–PMN–PT	66.2	1600	0.4	1012	145	--	7878@27℃	[20]
	La/Sm-71PMN–29PT	61	632	1	1104	91	--	7450@28℃	[130]
	Pr-70PMN–30PT	69.7	2500	0.7	1220	80	--	10524@36℃	[65]
	Sm/Pr-72PMN–28PT	64.1	900	0.6	1310	71	0.59	19140@30℃	[105]
	Eu-72PMN–28PT	68	2500	0.4	1500	87	0.69	8280@25℃	[61]
	Sm-72PMN–28PT	69	2500	0.3	1460	80	0.67	15100@25℃	[63]
	3Sm-PIN–PMN–PT	65.1	1800	0.6	1023	116	--	6780@25℃	[131]
	La-67PMN–33PT	67	1800	0.5	1450	68	--	8360@20℃	[132]
	La/Sm-PIN–PMN–PT	56.4	632	0.4	790	172	0.62	7900@33℃	[133]
	LPNSE-70PMN–30PT	60	900	0.5	1476	95	0.73	8803@27℃	[134]
	Eu-PIN–PMN–PT	68	1600	0.4	860	177	0.64	5918@25℃	[135]
Lead free	KNLNB	60	900	0.5	64	273	--	1220@25℃	[70]
	KNLNB-Sr/Ba	60	900	0.5	151	250	0.25	1650@25℃	[115]
	KNN–CSN	60	1064	0.5	35	147	--	1914@25℃	[136]
	KNLNB-Er	45	900	0.3	89	350	--	1396@25℃	[116]
	KNN–SAN	55	780	0.3	105	320	--	1021@25℃	[107]
	KNN–SSN	73	780	0.3	101	275	--	1481@25℃	[106]
	KNN–SZ-li$_2$O	75	2000	0.3	150	273	--	3000@25℃	[33]

KNN–BNN-Ta	60	900	0.3	185	347	--	1172@25℃	[28]
KNLNST–CZ	73.5	1800	0.1	130	--	0.175	3287@25℃	[137]
KNNLN-Er	34	850	0.28	97	--	--	--	[138]
TLKN–TSN-Sc	53	800	0.3	180	332	0.34	1220@25℃	[139]
KNTL–NB-Ta	72	780	0.3	157	182	--	1725@25℃	[140]

d_{33}, T_c, k_p, ε_r correspond to the following: piezoelectric coefficients, Curie temperature, plane electromechanical coupling coefficient, dielectric constant respectively.

Rare-earth modification plays a crucial role in improving both the optical transparency and piezoelectric performance of PMN–PT ceramics. Variations in ionic radius, valence state, and site occupancy among rare-earth cations generate distinct local lattice distortions, alter random electric fields, and redistribute domain-wall energies. These dopant-induced perturbations regulate domain types, domain size and domain-wall mobility. Such ionic-size-dependent structural modulations influence phase stability and polarization distortion, thereby defining the pathways for improving transmittance and d_{33}. Recent studies have demonstrated that rare-earth dopants exhibit an optimal ionic-size window, in which Sm^{3+} is the most effective because it is the smallest ion capable of fully occupying the A site [66]. This substitution induces pronounced local heterogeneity and markedly flattens the free-energy landscape, resulting in enhanced piezoelectric responsiveness (Fig. 11(a)).

Beyond single-element doping, co-doping strategies have been explored to balance transparency and piezoelectricity. Yu *et al.* [130] reported that La/Sm co-doped in 71PMN–29PT ceramics exhibited 61% visible transmittance along with a d_{33} of 1104 pC N^{-1}. In this system, La^{3+} promotes densification and mitigates lattice distortion to improve transparency, whereas Sm^{3+} enhances structural heterogeneity and polarization responsiveness. Their synergistic roles result in simultaneous enhancement of both properties. Notably, large-area ceramic sheets were fabricated via tape casting followed by pressureless sintering, demonstrating a scalable and low-cost processing route that circumvents the limitations of conventional HPS. Gao *et al.* [105] further validated these compositional-design principles using Sm/Pr co-doping. A suitable amount of Pr^{3+} increases the R phase fraction and improves lattice ordering, whereas Sm^{3+} maintains heterogeneity and domain

mobility. This cooperative interaction yields a transmittance of 64.1% at 900 nm and a d_{33} of 1310 pC N^{-1} (Fig. 11(b)). These results collectively indicate that rational combinations of rare-earth dopants offer an effective strategy for simultaneously optimizing the transparency and piezoelectric response of PMN–PT ceramics.

High-component solid-solution design provides an effective route to enhance the thermal stability of PMN–PT-based transparent ceramics. Introducing high T_c components such as $Pb(In,Nb)O_3$ (PIN) or $Pb(Zn,Nb)O_3$ (PZN), increase phase stability and suppress temperature-induced polarization degradation. Compared with the binary PMN–PT system, the ternary $Pb(In,Nb)O_3$–$Pb(Mg_{1/3}Nb_{2/3})O_3$–$PbTiO_3$ (PIN–PMN–PT) composition benefits from multicomponent solid-solution effects that intrinsically enhance thermal robustness. On this basis, rare-earth doping further optimizes domain structure and enables simultaneous improvements in d_{33} and transmittance. Fu *et al.* [20] demonstrated this strategy by preparing La^{3+}-doped 24PIN–42PMN–34PT ceramics, achieving 66.2% transmittance at 1600 nm and a d_{33} of 1012 pC N^{-1}. Even near the T_c, the performance decreased by only 26.8% (Fig. 11(c)), confirming the strong thermal stability endowed by the high-PIN content. The coexistence of fine striped and ripple-like domains minimizes scattering and enhances polarization reversibility. Similarly, Zheng *et al.* [64] obtained 63% transmittance at 2500 nm and d_{33} = 905 pC N^{-1} in Sm-doped PIN–PMN–PT ceramics, accompanied by a marked increase in T_c and improved ferroelectric stability at elevated temperatures. Qi *et al.* [131] further reported Sm^{3+}-doped 26PIN–46PMN–28PT ceramics with d_{33} = 1023 pC N^{-1}, 65.1% transmittance at 1800 nm, and $T_c \approx 116$°C. Transparent ultrasonic transducers fabricated from this material delivered echo amplitudes about 1.5 times those of LN single crystals, demonstrating their potential for photoacoustic imaging. Fan *et al.* [133] further applied Sm^{3+}/La^{3+} co-doping to 25PIN–41PMN–34PT ceramics, achieving synergistic enhancement with T_c = 172 °C, d_{33} = 730 pC N^{-1}, and transmittance of about 56% in the near-infrared region. Collectively, these studies highlight that incorporating high T_c components fundamentally improves the thermal stability of PMN–PT based

transparent ceramics, whereas rare-earth doping provides additional domain-structure optimization. The combination of multicomponent design and targeted dopant engineering offers a powerful strategy for next-generation transparent piezoelectric devices.

Regulation of domain structures is a key factor governing the transmittance and d_{33}. Adjusting domain size, domain morphology and local lattice distortion can effectively tailor light scattering, polarization rotation and domain-wall mobility. Rare-earth doping provides an efficient approach for achieving such domain engineering. Regarding domain-size control, Qin *et al.* [73] demonstrated that Pr^{3+} doping significantly refines watermark domains. In Pr-doped 75PMN–25PT, the average watermark-domain size was below 200 nm, far smaller than the visible wavelength. This reduction in scattering results in 68% transmittance at 900 nm and a d_{33} of 850 pC N^{-1} (Fig. 11(d)). Pr^{3+} also promotes a minor T phase, increases the c/a ratio and enhances reversible domain rotation, enabling simultaneous improvements in d_{33} and transmittance. In contrast, Yan *et al.* [60] highlights the regulation of domain types**.** In 2.5 mol% Eu^{3+}-doped 72PMN–28PT, highly ordered parallel stripe domains formed, producing nearly twice the piezoelectric amplitude of watermark domains and requiring a lower switching voltage. The ceramics exhibited a high d_{33} of 1400 pC N^{-1} and 68% transmittance at 900 nm, approaching single-crystal behavior (Fig. 11(e)). PFM measurements confirmed that optimizing domain configurations plays a decisive role in enhancing the electromechanical response. Additional studies, Eu-doped 75PMN–25PT (transmittance ≈ 51% at 800 nm, d_{33} = 850 pC N^{-1}, d_{33}^* = 1520 pmV^{-1}) reported by Li *et al.* [90], and La-doped 75PMN–25PT (transmittance ≈ 69% at 1550 nm, d_{33} ≈ 450 pC N^{-1}, with uniform layered domains) reported by Hu *et al.* [58], further demonstrate that rare-earth ions can tune both domain size and domain morphology by modifying local lattice distortions. Such domain engineering enables coordinated improvement in d_{33} and transmittance.

For transparent piezoelectric ceramics, domain engineering should be viewed as a coupled regulation of optical scattering and polarization dynamics. Coarse ferroelectric domains and non-180°

domain walls introduce refractive-index discontinuities and act as optical scattering centers, whereas nanoscale domains or PNRs reduce optical anisotropy and improve in-line transmittance. However, domain walls and phase-boundary structures are also important contributors to extrinsic piezoelectricity, because they facilitate polarization rotation and reversible domain-wall motion. Therefore, the optimal domain state is not the complete elimination of domain walls, but a controlled domain configuration with reduced optically active scattering and sufficient polarization mobility. This explains why watermark-like, stripe-like, or nanoscale domain structures in rare-earth-doped PMN–PT can simultaneously improve transparency and d_{33}, whereas excessive field-induced domain alignment may increase scattering and reduce optical transmittance.

External electric fields can exert a significantly influence on the optical and electromechanical properties of transparent ceramics by reconstructing ferroelectric domain structures. In this context, Guo *et al.* [141] reported a strong influence of poling on transparency. In Pr-doped 75PMN–25PT ceramics, direct-current poling (DCP, 3.8 kV cm^{-1} for 20 min) induced extensive layered domains aligned with the electric field, reducing the transmittance at 900 nm from 68% to 20%; after thermal depoling at 130°C for 5 min, uniform high transparency was recovered (Fig. 11(f)). This observation demonstrates that domain reconstruction strongly affects optical performance, and provides important insight into the coupling between the electric field and transparency. Beyond the behavior observed under DCP, increasing attention has been directed toward how ACP regulates domain evolution in ferroelectric systems, where markedly different responses have been identified in single crystals and ceramics. In [001]-oriented PMN–PT single crystals, ACP significantly reduces the density of 71° domain walls and enlarges 109° domains to the millimeter scale. This transformation eliminates light-scattering interfaces and enables near-theoretical transparency together with an enhanced d_{33} exceeding 2100 pC N^{-1} [128]. In contrast, ACP in PMN–PT ceramics tends to refine domains and increase domain-wall density because of grain-boundary constraints and strong random fields. The resulting enhancement in piezoelectric response primarily arises from the increased

contribution of mobile domain walls, and dynamic-scaling analyses indicate that optimized ACP parameters can produce a high d_{33} of approximately 1390 pC N^{-1} within only several seconds (Fig. 11(g)) [142]. Taken together, these findings reveal that ACP drives domain coarsening and the removal of scattering-type walls in PMN–PT single crystals, whereas it induces domain refinement and increased wall density in ceramics, leading to entirely opposite trends in the regulation of transmittance and d_{33}. This pronounced system-dependent divergence highlights the complex interplay between external fields and microstructural constraints, and the underlying physical origin remains to be fully clarified.

Overall, recent progress in PMN–PT transparent ceramics establishes a comprehensive framework for property optimization through multiscale domain engineering. Single rare-earth doping modulates local lattice distortion and tailors domain size and morphology, enabling simultaneous enhancement of transmittance and d_{33}. Co-doping strategies integrate the complementary roles of different rare-earth ions, achieving a balanced improvement between transmittance and d_{33}. Incorporating high T_c components stabilizes the ferroelectric phase at elevated temperatures, while rare-earth modification provides additional flexibility for domain-structure refinement, yielding ceramics with superior thermal robustness. Meanwhile, external-field poling directly reconstructs domain architecture, revealing the intrinsic sensitivity of optical transparency and electromechanical coupling to domain-wall density and configuration in both single crystals and ceramics. Together, these advancements highlight the strong interplay among composition design, domain engineering and field-driven modulation, establishing an effective materials-design paradigm for next-generation transparent piezoelectric devices.

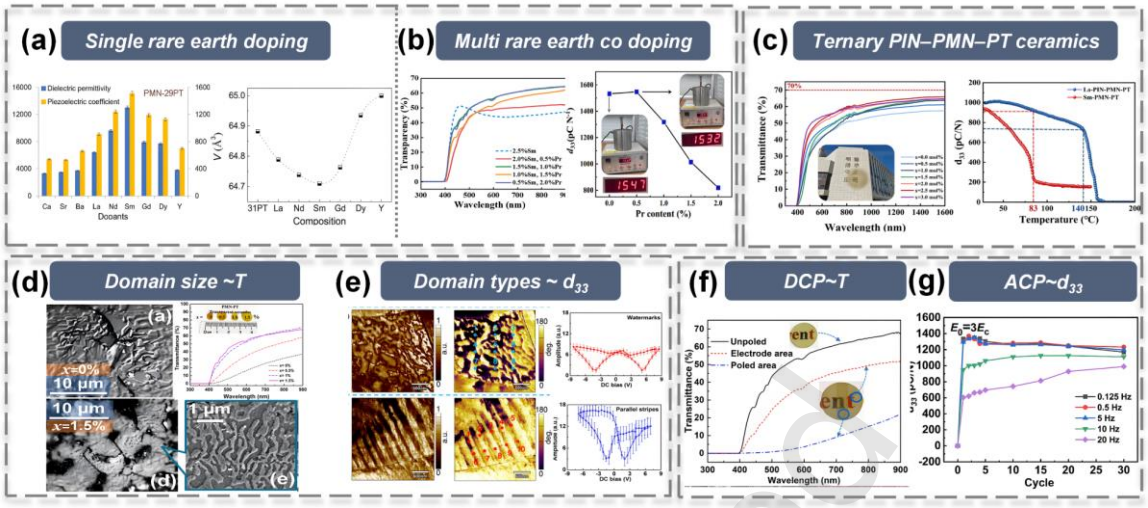

Fig. 11. Performance modulation strategies for PMN–PT-based transparent piezoelectric ceramics. (a) Different rare-earth dopants regulate the d_{33}. Reproduced with permission from Ref. [66], © American Physical Society 2020. (b) Co-doping with multiple rare-earth ions tunes the optoelectric properties of the ceramics. Reproduced with permission from Ref. [105], © Elsevier BV 2025. (c) Optoelectric properties and thermal stability of multicomponent ceramics. Reproduced with permission from Ref. [20], © American Institute of Physics 2024. (d) The influence of domain size on transmittance. Reproduced with permission from Ref. [73], © Elsevier BV 2022. (e) The influence of domain types on d_{33}. Reproduced with permission from Ref. [60], © American Chemical Society 2021. (f) The influence of ACP on transmittance. Reproduced with permission from Ref. [141], © Elsevier BV 2024. (g) The influence of DCP on d_{33}. Reproduced with permission from Ref. [142], © Japan Society of Applied Physics 2023.

3.1.3. Progress and Optimization Strategies in KNN

As an environmentally friendly, lead-free system, KNN has attracted growing attention in transparent piezoceramics. Early KNN ceramics required high sintering temperatures and showed coarse grain growth, making it difficult to achieve both high transmittance and strong piezoelectric response. Recent advances have significantly improved the performance of KNN-based transparent piezoelectric ceramics by using advanced sintering techniques and targeted elemental regulation. Representative progress is shown in Fig. 12, and detailed metrics are summarized in Table 1.

Fig. 12. Research progress on KNN-based transparent piezoelectric ceramics.

Advanced sintering techniques, including hot pressing and hot-isostatic pressing, have been widely adopted for fabricating KNN-based transparent piezoelectric ceramics. By enhancing densification and precisely controlling grain size, these techniques markedly improve both transmittance and piezoelectric performance. Using HPS, Kwok *et al.* achieved dense and fine-grained $(K_{0.5}Na_{0.5})_{0.95}Li_{0.05}Nb_{0.95}Bi_{0.05}O_3$ (KNLNB) ceramics with grain sizes below 400 nm, a transmittance of about 60% at 900 nm, and d_{33} = 64 pC N^{-1} [70]. Geng *et al.* [115] demonstrated that combining hot pressing with Sr^{2+}/Ba^{2+} co-doping refined grains (< 1 μm) and increased density (> 94%), producing transparent $[(K_{0.5}Na_{0.5})_{1-x}(Sr_{0.75}Ba_{0.25})_x]_{0.93}Li_{0.07}Nb_{0.93}Bi_{0.07}O_3$ (KNLNB-Sr/Ba) ceramics with 60% transmittance at 900 nm and d_{33} = 151 pC N^{-1} (Fig. 13(a)). In recent years, additive manufacturing has been applied to KNN-based transparent piezoelectric ceramics, enabling complex architectures and multifunctional integration. Chen *et al.* [138] fabricated 0.5 mol% Er_2O_3-doped lead-free KNNLN transparent ceramics via stereolithography (SLA) 3D printing. After sintering at 1120 °C for 6 h, the ceramics exhibited about 34% transmittance (550–800 nm), d_{33} = 97 pC N^{-1}, and thickness electromechanical coupling coefficient (k_t) of about 0.36, along with pronounced upconversion luminescence. Structural analysis revealed coexistence of O and T phases, with the phase ratio tunable by sintering time. The transparent transducer fabricated from this material operated at 10.5 MHz, showing strong ultrasonic echoes and enabling multimodal imaging

that combined ultrasound, photoacoustic, and fluorescence modes (Fig. 13(b)). This study demonstrated the potential of rare-earth–doped KNN-based ceramics for multimodal medical imaging and integrated microsystems and verified the feasibility of 3D printing for constructing complex transparent piezoelectric ceramics.

Elemental doping to tailor the phase structure, domain configuration, and grain size of KNN-based transparent piezoelectric ceramics is a primary strategy for improving their optical and electrical properties. Common A-site dopants include Sr, Ca, and Ba, whereas typical B-site dopants include Sc, Al, and Zr. For example, Yang *et al.* [136] introduced $Ca(Sc_{0.5}Nb_{0.5})O_3$ into $(K_{0.37}Na_{0.63})NbO_3$ to produce pseudo-cubic KNN–CSN transparent ceramics with grain sizes below 1 μm and 98% density, achieving ~60% transmittance and d_{33} = 38 pC N^{-1}. Zhao *et al.* [106, 107] used $Sr(Sc_{0.5}Nb_{0.5})O_3$ (SSN) and $Sr(Al_{0.5}Nb_{0.5})O_3$ (SAN) to tune the KNN phase toward an orthorhombic structure while maintaining submicron grains, yielding KNN–SSN ceramics (transmittance = 70% at 780 nm, d_{33} = 101 pC N^{-1}) and KNN–SAN ceramics (transmittance = 55% at 780 nm, d_{33} = 105 pC N^{-1}). Li *et al.* [143] reported that Sm^{3+} doping in KNN-based ceramics introduced PNRs, refined grains, and reduced domain-wall density, thereby reducing optical scattering. At the optimal doping level, a desirable balance between transparency and piezoelectricity was achieved (Fig. 13(c)).

Constructing polymorphic phase boundary is one of the most commonly used and effective strategies for enhancing the piezoelectric performance of KNN-based TFCs. Most reported KNN TFCs are limited to single O, T, or P phases, or to two-phases coexistence regions such as O–T or T–P phases. The lack of morphotropic or polymorphic phase boundary leads to lower d_{33}, typically below 200 pC N^{-1}. In contrast, high- piezoelectric performance KNN ceramics typically occur near the R–T or R–O–T phase boundaries. Studies have shown that elements such as Li, Ag, Bi, Ta, and Sb, as well as complex perovskites like ABO_3 (A = Sr, Ba, Ca; B = Ti, Zr), $(Bi_{0.5}Na_{0.5})MO_3$ (M = Zr, Ti, Hf), and $BiMO_3$ (M = Al, Fe, Sc), can lower T_{O-T} [144-149]. Conversely, dopants such as Ta, Sb, A ZrO_3 $AZrO_3$ (A = Sr, Ba, Ca), and $BiMO_3$ (M = Fe, Sc) can raise T_{R-O} [144-149]. Careful chemical

modification and optimized sintering conditions can produce uniform polar regions and phase coexistence, greatly enhancing the piezoelectric response. Based on this concept, Ren *et al.* [33] developed $0.93K_{0.5}Na_{0.5}NbO_3$–$0.07SrZrO_3$ (KNN–SZ) ceramics using Li_2O as a sintering aid. Li_2O addition promoted grain growth (~510 nm) and induced O–T phase coexistence (Fig. 13(d)), yielding high-performance transparent ceramics with 70% transmittance at 750 nm and d_{33} = 150 pC N^{-1}. Lin *et al.* [28] fabricated $0.99K_{0.5}Na_{0.5}Nb_{(1-x)}O_3$–$0.01Bi(Ni_{2/3}Nb_{1/3})O_3$-6 mol%$Ta^{5+}$ (KNN–BNN-Ta) ceramics via conventional pressureless sintering. Ta^{5+} incorporation promoted O–T phase coexistence, produced uniform grains (~280 nm) and complex nanoscale domains (Fig. 13(e)), achieving 60% transmittance at 900 nm and d_{33} = 185 pC N^{-1}. Building on these findings, Lin *et al.* [139] proposed a multiscale reconstruction strategy based on A/B-site co-doping. In the $(Tb_{0.01}Li_{0.07}K_{0.45}Na_{0.45})(Ta_{0.06}Sb_{0.03}Nb_{0.91-x}Sc_{5x/3})O_3$ (TLKN–TSN-*x*Sc) system, compositional tuning and densification control induced O–T phase coexistence, submicron grains, and nanoscale striped domains, yielding a balanced combination of transmittance and d_{33}. The optimized sample exhibited ~53% transmittance at 800 nm, $d_{33} \approx$ 180 pC N^{-1}, $K_p \approx$ 34%, and $T_c \approx$ 332°C, along with excellent thermal stability and device sensitivity. More recently, Lin et al. [140] further constructed a tetragonal–pseudocubic (T–P) phase boundary in KNN-based transparent ceramics through Ta doping, enabling the synergistic regulation of average lattice symmetry and local polarization response. This strategy improved optical transparency by increasing structural symmetry, while P phase-induced local polarization disorder, manifested as PNRs, provided field-responsive local polar units to maintain piezoelectric activity. The optimized d $(K_{0.465}Na_{0.465}Li_{0.07}Tb_{0.01})(Nb_{0.93}Bi_{0.07})O_3$-Ta (KNTL–NB-Ta) ceramic achieved a transmittance of approximately 72% at 780 nm and a d_{33} of 157 pC N^{-1}, showing an excellent balance between transparency and piezoelectricity. These findings provide new insights into the practical development of transparent piezoelectric ceramics.

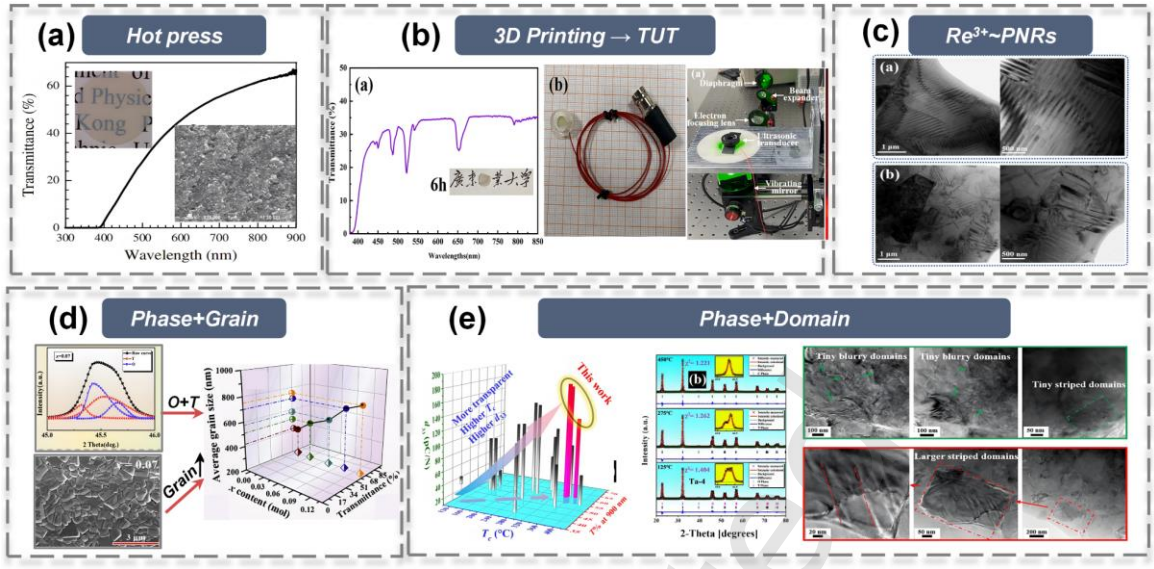

Fig. 13. Effects of doping and processing regulation on the properties of KNN-based transparent piezoelectric ceramics. (a) Hot-pressed KNN transparent piezoelectric ceramics. Reproduced with permission from Ref. [70], © Elsevier 2012. (b) 3D-printed KNN transparent piezoelectric ceramics and their applications. Reproduced with permission from Ref. [138], © Elsevier Ltd 2024. (c) Influence of polar nanoregions on material performance. Reproduced with permission from Ref. [143], © Elsevier BV 2023. (d) Effects of phase boundaries and grain size on optical and electrical properties. Reproduced with permission from Ref. [33], © Elsevier BV 2020. (e) Regulation of phase structure, grain size, and domain configuration for optimizing the optoelectric performance of KNN ceramics. Reproduced with permission from Ref. [28], © Elsevier Ltd 2022.

3.1.4. Summary

PMN–PT-based TFCs currently lead in absolute piezoelectric performance, with performance metrics rivaling those of single crystals, making them attractive for demanding applications such as transparent ultrasonic transducers and high-sensitivity biomedical imaging probes, where large d_{33}, high sensitivity, and strong electromechanical coupling are required. KNN-based ceramics, while still developing, offer a compelling lead-free alternative with steadily improving performance and better environmental compatibility. They are therefore more suitable for green, scalable, and environmentally regulated transparent piezoelectric components, although their piezoelectric coefficients are still generally lower than those of PMN–PT-based counterparts. From the perspective

of multifunctional coupling, transparent piezoelectric ceramics clearly illustrate the trade-off between optical transparency and electromechanical activity. For PMN–PT, rare-earth-induced domain refinement and MPB-related polarization rotation can simultaneously improve transmittance and d_{33}, but excessive domain-wall density or field-induced domain alignment may enhance scattering. For KNN, submicron grains and O–T/R–O–T polymorphic phase boundaries improve transparency and polarization rotation, but excessive disruption of long-range ferroelectric order may weaken macroscopic piezoelectricity. Thus, transparent piezoelectric ceramics require coordinated control of grain/domain structure and phase-boundary engineering rather than independent optimization of optical or electrical properties.

3.2. Transparent Electro-Optic Ceramics

3.2.1. Electro-Optic Mechanisms and Application Scenarios

The electro-optic (EO) effect is the change in refractive index under an applied electric field, as illustrated in Fig. 14 [150]. In general, the refractive index can be expressed as:

$$n = n^0 + aE + bE^2 \tag{6}$$

where n^0 is the refractive index in the absence of an external field, and a and b are material constants. The linear term aE corresponds to the first-order EO effect (Pockels effect), and the quadratic term bE^2 corresponds to the second-order EO effect (Kerr effect). Changes in refractive index can be characterized by monitoring variations in transmitted intensity under an applied voltage.

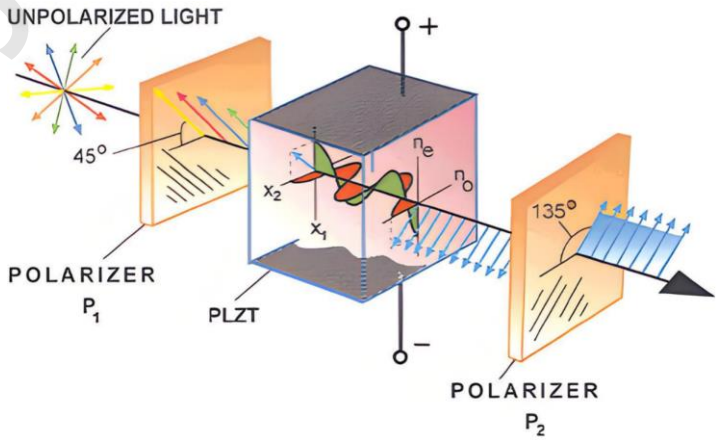

Fig. 14. Schematic illustration of the electro-optic effect principle. Reproduced with permission from Ref. [150], © Wiley-Blackwell 1999.

Transparent electro-optic materials combine high transparency with strong electro-optic activity and are widely used in components such as EO switches, modulators, polarization controllers, tunable filters, and variable optical attenuators, playing key roles in optical communication, sensing, and photonics [34-36]. Typical materials include single crystals such as LN, BBO, KDP, and RTP, as well as PLZT and PMN–PT-based ceramics and single crystals. Among these, LN-based phase modulators, Mach–Zehnder modulators, and microring-resonator modulators have been commercialized and are widely deployed. Among ceramic electro-optic materials, PLZT is one of the most classical transparent electro-optic ceramics and has long been used as a benchmark for electro-optic modulation. However, compared with PMN–PT and KNN systems, its recent development has been more concentrated on electro-optic applications rather than broad multifunctional coupling involving piezoelectricity, energy storage, luminescence, and photochromism. Therefore, in this review, PLZT is discussed mainly as a representative electro-optic material, whereas PMN–PT and KNN are emphasized as the main multifunctional transparent ferroelectric ceramic systems.

More recently, various devices based on transparent PMN–PT EO ceramics have been developed. Tunable optical attenuators exhibit low insertion loss and sub-microsecond response; dynamic polarization controllers achieve low polarization-dependent loss (PDL) and fast modulation; EO Q-switches generate high-repetition-rate pulses (>200 kHz) at drive voltages of only a few tens of volts; and tunable optical filters show nanosecond-scale response with precise wavelength selectivity. The overall performance of these devices approaches, and in some cases surpasses, that of commercial single-crystal components. Efficient EO modulation places stringent requirements on materials, which must provide a large EO coefficient, fast response, and high optical homogeneity. Therefore, precise control of microstructural uniformity and grain-boundary characteristics is essential to optimize the electro-optic performance of transparent ferroelectric ceramics.

Compared with conventional EO crystals, transparent ferroelectric ceramics offer greater processing flexibility and lower fabrication cost while maintaining high transparency, demonstrating strong application potential. Classical PLZT ceramics have provided early and representative examples of ceramic-based EO devices. For instance, PLZT EO ceramic deflectors have been used for intracavity beam steering in external-cavity diode lasers, achieving a beam deflection angle of 5.8 mrad at 1000 V and a switching time below 120 ns [151]. PLZT-based shutters have also been demonstrated for free-space optical fiber switching, where a 1 × 6 fiber-ribbon switching architecture showed reliable operation at Gb/s-level link speeds [152]. These examples indicate that PLZT remains an important benchmark for transparent ceramic EO modulation, especially in shutters, beam deflectors, and optical switching components. More recently, various devices based on transparent PMN–PT EO ceramics have been developed. Tunable optical attenuators exhibit low insertion loss and sub-microsecond response; dynamic polarization controllers achieve low polarization-dependent loss (PDL) and fast modulation; EO Q-switches generate high-repetition-rate pulses (>200 kHz) at drive voltages of only a few tens of volts; and tunable optical filters show nanosecond-scale response with precise wavelength selectivity. The overall performance of these devices approaches, and in some cases surpasses, that of commercial single-crystal components. Efficient EO modulation places stringent requirements on materials, which must provide a large EO coefficient, fast response, and high optical homogeneity. Therefore, precise control of microstructural uniformity and grain-boundary characteristics is essential to optimize the electro-optic performance of transparent ferroelectric ceramics.

3.2.2. Progress and Optimization Strategies in PMN–PT

In the PMN–PT system, research on transparent electro-optic ceramics began in the 1990s. Early samples typically showed about 40% transmittance, which was below practical device requirements. As chemical co-precipitation and uniaxial HPS matured along with A-site rare-earth doping (e.g., La, Sm) and controlled excess PbO, PMN–PT transparent ceramics achieved ~65%

near-infrared transmittance and an electro-optic coefficient up to 66×10^{-16} m^2 V^{-2} (Fig. 15). The detailed performance of transparent electro-optical ceramics are summarized in Table 2.

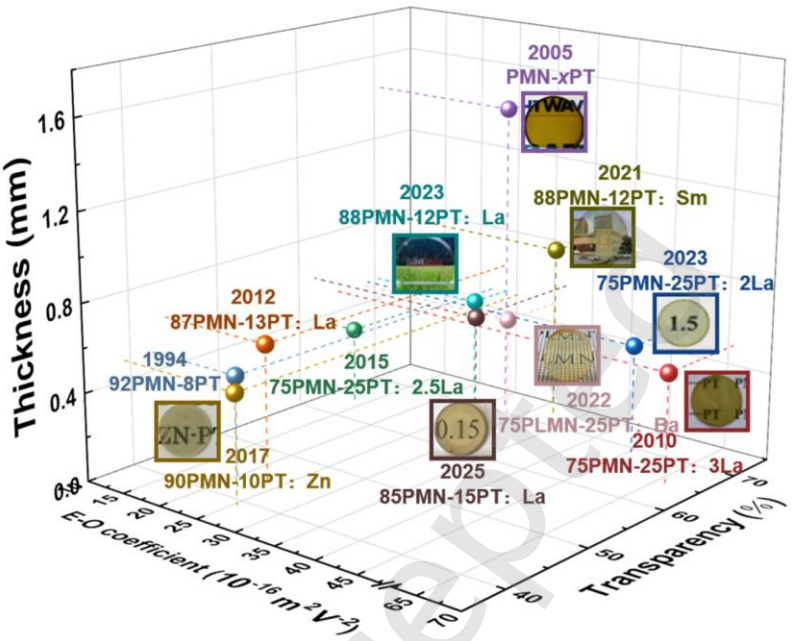

Fig. 15. Research progress on PMN–PT transparent electro-optic ceramics.

Table 2. Detailed performance of transparent electro-optic ceramics

Classification	Component	Transmittance [%]	Wavelength [nm]	Thicknesses[mm]	*E-O* Effect	*E-O* Coefficient	Refs.
Lead based	88PMN–12PT	49	633	0.5--	Quadratic	22×10^{-16} m^2 V^{-2}	[153]
	PMN–PT	70	1550	1.45	Quadratic	28×10^{-16} m^2 V^{-2}	[59]
	75PMN–25PT	65	1800	0.5	Quadratic	66×10^{-16} m^2 V^{-2}	[154]
	PLMN–13PT	50	1100	0.63	Quadratic	23.7×10^{-16} m^2 V^{-2}	[155]
	PLMN–25PT	62	632	0.35	Quadratic	40.6×10^{-16} m^2 V^{-2}	[156]
	La-75PMN–25PT	65	1100	0.35	Quadratic	13.45×10^{-16} m^2 V^{-2}	[157]
	Zn-90PMN–10PT	44	2000	0.5	Quadratic	25.5×10^{-16} m^2 V^{-2}	[158]
	Sm-88PMN–12PT	69.6	900	0.85	Quadratic	35×10^{-16} m^2 V^{-2}	[5]
	Ba-PLMN-25PT	68	1100	0.5	Quadratic	30.4×10^{-16} m^2/V^2	[159]
	La-75PMN–25PT	69	1550	0.5	Quadratic	45.4×10^{-16} m^2 V^{-2}	[58]
	La-88PMN–12PT	70.5	900	0.5	Quadratic	23.6×10^{-16} m^2 V^{-2}	[114]
	Sm-PIN–PMN–PT	63	2500	0.4	Linear	814 pm V^{-1}	[64]
	La-85PMN–PT	60	1500	0.6	Quadratic	35×10^{-16} m^2 V^{-2}	[57]
	La-67PMN–33PT	67	1800	0.5	Linear	1417 pm V	[132]
Lead	KNN–ST	--	--	0.173	Quadratic	1.65×10^{-17} m^2 V^{-2}	[160]

free	KNNB	60	800	0.5	Linear	42 pm V^{-1}	[94]
	KNLNB-Bi	60	900	0.5	Linear	102 pm V^{-1}	[70]
	KNLNB-HP	58	900	0.5	Linear	198 pm V^{-1}	[71]
	KNLNB-NP	70	900	0.5	Linear	30 pm V^{-1}	[95]
	KNNT-Bi	51.5	633	0.5	Linear	26.1 pm V^{-1}	[161]
	KNLNB-Er	60	900	0.3	Linear	128 pm V^{-1}	[116]
	KNN–BNN-Ta	60	900	0.3	Linear	84 pm V^{-1}	[28]

Experimental studies show that rare-earth ion doping reduces ferroelectric domain size and improves crystal structure, resulting in faster electro-optic response and significantly enhanced modulation efficiency. At the device level, PMN–PT transparent ceramics used in high-efficiency EO switches and modulators exhibit switching times on the order of tens of nanoseconds, much faster than conventional EO materials. These materials show great potential for high-speed optical communication, optical switching, and free-space optical transmission. In summary, PMN–PT transparent EO ceramics have achieved notable breakthroughs in both transmittance and EO coefficient. To elucidate the mechanisms underlying these improvements, this review focuses on the logical progression from composition selection to compositional tuning, microstructural evolution, and external-field regulation, clarifying the correlation between material design and performance optimization.

The EO performance of PMN–PT ceramics strongly depends on the PT content, which defines the phase region or boundary and thereby influences the EO response. Uchino *et al.* [153] first compared PLZT and (1–*x*)PMN–*x*PT transparent ceramics and found that 88PMN–12PT exhibited an EO coefficient of about 22×10^{-16} m^2 V^{-2}, nearly twice that of PLZT. Subsequent work by Londono *et al.* [155] confirmed that PMN-rich compositions with ~12–13% PT exhibit the strongest EO response (Fig. 16(a)) . Ruan *et al.* [154] later reported La-doped 0.75PMN–0.25PT ceramics fabricated by two-step sintering, achieving ~65% infrared transmittance and an exceptionally high EO coefficient of 66×10^{-16} m^2 V^{-2}, far exceeding conventional compositions. Domain-structure

analysis revealed that this composition lies near the critical boundary between relaxor and ferroelectric states, where an external field easily induces a phase transition accompanied by a large refractive-index change, producing a giant Kerr-type EO effect. Based on these findings, the design principle of the "critical phase region leading to maximum EO response" was established [113]. Recent studies have further expanded this understanding. Shi *et al.* [57] observed that in 75PMN–25PT and 80PMN–20PT ceramics, the EO coefficient peaks at 60–90°C, whereas in 85PMN–15PT and 90PMN–10PT it decreases monotonically with temperature. These results indicate strong coupling between composition, phase-transition behavior, and EO activity.

A-site rare-earth doping has been proved to effectively optimize lattice and domain structures, and plays a crucial role in enhancing electro-optic performance of PMN–PT transparent ceramics. Ruan *et al.* [154] reported that La doping suppresses defect formation, increases densification, and significantly enhances both transmittance and EO response. Londono *et al.* [155] further confirmed that La incorporation prevents pyrochlore formation and stabilizes a single pseudocube phase. The 0.63 mm-thick sample showed 49% transmittance and an EO coefficient of 23.7×10^{-16} m^2 V^{-2}. Ji *et al.* [157] reported an "optimal window" for La doping, with the highest EO coefficient (13.45×10^{-16} m^2 V^{-2}) at 2.5 mol% doping content; excessive doping causes lattice mismatch and defect accumulation, reducing performance (Fig. 16(b)). Sm doping also shows outstanding performance. Fang *et al.* [5] fabricated Sm-88PMN–12PT ceramics with ~69.6% transmittance at 0.85 mm thickness and an EO coefficient of about 35×10^{-16} m^2 V^{-2}, successfully demonstrating optical communication for audio and image transmission (Fig. 16(b)). Hu *et al.* [58] prepared La-0.75PMN–0.25PT ceramics with ~69% transmittance at 0.50 mm thickness, and observed parallel layered domains promote rapid polarization switching, yielding a high EO coefficient of 45.4×10^{-16} m^2 V^{-2}. Tian *et al.* [114] achieved 70.5% transmittance at 0.50 mm thickness, an EO coefficient of 23.6×10^{-16} m^2 V^{-2}, and an extinction ratio of 34 dB in La-88PMN–12PT ceramics, demonstrating polarization control and dual-channel optical communication.

B-site regulation and controlled PbO excess have also proven effective for enhancing EO performance. In 90PMN–10PT transparent ceramics, Fujii *et al.* [158] achieved > 40% transmittance and an EO coefficient of 25.5×10^{-16} m^2 V^{-2} by substituting Zn for Mg at B site. This enhancement was attributed to the composition being near a critical phase transition region, where the material is highly sensitive to external electric fields (Fig. 16(c)). Ji *et al.* [156] found that when increasing PbO from 10 to 20 mol% in La-75PMN–25PT transparent ceramics, the grain size enlarged from 3–5 μm to >7 μm, and raising the EO coefficient from 22.9×10^{-16} to 40.6×10^{-16} m^2 V^{-2} (Fig. 16(c)). Similarly, Tian *et al.* [114] reported that an appropriate PbO excess (10mol%) improves densification and transmittance (~70.5%) while increasing the EO coefficient to 23.6×10^{-16} m^2 V^{-2}.

Microscopic domain structure and phase-transition behavior are key factors governing EO performance in PMN–PT transparent ceramics. Ruan *et al.* [113, 154] observed typical "fingerprint-like" nanodomains in La-doped 75PMN–25PT, where nanoscale domain configurations reduce the energy barrier for field-induced phase transitions. This facilitates domain reorientation and produces a strongly amplified Kerr-type EO response. Hu *et al.* [58] further demonstrated the potential of domain engineering by identifying "parallel layered" domain structures, whose ordered alignment enables rapid polarization switching and yields an ultrahigh EO coefficient of 45.4×10^{-16} m^2 V^{-2} (Fig. 16(d)). Taken together, these findings indicate that domain-structure regulation plays a dominant role in EO enhancement within the conventional domain-mediated framework, providing effective pathways for performance optimization through domain engineering, phase-transition design, and polarization mobility control. Beyond conventional domain engineering, in which EO enhancement is often constrained by domain-wall dynamics, Jiang *et al.* [132] demonstrated that further EO optimization in PMN–PT transparent ceramics can arise from atomistic polarization mechanisms. Transmission electron microscopy combined with first-principles calculations revealed localized atomistic polar structures in La-doped PMN–PT, which remain responsive to electric fields at optical frequencies (Fig. 16(e)). As a result, an ultrahigh linear EO coefficient of approximately 1417 pm V^{-1}

was reported, suggesting a new route for EO optimization beyond domain-mediated effects.

External parameters such as temperature and electric field offer additional way to tune the EO response of PMN–PT. Ruan *et al*. [113] reported that applying a DC bias to a critical composition triggers a phase transition between ferroelectric and relaxor states, producing an abrupt refractive-index change and a giant Kerr effect (Fig. 16(f)). Shi *et al*. [57] systematically clarified the temperature dependence: the EO coefficient in 75PMN–25PT and 80PMN–20PT transparent ceramics first increases then decreases with temperature,, and the maximum EO coefficient corresponds to the coexistence of multiphase and a field-induced ferroelectric–ferroelectric phase transition. While in 85PMN–15PT and 90PMN–10PT, no field-induced phase transition occurred and the EO coefficient decreases monotonically (Fig. 16(g)). These results highlight the crucial role of external-field control in optimizing transparent PMN–PT ceramics and provide a theoretical foundation for designing stable EO devices under complex operating conditions.

Beyond ceramic systems, a major breakthrough has recently been achieved in [011]-poled PIN–PMN–PT single crystals. Through synergistic control of ferroelectric phase, crystal orientation, and poling strategy, light-scattering domain walls were effectively removed, resulting in an ultrahigh transmittance of 99.6% at 1064 nm (with antireflection coating) together with a giant electro-optic response ($r_{33} \approx 900$ pm V^{-1} at room temperature). This performance surpasses that of conventional EO crystals such as $LiNbO_3$ and DKDP by more than one order of magnitude. The enhanced EO activity is attributed to electric-field-induced polarization rotation along the nonpolar [011] direction near the morphotropic phase boundary, where the flattened free-energy landscape amplifies ionic and piezoelectric contributions. This work establishes a new paradigm for achieving both high transparency and giant EO response in relaxor-based single crystals [37].

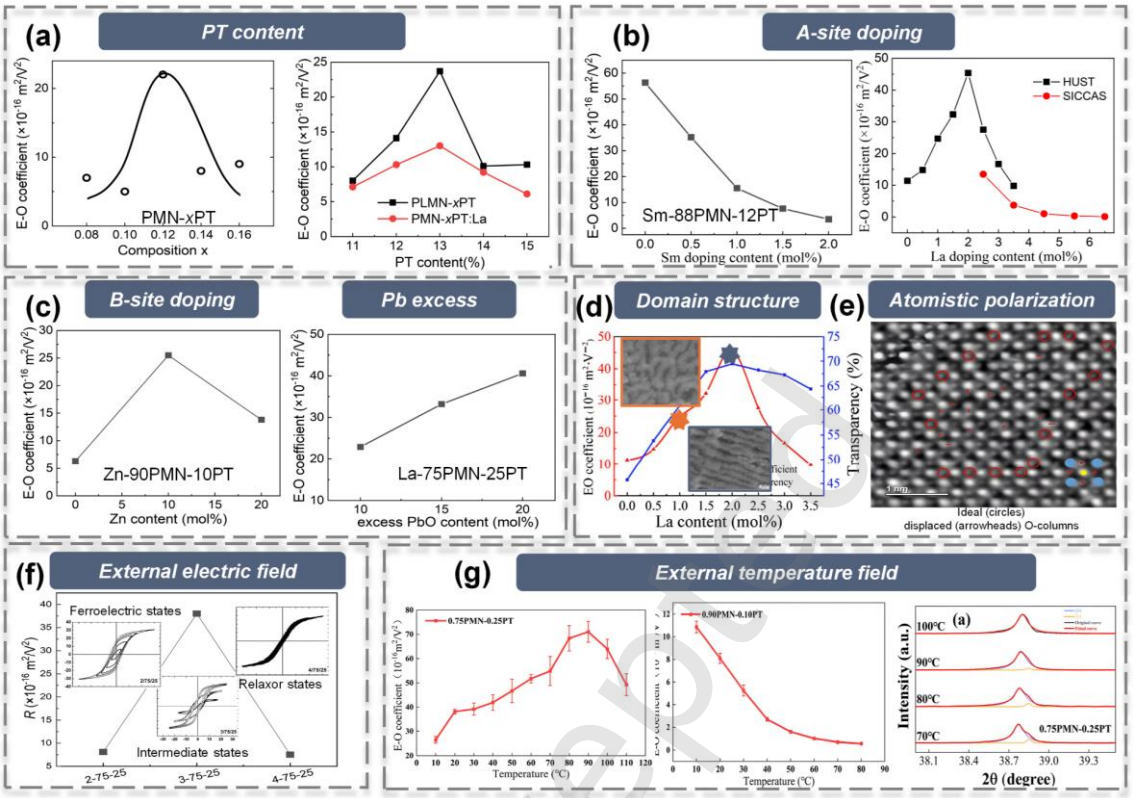

Fig. 16. Principal strategies for tuning the electro-optic coefficient of PMN–PT transparent ceramics: (a) influence of PT content on the electro-optic coefficient; Reproduced with permission from Ref. [153, 155], © Elsevier Ltd 1995; Scientific Research Publishing 2012. (b) optimization of transmittance and electro-optic performance via A-site doping; Reproduced with permission from Ref. [5, 157], © John Wiley and Sons Inc 2021; Elsevier Ltd 2012. (c) effects of B-site doping and excess PbO on electro-optic performance; Reproduced with permission from Ref. [156, 158], © Trans Tech Publications Ltd 2013; American Institute of Physics 2017. (d) impact of domain structure on electro-optic properties; Reproduced with permission from Ref. [58], © Tsinghua University Press 2023. (e) iDPC-TEM (integrated differential phase-contrast transmission electron microscopy) image of oxygen-column displacements in La-doped PMN–PT.; Reproduced with permission from Ref. [132], © American Chemical Society 2025. (f) bias-induced phase transition; Reproduced with permission from Ref. [113], © American Institute of Physics 2011. (g) temperature-dependent multiphase cooperation and performance enhancement. Reproduced with permission from Ref. [57], © American Institute of Physics 2025.

3.2.3. Progress and Optimization Strategies in KNN

Compared with the PMN–PT system, research on KNN-based transparent EO ceramics began later but shows clear potential. Because KNN compositions tend to form multiphase coexistence

during solid-solution processing, controlling the refractive index and EO coefficients remains challenging. Recent studies achieved high transmittance in the visible and near-infrared regions, along with moderate EO effects, by optimizing sintering routes such as hot pressing and pressureless sintering combined with moderate excess dopants. Reported linear EO coefficients range from several tens to over 100 pm V^{-1} [28, 71, 94]. Although the EO response speed and modulation depth of KNN ceramics still need improvement, multi-element co-doping (e.g., Bi, Li, Sr, Ba) shows promise for producing a more uniform distribution of internal polar regions and enhancing EO performance. Overall, KNN transparent EO ceramics represent a promising pathway toward environmentally friendly materials and a key direction for future development.

Although KNN-based transparent ceramics have made notable structural and processing progress in recent years, systematic investigations of their EO properties remain limited. Representative advances are summarized in Table 2. Early work by Kroupa *et al.* [160] produced $80K_{0.5}Na_{0.5}NbO_3$–$20SrTiO_3$ (KNN–ST) transparent ceramics, revealing a characteristic quadratic EO response (Fig. 17(a)). Because reliable refractive-index data were unavailable at that time, the calculated EO coefficients carried considerable uncertainty. Li and co-workers [71, 95] later reported refractive-index parameters for KNN, recalculating the EO coefficient as approximately 1.65×10^{-17} m^2 V^{-2}. However, the EO response remains relatively slow, on the order of several hundred microseconds, which limits its potential for high-speed EO modulators.

With advances in processing, researchers used hot-press sintering to improve densification. Li *et al.* [94] fabricated dense $K_{0.48}Na_{0.52}Nb_{0.925}Bi_{0.075}O_3$ (KNNB) ceramics at 1060 °C for 5 h under 5.5 MPa, achieving 60% transmittance at 633 nm, a refractive index of 2.257, and a linear EO coefficient of 42 pm V^{-1} (Fig. 17(b)). Kwok *et al.* [70] introduced 2 mol% excess Bi_2O_3 into $(K_{0.5}Na_{0.5})_{0.95}Li_{0.05}Nb_{0.95}Bi_{0.05}O_3$ and, via hot-press sintering, obtained an EO coefficient of about 102 pm V^{-1}, demonstrating the dual role of Bi doping in improving transparency and enhancing EO activity. Based on this work, Li *et al.* [71] reported Li–Bi co-doped $(K_{0.5}Na_{0.5})_{1-x}Li_xNb_{1-x}Bi_xO_3$

（KNLNB-HP) ceramics with 58% transmittance at 900 nm and an EO coefficient up to 198 pm/V. The superior performance was attributed to the dense microstructure produced by hot pressing and the formation of abundant polar nanoregions induced by Bi incorporation, which enhanced refractive-index modulation under an external electric field.

In comparison, pressureless sintering usually yields lower densification, but appropriate design can still balance transparency and EO performance. Li *et al.* [95] prepared $(K_{0.5}Na_{0.5})_{0.9}Li_{0.1}Nb_{0.9}Bi_{0.1}O_3$ (KNLNB-NP) transparent ceramics using conventional pressureless sintering. Although the EO coefficient was about 40 pm V^{-1}, the transmittance reached 60% at 900 nm by adding 4 mol% excess Bi_2O_3 to induce a more cubic-like structure and form polar nanoregions. Furthermore, Wu *et al.* [116] fabricated $(K_{0.5}Na_{0.5})_{0.94}Li_{0.06}Nb_{0.94}Bi_{0.06}O_3$ doped with 1 mol% Er^{3+} (KNLNB-Er), achieving an EO coefficient of 128 pm V^{-1} and pronounced photoluminescence. These results indicate that pressureless sintering combined with rare-earth doping preserves transparency while enabling multifunctional responses, highlighting potential for optoelectronic integration.

Structural regulation can enhance the EO response of KNN-based transparent ceramics through different mechanisms depending on the specific phase evolution. In $(K_{0.5}Na_{0.5})_{0.9}Sr_{0.1}Nb_{0.9}Ti_{0.1}O_3$-$x$%$Bi_2O_3$ (KNSNT-Bi) ceramics, Liu *et al.* [161] showed that increasing Bi_2O_3 content induced a transition from the T phase toward a pseudocubic (P) relaxor phase. This higher-symmetry P phase reduces optical anisotropy and birefringence-related scattering, while the formation of fingerprint-like nanodomains smaller than 50 nm improves electric-field sensitivity, yielding a maximum linear EO coefficient of ~26.1 pm V^{-1} (Fig. 17(c)). In contrast, Lin *et al.* [28] reported that $0.99(K_{0.5}Na_{0.5})NbO_3$–$0.01Bi(Ni_{2/3}Nb_{1/3})O_3$ (KNN–BNN) ceramics transformed from an O phase to O–T coexistence after Ta^{5+} introduction, with grains refined to 200–290 nm. With 6 mol% Ta doping, a complex multiscale domain architecture formed, which facilitated polarization rotation and domain switching, enhanced the inverse piezoelectric contribution and electric-field-responsive electronic susceptibility, and thereby yielded an EO coefficient of ~84 pm V^{-1} (Fig. 17(d)).

Overall, although KNN-based transparent EO ceramics still fall short of PMN–PT in performance, their environmental advantages and tunability make them a key direction for future development. Current studies indicate that HPS is crucial for achieving high densification and transmittance; Bi/Li co-doping effectively induces polar nanoregions and markedly enhances the EO response; and elements such as Sr, Ti, and Ta further optimize reversible polarization through phase-structure regulation and domain engineering. Following the sequence of process optimization → composition control → microstructure evolution → performance improvement, KNN is gradually becoming the main representative of lead-free transparent EO ceramics.

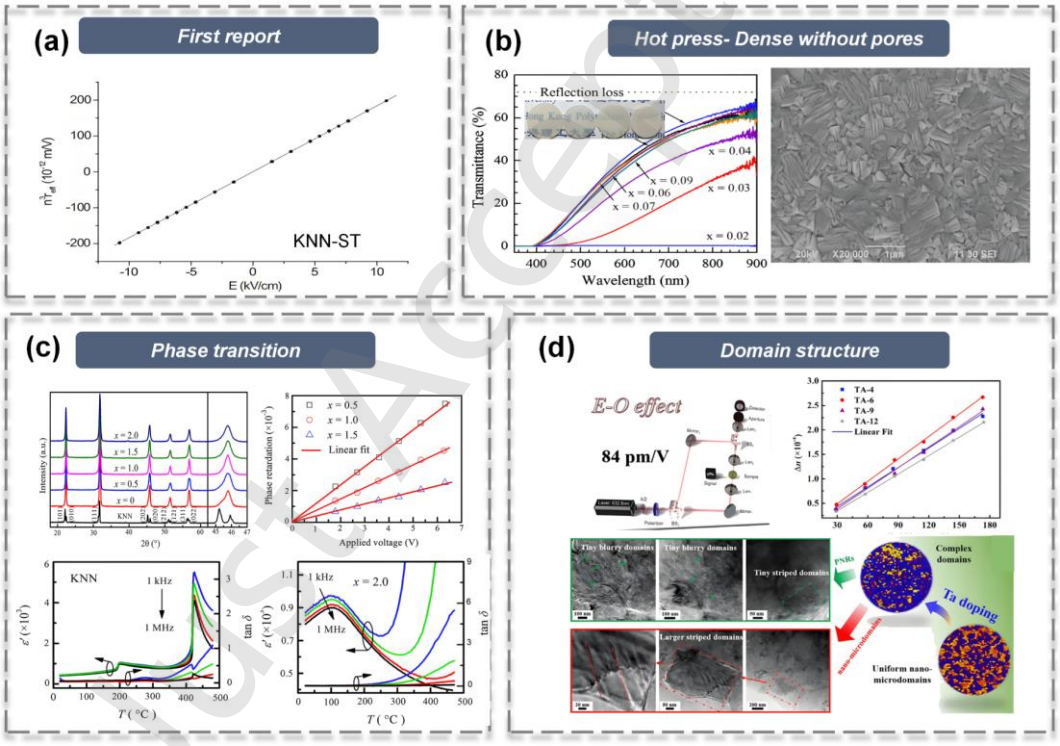

Fig. 17. Research progress on the electro-optic properties of KNN-based transparent ceramics. (a) Electro-optic performance of KNN-ST ceramics. Reproduced with permission from Ref. [160], © IOP Publishing Ltd 2005. (b) Transmittance and microstructure of hot-pressed KNN ceramics. Reproduced with permission from Ref. [71], © Elsevier BV 2013. (c) Influence of phase transition on electro-optic performance. Reproduced with permission from Ref. [161], © Springer US 2015. (d) Domain structure evolution and enhancement of electro-optic properties. Reproduced with permission from Ref. [28], © Elsevier Ltd 2022.

3.2.4. Summary

Transparent electro-optic ceramics have made notable progress over the past two decades, but lead-based and lead-free systems show distinct development levels and application orientations. PMN–PT-based transparent materials are currently a technologically advanced platform for electro-optic devices, benefiting from large electro-optic coefficients, fast response, relatively low driving voltage, and demonstrated functional prototypes such as electro-optic switches, Q-switches, tunable filters, polarization controllers, and optical-communication components. Therefore, they are more suitable for near-term high-speed and high-sensitivity photonic devices where performance is the primary requirement. However, their lead-containing composition, processing sensitivity, and thermal or field stability issues may limit broader deployment under environmentally regulated or harsh operating conditions. In contrast, KNN-based transparent electro-optic ceramics validate the feasibility of lead-free electro-optic materials and offer advantages in environmental compatibility, compositional flexibility, and multifunctional integration with luminescence or photochromism. At present, however, their electro-optic coefficients, response speed, and device-level demonstrations still lag behind those of PMN–PT-based systems. Overall, PMN–PT systems are better suited for near-term high-performance electro-optic devices, whereas KNN systems represent a longer-term green platform for integrated and multifunctional transparent photonics.

3.3. Transparent Energy-Storage Ceramics

3.3.1. Energy-Storage Mechanisms and Application Scenarios

The fundamental mechanism of dielectric energy storage arises from polarization and depolarization under an external electric field. The core principle is the polarization behavior of the dielectric under an applied electric field. As illustrated in Fig. 18, the polarization–electric field (P–E) hysteresis loop directly represents the energy-storage behavior. A large saturation polarization (P_s) combined with a small remanent polarization (P_r) enables higher recoverable polarization and lower energy loss. Moreover, a higher breakdown electric field (E_b) permits stronger applied fields and leads to a higher recoverable energy-storage density (W_{rec}).

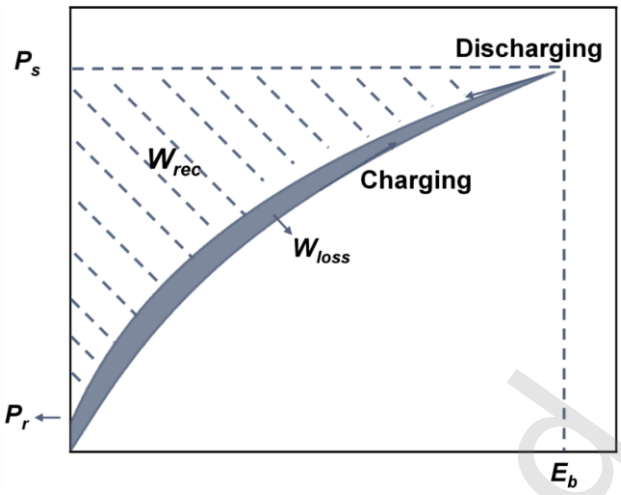

Fig. 18. Schematic of a *P*–*E* hysteresis loop.

With the rapid development of new energy technologies and portable electronics, demand is rising for energy-storage materials that combine high energy density with low loss. Transparent energy-storage ceramics are a new class of dielectrics with high permittivity, large energy-storage density, and excellent optical transparency, showing strong potential for transparent displays and transparent supercapacitors [38-40]. Synergistic optimization requires systematic design, including grain-size control, microstructural tuning, and enhancement of breakdown strength.

Common transparent energy-storage materials include KNN-based ceramics or films, HfO_2 thin films, and PLZT-based films. Among these, KNN-based TFCs have attracted considerable attention because they are environmentally friendly and exhibit an excellent dielectric response. For example, $0.94(K_{0.5}Na_{0.5})NbO_3$–$0.06Sr_{0.7}La_{0.2}ZrO_3$ (KNN–SLZ) transparent ceramics show 62% transmittance at 780 nm, a recoverable energy density W_{rec} = 2.7 J cm^{-3}, charging/discharging capability with power density up to 243 MW cm^{-3}, and a discharge response time of ≈ 76 ns [162]. Qu *et al.* [163] first prepared $0.8(K_{0.5}Na_{0.5})NbO_3$–$0.2Sr(Sc_{0.5}Nb_{0.5})O_3$ (KNN–SSN), achieving W_{rec} = 2.0 J cm^{-3} and 55% transmittance at 780 nm. Later, Chai *et al.* [164] introduced $Sr(Zn_{1/3}Nb_{2/3})O_3$ into KNN, increasing transmittance to 73% at 780 nm and achieving W_{rec} = 1.5 J cm^{-3} under a moderate field. These results highlight the strong potential of KNN-based transparent ceramics for next-generation transparent pulsed capacitors operating at high power and high frequency. By contrast, although

PMN–PT shows outstanding performance in transparent piezoelectric and electro-optic applications, its relatively low breakdown strength and high dielectric loss have thus far precluded reports of PMN–PT-based transparent energy-storage ceramics.

3.3.2. Progress and Optimization Strategies in KNN

In recent years, KNN-based transparent energy-storage ceramics have attracted extensive attention, and research on them has made significant progress. The specific developments are summarized in Table 3.

Table 3. Research progress of KNN transparent energy storage ceramics

Component	Transmittance [%]	Wavelength [nm]	t [mm]	G [nm]	W_{rec} [J cm^{-3}]	η [%]	E_b [kV cm^{-1}]	Refs.
KNN-SSN	66	900	0.3	500	2.02	81.4	295	[163]
KNN-SZN	73	780	0.5	136	1.5	50	180	[164]
KNN-EB	50	800	0.1	120	1.85	69	280	[165]
KNN-KBN	83	1600	0.2	100	3.39	51	330	[166]
KNN-SZ	68	2000	0.3	200	2.81	80	370	[167]
KNN-LB	77	750	0.3	145	3.6	74.2	340	[168]
KNN-SSN	76.7	780	0.3	210	2.65	60	395	[40]
KNN-BLN	78	1200	0.3	109	4.39	81.4	345	[169]
KNN-BST-Er	72	900	0.3	98	3.42	53.5	320	[170]
KNN-BZZ	67	800	0.2	261	2.56	69	315	[171]
KNN-BZN	70	780	0.1	80	7.4	74	750	[6]
KNN-SLZ	62	780	0.3	270	5.6	71	540	[162]
KNN-SLT	60	780	0.3	210	4.04	73	210	[172]
KNN-BCZT	50	850	--	700	7.83	81	604	[173]
KNNT-NL-Sr	43	900	0.25	60	5.9	84.2	490	[174]
KNN-BL	44.8	1100	--	330	1.75	83.5	220	[175]
KNNT-BZT-Er	72	880	0.25	73	6.2	71.3	670	[176]
KNN-SSN-Er	48	780	0.3	280	2.03	75.7	240	[177]
KNN-BCZT-BMT	--	--	--	1220	7.62	86	550	[178]
KNLN-SZ	55	780	0.3	380	4.06	75	400	[179]

t, W_{rec}, η, G, and E_b correspond to the following: sample thickness, recoverable energy density, energy storage efficiency, grain size, and breakdown electric field, respectively.

In studies of KNN-based transparent energy-storage ceramics, controlling grain size, domain structure, and band gap has consistently guided performance optimization. Although these three factors are intrinsically distinct, they are strongly coupled and jointly determine the transmittance and energy-storage capacity of the material (Fig. 19).

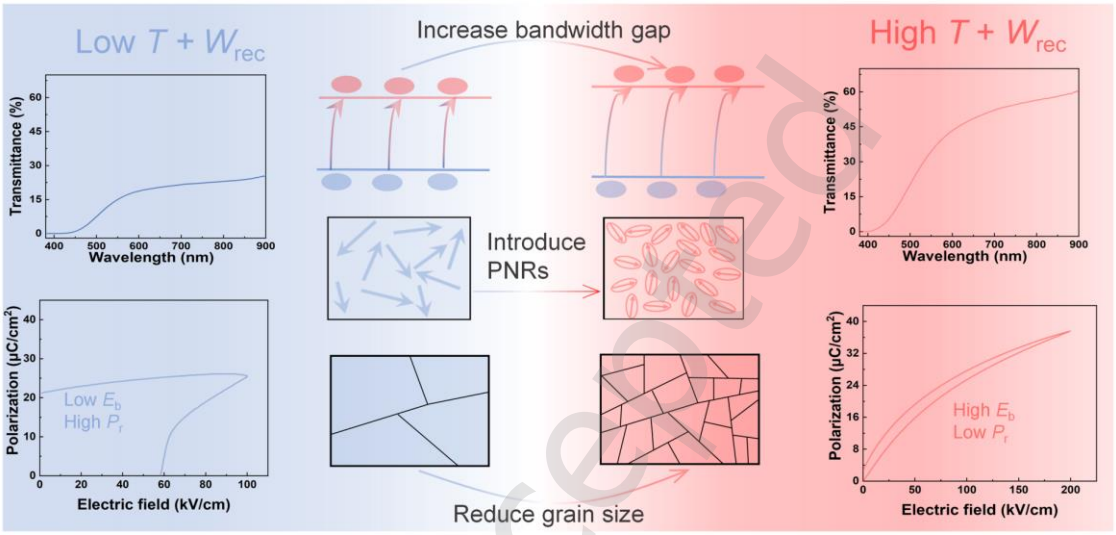

Fig. 19. Regulation strategies for transparent energy-storage KNN ceramics.

The influence of grain size on material properties is both direct and pronounced. Larger grains generally cause stronger light scattering at grain boundaries, thereby reducing transmittance. In addition, macroscopic polarization switching becomes more hysteretic, increasing remanent polarization and reducing recoverable energy density and efficiency, both of which are unfavorable for energy storage. Ren *et al.* [167] introduced $SrZrO_3$ (SZ) into KNN to refine the grain size to about 200 nm and adjusted the phase boundary toward a pseudocubic structure, achieving 68% transmittance, a recoverable energy density $W_{rec} \approx 2.81$ J cm^{-3}, and 80% efficiency. Similar trends were observed by Xing *et al.* and Zhang *et al.* In the KNN–$LaBiO_3$ (KNN–LB) system studied by Xing and co-workers, a grain size of about 145 nm yielded 77% transmittance and $W_{rec} \approx 3.6$ J cm^{-3} [168]. In KNN–$(K_{0.7}Bi_{0.3})NbO_3$ (KNN–KBN) ceramics, the grain size was refined to about 100 nm, yielding 83% transmittance and a W of 3.39 J cm^{-3} with stable performance from 20°C to 120°C [166]. These results indicate that fine-grained microstructures improve optical transparency, enhance

local field uniformity, and suppress breakdown, thereby increasing the E_b. Consequently, the *P-E* hysteresis loop becomes slimmer, leading to higher energy efficiency. Further studies by Yang *et al.*, Song *et al.*, and Gong *et al.* [175, 177, 179] have repeatedly verified this trend, demonstrating that refined grains enable both high transmittance and enhanced energy-storage output.

Regarding band-structure regulation, it is generally accepted that the band gap (E_g) directly determines both the optical and electrical properties of KNN-based transparent energy-storage ceramics. A narrower E_g causes stronger absorption from the visible to the near-infrared range, reduces transmittance, increases leakage current, and lowers E_b, thereby limiting energy-storage performance. In contrast, widening the band gap effectively suppresses optical absorption, enhances transparency, reduces energy loss, and significantly increases both E_b and η. Chai *et al.* [164] introduced $Sr(Zn_{1/3}Nb_{2/3})O_3$ (SZN) into KNN, widening E_g to 3.13 eV, achieving 73% transmittance at 780 nm and an energy-storage density of about 1.5 J cm^{-3}, clearly revealing the correlation between band-gap widening and performance improvement. In the Er-doped KNN–$(Ba,Sr)TiO_3$ system (KNN–BST-Er) system reported by Lin *et al.* [170] adjusting the Sr/Ba ratio increased E_g from 3.03 eV to 3.10 eV, resulting in a recoverable energy density of 3.42 J cm^{-3} and a 42 ns discharge under 72% transmittance, highlighting the synergy among band-gap expansion, symmetry enhancement, and relaxor behavior. Dai *et al.* [40] showed that SSN doping widened E_g to 3.21 eV, accompanied by grain refinement and nanoscale domain formation, yielding 84.5% transmittance in the near-infrared and stable efficiency of 76–83%. KNN–$BiZn_{0.5}Zr_{0.5}O_3$ (KNN–BZZ) ceramics achieved E_g of 3.16 eV through the introduction of BZZ, reaching 73% transmittance, a breakdown field of about 315 kV cm^{-1}, and efficiency above 90%, with significantly reduced energy loss [171]. Overall, these studies confirm that widening the band gap serves as an intrinsic modulation pathway. Rather than directly affecting scattering or domain switching, it indirectly governs the upper limits of transmittance and breakdown strength by mitigating optical absorption and leakage. When E_g increases from about 2.8 eV to 3.1–3.2 eV, KNN-based transparent energy-storage ceramics typically

achieve 70–85% transmittance, E_b exceeding 300 kV cm^{-1}, η of 80–93% and W_{rec} around 2–3 J cm^{-3}, demonstrating the crucial role of band-gap engineering in performance optimization.

In KNN-based transparent energy-storage ceramics, domain-structure refinement is a key approach to achieving both high transparency and excellent energy-storage performance. The formation of nanoscale ferroelectric domains and PNRs plays a critical role. Macroscopic ferroelectric domains often introduce strong refractive-index anisotropy and domain-wall scattering, reducing optical uniformity and limiting transmittance. Moreover, large domains show pronounced hysteresis during polarization switching under external fields, leading to square *P*–*E* loops and large P_r. When the domain size is reduced to the nanoscale, local polarization becomes short-range ordered. A homogeneous distribution of PNRs produces near-optical isotropy, effectively suppressing scattering and improving transmittance. Meanwhile, polarization switching becomes more reversible, yielding slimmer *P*–*E* loops, smaller P_r, and significantly enhanced energy efficiency. Numerous experimental studies have verified this mechanism. Chai *et al.* [172] reported that $Sr_{0.7}La_{0.2}TiO_3$ (SLT) doping generated abundant PNRs, reduced domain size and scattering, and enabled slender *P*–*E* loops with energy density above 4 J cm^{-3} while maintaining high transmittance. In the KNN–SLZ, Chai *et al.* [162] further achieved uniform nanoscale domain distribution through compositional tuning, where enhanced relaxor behavior suppressed domain-wall pinning, resulting in >70% transmittance and improved E_b and η. Yang *et al.* [179] provided direct PFM and TEM evidence that increasing SZ doping disrupted long-range ordered domains into nanoscale domains, lowering switching voltage, reducing loss, and enabling stable high-efficiency energy storage while maintaining transparency. Similarly, Hou *et al.* [171] showed that $BiZn_{0.5}Zr_{0.5}O_3$ (BZZ) doping produced nanoscale domains and PNRs through slight lattice distortion, yielding η > 90% at 73% transmittance. In high-performance composite systems, Sun *et al.* [178] observed 180° nanoscale stripe domains via TEM and found reduced polarization retention by first-order reversal curves analysis, consistent with loop linearization and enhanced energy efficiency, achieving an energy

density near 8 J cm^{-3}. Bi *et al.* [176] further showed that Er doping promoted nanoscale domains and local polarization inhomogeneity, enhancing relaxor behavior and achieving energy density above 6 J cm^{-3} while maintaining 72% transmittance.

3.3.3. Summary

Transparent energy-storage ceramics combine optical clarity with high-density electrical energy storage, making them ideal for next-generation smart windows, transparent electronics, and integrated optoelectronics. KNN-based systems have become the leading platform, achieving strong performance (6–8 J cm^{-3} storage density with 70–85% transparency) by co-optimizing grain size, band gap, and domain structure. In contrast, PMN–PT materials are less suitable due to their lower breakdown strength and higher dielectric loss. Future progress hinges on improving temperature stability, cycling endurance, and scalable fabrication to move these promising materials from lab demonstrations into real-world devices.

3.4. Transparent Luminescent Ceramics

3.4.1. Photoluminescence Mechanisms and Application Prospects

Transparent ferroelectric materials doped with luminescent ions combine high optical transparency with strong photoluminescence, attracting broad attention. As shown in Fig. 20, luminescence primarily arises from electronic transitions of activator ions in excited states: electrons relax from higher to lower energy levels and release photons, producing light emissions.

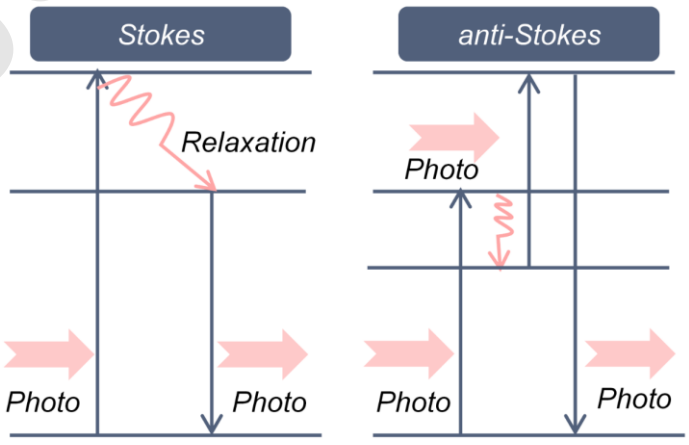

Fig. 20. Schematic illustration of the photoluminescence mechanism.

Under an external electric field, the polarization state of ferroelectric materials can be reversibly switched. This electric field does not directly excite luminescence but instead modulates the optically excited emission by altering polarization states, local crystal fields, or defect distributions, thereby enabling electric-field-modulated photoluminescence. Typical transparent ferroelectric luminescent materials include KNN, PMN–PT, and PLZT ceramics or single crystals, as well as BNT-based thin films. Owing to their combination of optical excitation and ferroelectric tunability, these materials show strong potential for lighting, displays, optoelectronic devices, smart glass, decorative design, optical sensing, and biomedicine [34, 180-183]. For example, Eu-doped $0.94Bi_{0.5}Na_{0.5}TiO_3$–$0.06BaTiO_3$ transparent films exhibit intense optically excited luminescence, together with excellent flexibility and bending resistance, indicating strong potential for electric-field-modulated photoluminescent wearable memories, sensors, and flexible displays [184].

The luminescence of transparent ceramics primarily arises from energy-level transitions of rare-earth ions such as Eu^{3+}, Er^{3+}, and Pr^{3+}. Their emission intensity can be tuned by an external electric field. These ceramics are promising for flat-panel displays, solid-state lighting, and optical or temperature sensing. To balance luminescence and transparency, materials should possess high lattice symmetry to minimize scattering losses. The rare-earth dopant concentration should be carefully controlled to ensure a uniform distribution of luminescent centers and, in turn, efficient and stable emission.

Rare-earth dopants in luminescent TFCs should not be regarded only as optical activators. Their 4f energy levels determine emission color, lifetime, upconversion/downconversion pathways, and temperature-dependent fluorescence response. Meanwhile, their ionic radius, valence state, and site occupancy introduce local lattice distortion, random fields, and charge-compensation defects, which can modify PNR formation, domain-wall energy, and polarization switching. Under an external electric field, ferroelectric polarization changes the local crystal-field symmetry around rare-earth ions and may redistribute nearby defect states, leading to reversible luminescence modulation.

Therefore, rare-earth doping establishes a coupled "luminescent center–local crystal field–ferroelectric polarization" mechanism. Excessive doping, however, may cause concentration quenching, defect-related absorption, structural disorder, and reduced transmittance, indicating that emission efficiency, transparency, and ferroelectric switchability must be optimized together.

3.4.2. Progress and Optimization Strategies in PMN–PT

In the PMN–PT system, doping with rare-earth ions such as Er and Pr enables both upconversion and downconversion luminescence while maintaining high optical transmittance (≈ 60%). Using an optimized two-step sintering process, rare-earth-doped PMN–PT ceramics exhibit multiple distinct emission peaks under near-infrared excitation. Their emission intensity and spectral distribution are highly sensitive to temperature and electric field, indicating strong optoelectronic responsiveness. Studies have shown that adjusting dopant concentration and microstructural features can enhance fluorescence efficiency and enable color-tunable emission, providing a theoretical and technological foundation for their application in smart light-control components and multifunctional optoelectronic devices.

Qin *et al*. [185] fabricated Pr-doped 75PMN–25PT ceramics with 68% transmittance at 900 nm. Under 450 nm excitation, the ceramics exhibited strong red emissions at 619 nm and 650 nm. Within -50 to 40°C, the fluorescence intensity ratio exhibited a highly linear dependence on temperature, demonstrating strong potential for temperature-sensing applications (Fig. 21(a)). Furthermore, Pr/Yb co-doped 75PMN–25PT transparent ceramics exhibited both strong upconversion and downconversion luminescence. As the Yb^{3+} content increased from 1 to 3 mol%, the blue–green emission intensity decreased significantly. Detailed studies revealed that Pr/Yb co-doped 75PMN–25PT exhibited strong photoluminescence in both near-infrared and visible regions with pronounced temperature dependence. The downconversion emission weakened with increasing temperature, whereas the upconversion emission intensified as the temperature rose from -133 to 47°C. This behavior results from enhanced lattice vibrations and relaxation at luminescent centers, which

increase the probability of nonradiative transitions and thereby reduce emission efficiency. Meanwhile, higher temperature facilitates the absorption of environmental energy by electrons participating in Pr^{3+} transitions, increasing the population of excited Pr^{3+} ions [183].

Wei *et al.* [103, 186] prepared Er-doped 75PMN–25PT transparent ceramics by a two-step sintering process, achieving 65% transmittance in the near-infrared region. Under 521 nm excitation, distinct emission peaks appeared at 950–1060 nm, 1220–1290 nm, and 1420–1560 nm. The emission intensity initially increased and then decreased with rising temperature, whereas the emission bandwidth increased monotonically. Zeng *et al.* [102] investigated the upconversion luminescence of Er^{3+}-doped 75MN–25PT transparent ceramics and found that the emission color shifted from yellow-green to red-orange with increasing Er^{3+} concentration. At low Er content, upconversion was dominated by excited-state absorption, whereas at higher concentrations it was primarily governed by cross-relaxation. Liang *et al.* [187] reported that the fluorescence intensity ratio (FIR) of Er-75PMN–25PT varied linearly with temperature between 303 and 463 K, enabling an FIR-based temperature sensor with 0.5 K resolution and 2.9% K^{-1} sensitivity. Building on this, Zeng *et al.* [102] observed stronger luminescence enhancement in Pr-doped 70PMN–30PT transparent ceramics. The near-infrared transmittance was approximately 69.7%, and under 448–450 nm excitation, the 650 nm red-emission peak intensity was about seven times higher than that of opaque samples. The study further indicated that the migration and coalescence of nanoscale domains under low and high electric fields were closely correlated with the observed luminescence enhancement (Fig. 21(b)).

Yao *et al.* [188] fabricated Er-doped (1–*x*)PMN–*x*PT transparent ceramics with varying compositions and found that PT content strongly affected crystal-structure symmetry, which in turn influenced the red-to-green emission intensity ratio I_r/I_g (Fig. 21(c)). They also observed that an external electric field modified the microstructure of the transparent ceramics, thereby influencing both transparency and luminescent performance. Zhou *et al.* [112] reported that with increasing Eu content, micrometer-scale ferroelectric domains in 75PMN–25PT transparent ceramics evolved into

sub-micrometer fingerprint-like domains, enhancing field-induced light scattering and reducing transmittance (Fig. 21(d)). Guo *et al.* and Liang *et al.* [141, 187] prepared Pr-doped 75PMN–25PT and Er-doped 75PMN–25PT transparent luminescent ceramics and found that applying an external electric field significantly increased emission intensity, attributed to polarization-induced local symmetry breaking and enhanced optical absorption (Fig. 21(e)).

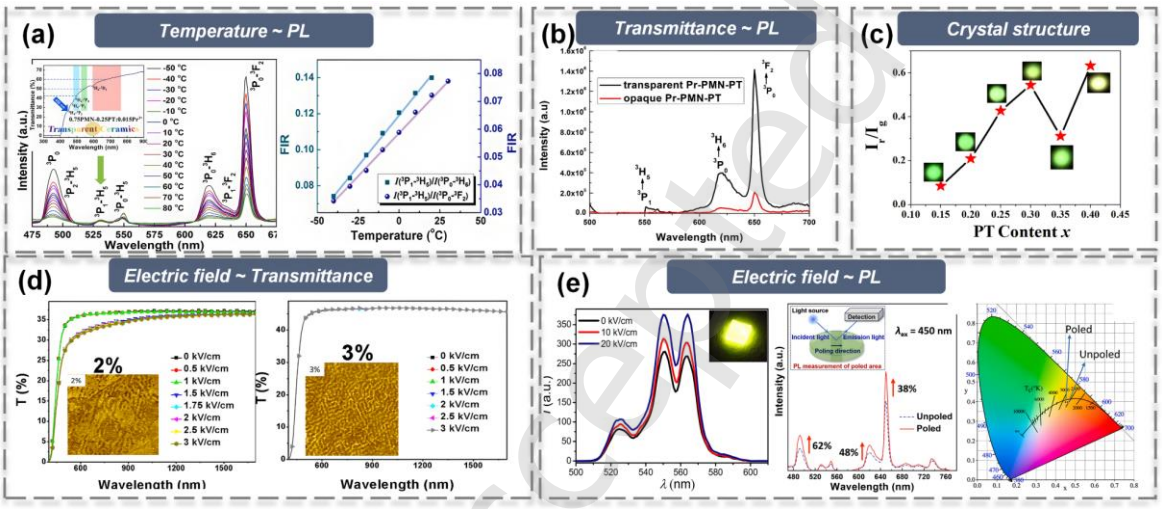

Fig. 21. Luminescent properties of PMN–PT-based transparent ceramics. (a) Red emission and temperature sensing of Pr-doped ceramics. Reproduced with permission from Ref. [185], © Elsevier Ltd 2021. (b) Influence of transparency on luminescence performance. Reproduced with permission from Ref. [65], © Elsevier BV 2024. (c) Effect of crystal structure on emission intensity. Reproduced with permission from Ref. [188], © American Institute of Physics 2015. (d) Electric-field-controlled transmittance. Reproduced with permission from Ref. [112], © Wiley-Blackwell 2016. (e) Effect of external electric field on luminescence intensity. Reproduced with permission from Ref. [141, 187], © American Institute of Physics 2016; Elsevier BV 2024.

3.4.3. Progress and Optimization Strategies in KNN

In the lead-free KNN system, doping with rare-earth ions imparts excellent photoluminescent properties to the material. While maintaining high optical transmittance (60–80%), KNN-based transparent ceramics exhibit both upconversion and downconversion multiband emissions with strong tunability under temperature and electric-field stimuli. This has led to a synergistic design paradigm described as a "transparent matrix–rare-earth emission center–local structure (PNRs/near-

pseudocubic)" framework. Er-doped KNN–CBN transparent ceramics achieve over 74% transmittance in the near-infrared region and display characteristic upconversion luminescence under 980 nm excitation. The green emissions are centered at approximately 530 and 550 nm, corresponding to the $^2H_{11/2}$ and $4S_{3/2}\rightarrow{}^4I_{15/2}$ transitions of Er^{3+}, while the red emission occurs near 660 nm ($^4F_{9/2}\rightarrow{}^4I_{15/2}$). This combination of high transparency and strong luminescence is attributed to the near-pseudocubic phase and fine-grained nanostructure of the ceramics [189]. Furthermore, Ta^{5+} co-doped KNN:Er ceramics exhibit temperature-sensitive luminescence. Based on the thermally coupled levels ($^2H_{11/2}$ and $^4S_{3/2}$) of Er^{3+}, an FIR-based thermometer was constructed, achieving enhanced sensitivity over 273–543 K. Notably, as the structure evolved from the orthorhombic to near-cubic phase, the near-infrared emission intensity showed an abrupt temperature response, revealing a pronounced amplification effect of phase boundaries on luminescent thermal behavior (Fig. 22(a)) [190]. Pr-doped KNN–CT transparent ceramics primarily exhibit red emission, where the fluorescence intensity ratio (FIR) based on the $^1D_2\rightarrow{}^3H_4$ and $^3P_0\rightarrow{}^3H_5$ transitions enables highly sensitive temperature detection (S_a = 0.139 K^{-1}, S_r = 2.69% K^{-1}), far exceeding conventional Pr^{3+}-doped systems (Fig. 22(b)). The authors [191] attributed this exceptional sensitivity to the cooperative effects of PNRs formation and local crystal-field modulation, which tightly couple luminescence with reversible polarization switching.

Eu-doped KNN transparent ceramics exhibit typical downconversion emission, with a dominant peak at approximately 614 nm ($^5D_0\rightarrow{}^7F_2$) and additional peaks at 591 and 650 nm. As the Eu^{3+} concentration increases, the red emission gradually intensifies and becomes dominant in the overall spectrum. Moderate Eu^{3+} substitution introduces local structural inhomogeneity accompanied by the formation of PNRs. This process weakens long-range ferroelectric order, promotes a near-pseudocubic phase, and enhances the tunability of emission intensity and lifetime, reflecting a coupled mechanism of "local crystal field–luminescent center–reversible polarization" (Fig. 22(c)) [192]. In addition, Tb-doped KNN transparent ceramics exhibit green emission (~546 nm, $^5D_4\rightarrow{}^7F_5$)

under 488 nm excitation, and the emission intensity increases under an external electric field. This enhancement is attributed to ferroelectric polarization–induced symmetry changes that alter the selection rules of 4f–4f transitions and increase radiative probability (Fig. 22(d)) [53, 193]. Dy-doped KNN ceramics display dual-channel emission with blue (~475 nm) and yellow (~573 nm) light, maintaining high transparency and enabling potential white-light applications [194]. Furthermore, Nd-doped KNN ceramics, although semitransparent, exhibit downconversion luminescence in the near-infrared region, with both emission intensity and lifetime showing reversible temperature-dependent modulation. This finding further confirms the universal coupling between rare-earth energy levels and local defects or crystal-field environments in this system [195].

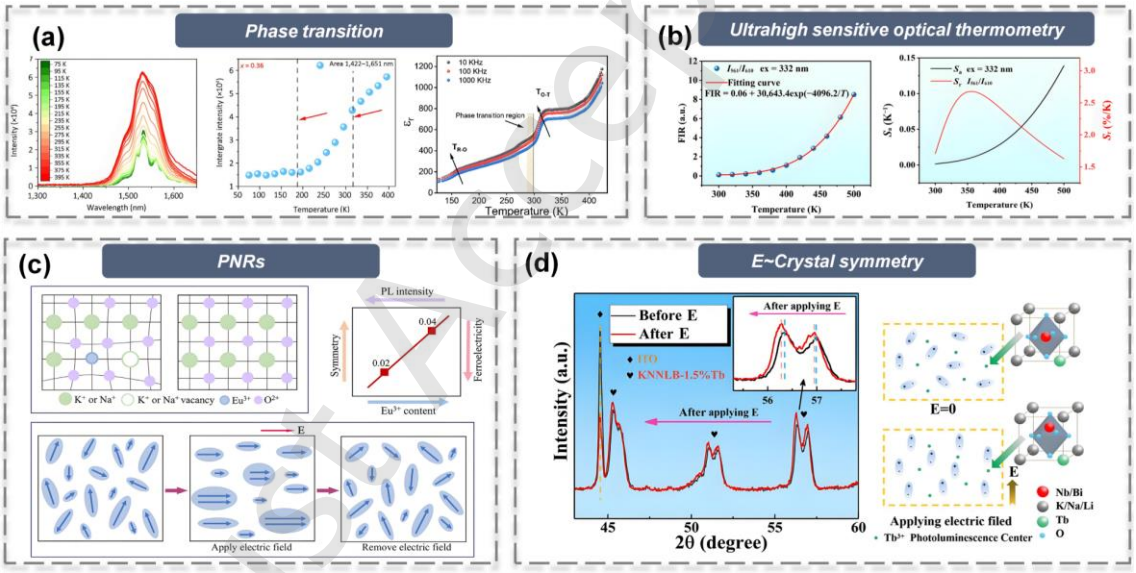

Fig. 22. Luminescence and modulation of rare-earth-doped KNN-based transparent ceramics. (a) Influence of phase transition on luminescent properties. Reproduced with permission from Ref. [190], © Chinese Ceramic Society 2024. (b) Highly sensitive FIR thermometry in Pr-doped KNN–CT ceramics. Reproduced with permission from Ref. [191], © Tsinghua University Press 2025. (c) Mechanism of PNRs induced enhancement in luminescence performance. Reproduced with permission from Ref. [192], © Wiley-Blackwell 2023. (d) Effect of external electric field on crystal-structure symmetry and luminescence. Reproduced with permission from Ref. [193], © American Chemical Society 2022.

3.4.4. Summary

Transparent luminescent ceramics integrate optical transparency, rare-earth photoluminescence, and ferroelectric tunability in a single platform. Two principal systems have emerged: PMN–PT, which offers mature field-tunable emission for optical thermometry and smart lighting; and lead-free KNN, which provides compositional flexibility for tailored emissions, ranging from sensitive thermometry based on Er/Pr to high-purity visible light based on Eu/Tb. Both exemplify a "transparent matrix–luminescent center–ferroelectric modulation" design, in which optical clarity, rare-earth emission, and polarization response must be balanced. Rare-earth ions act as emission centers, but they also modify local lattice distortion, charge compensation, PNRs formation, and domain switching. Therefore, luminescence modulation in TFCs is not an isolated optical process, but a coupled response involving local crystal-field symmetry, defect redistribution, and ferroelectric polarization. Future progress hinges on improving emission efficiency, cycling stability, and electric-field controllability to advance applications in sensing, lighting, and integrated photonics.

3.5. Transparent Photochromic Ceramics

3.5.1 Photochromic Mechanisms and Application Scenarios

Photogenerated color change (photochromism) is a reversible color variation triggered by irradiation at specific wavelengths. The color changes during illumination, persists after the light is removed, and recovers to the original state upon thermal stimulation or illumination at a suitable wavelength. The underlying mechanism is the formation of color centers caused by electronic-state transfer and ion migration (Fig. 23). For transparent photochromic ceramics, a pronounced and stable response requires high transmittance and precise tuning of defect energy levels by controlling oxygen vacancies, cation vacancies, and rare-earth doping. In recent years, TFCs doped with rare-earth luminescent ions have attracted considerable attention because they combine strong photochromism with ferroelectricity and high transparency. For example, rare-earth-doped KNN transparent ceramics enable information writing under laser irradiation and readout via photochromic modulation, demonstrating preliminary three-dimensional optical data storage [51, 109, 196]. These materials

show broad prospects for high-density optical storage, multilevel encryption, smart windows, optoelectronic devices, and privacy protection [197-201]. Notably, most studies on the PMN–PT system focus on electrical properties, and related work on photochromism has not yet been reported.

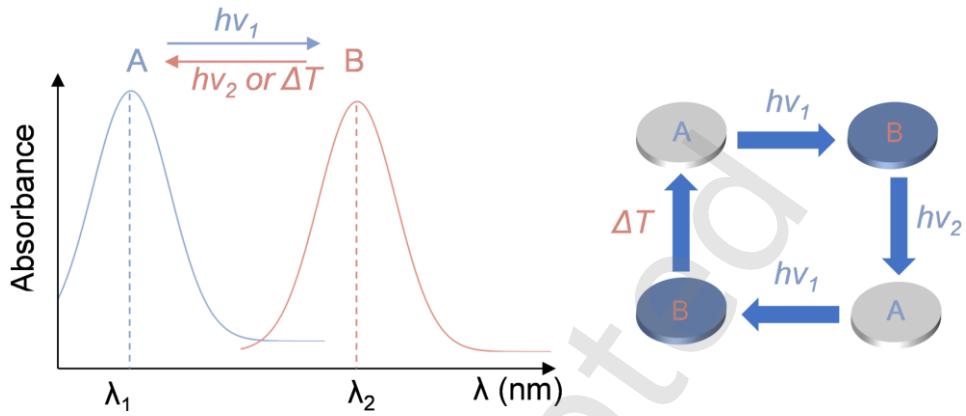

Fig. 23. Schematic illustration of the photochromic mechanism.

3.5.2 Progress and Optimization Strategies in KNN

In the KNN system, photochromic behavior primarily arises from defect regulation induced by alkali-element volatilization during high-temperature sintering and by rare-earth doping (Fig. 24) [52]. During sintering, volatilization of K^+/Na^+ generates cation vacancies, which are often accompanied by oxygen vacancies to maintain charge neutrality. When rare-earth ions occupy the A site, they further alter the local environment and energy-level distribution, creating electron and hole trap states. Under illumination at specific wavelengths, photogenerated electrons and holes are captured by these traps, forming F centers and V centers, respectively. This process causes partial absorption or scattering of incident light, thereby reducing transmittance and producing observable color changes. In addition, excited-state electrons at luminescent centers may be trapped, resulting in a temporary decrease in emission intensity. Upon heating or illumination at suitable wavelengths, trapped carriers are released, color centers disappear, and both transparency and luminescence recover to their initial states. Recent studies show that co-doping with rare-earth and alkali elements improves transparency, enhances the photochromic response, and shortens the response time to a few seconds, thereby improving practical feasibility. Defect regulation in transparent photochromic

ceramics involves an intrinsic trade-off between optical modulation and electrical reliability. Oxygen vacancies, cation vacancies, and rare-earth-related charge-compensation defects provide trap states for photogenerated carriers and enable the reversible formation of F/V color centers. A moderate distribution of shallow and deep traps is beneficial for fast coloration, large transmittance/luminescence modulation, and long retention. However, excessive oxygen vacancies or overly dense trap states can introduce additional absorption centers, hopping-conduction paths, and leakage-current channels, thereby increasing dielectric loss, reducing breakdown strength, and degrading cycling stability. Oxygen annealing reflects this trade-off: it can suppress oxygen-vacancy-related absorption and improve transparency and electrical stability, but may weaken photochromic contrast and luminescence modulation by reducing active traps. Thus, defect engineering should aim to construct an optimized trap landscape rather than simply increasing or eliminating defects. For example, Lin *et al.* [51] fabricated Sm-doped KNN transparent photochromic ceramics with ≈ 59% transmittance, achieving a transmittance modulation $\Delta R_T \approx 5.2\%$ and a luminescence reduction $\Delta R_L \approx 24\%$, thereby confirming the strong potential of this system for photochromic applications.

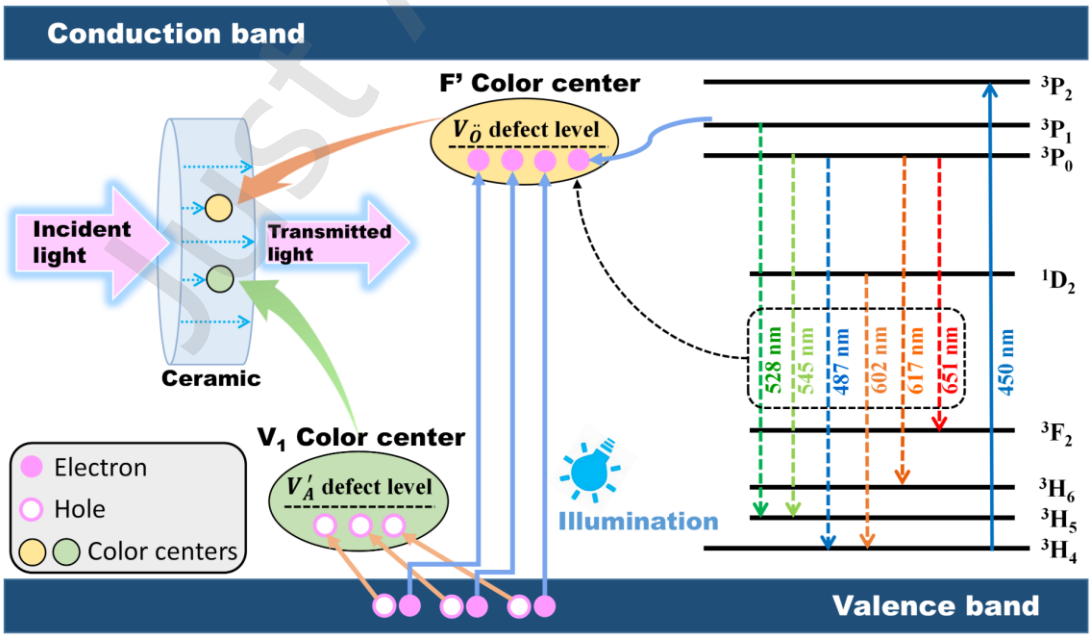

Fig. 24. Mechanism of photochromic modulation of transmittance and luminescence. Reproduced with permission from Ref. [52], © Royal Society of Chemistry 2023.

Rare-earth doping is a key strategy for optimizing the transparency, luminescence, and photochromic behavior of KNN-based transparent ceramics. Numerous studies have demonstrated that even single-ion doping can significantly improve the optical and electrical properties of these materials. Lin *et al.* [194] fabricated $95(K_{0.5}Na_{0.5})NbO_3–5Ba(Sc_{0.5}Nb_{0.5})O_3$ (KNN–BSN-Dy) transparent ceramics that maintained ~50% transmittance and exhibited high-quality white-light emission. This result indicates that the energy-level structure of Dy^{3+} matches well with the host band structure, imparting additional luminescent characteristics and yielding $\Delta R_T \approx 19.7\%$ and $\Delta R_L \approx 48\%$. Nd-doped KNN ceramics (KNN-Nd) exhibited a relatively low transmittance (~38%) but achieved $\Delta R \approx 36.4\%$ and $\Delta R_L \approx 67\%$, along with both upconversion and downconversion emissions that were particularly strong in the near-infrared region, demonstrating potential for optical communication and sensing (Fig. 25(a)) [195]. Jia *et al.* [53] reported Tb-doped KNN transparent ceramics with ~67% transmittance and an ultrahigh $\Delta R_L \approx 92.6\%$, the highest among similar materials to date. These ceramics retained optical information for up to six days without an external field, confirming the feasibility of KNN ceramics as optical storage media. Moreover, under alternating 407 nm irradiation for 20 s and thermal erasure at 150°C for 10 s, both transmittance and luminescence modulation remained reversible over 10 cycles without obvious degradation, suggesting good short-term cycling stability for repeated optical writing and erasing. Wang *et al.* [52] investigated Pr-doped KNN ceramics with ~64% transmittance at 900 nm. Thermoluminescence analysis (Fig. 25(b)) revealed that Pr doping introduced numerous deep defect levels. These deep traps were difficult to excite by visible light, thereby reducing ΔR_T, while the increased defect density enhanced competition with luminescent centers, leading to a larger ΔR_L. Zhou *et al.* [108] prepared highly transparent KNN-Eu ceramics exhibiting high-contrast, reversible photochromic and luminescent modulation under 380 nm UV writing and 250°C thermal erasing. XPS analysis verified the evolution of defect states, particularly those related to oxygen vacancies, before and after illumination, confirming the photochromic mechanism (Fig. 25(c)). These results indicate that

although single rare-earth doping entails trade-offs between transmittance and modulation depth, it plays a crucial role in establishing the fundamental performance framework of KNN-based transparent photochromic ceramics.

Building on the optimization of transparency and photochromic performance achieved through single rare-earth-ion doping, researchers have increasingly adopted co-doping strategies that combine rare-earth and alkaline-earth ions. This approach aims to simultaneously enhance photochromic contrast and accelerate response speed through dual modulation of defect chemistry and local structural reconstruction. The core mechanism lies in the complementary roles of dopants. Alkaline-earth ions such as Ba^{2+} or Sr^{2+} induce oxygen vacancies and local strain fields, reconstructing the defect-level distribution, while rare-earth ions, through their 4f electronic states and charge-compensation effects, interact with these defects to form a hierarchical trap system ranging from shallow to deep levels (Fig. 25(d)) [111]. Shallow traps capture photoexcited carriers rapidly under illumination, enabling subsecond-scale coloration, while deep traps sustain large $\Delta R_T/\Delta R_L$ modulation amplitudes and long-term retention, achieving a balance between transparency, modulation depth, and dynamic response. Specifically, Dy–Sr co-doped ceramics maintain high transmittance and exhibit strong photochromic modulation with intense white-light emission, whose brightness can be tuned before and after illumination, showing great promise for white LEDs and tunable optoelectronic devices [202]. Er–Ba/Sr co-doped systems also achieve high transparency together with enhanced $\Delta R_T/\Delta R_L$ performance [203]. Sr–Ho co-doped ceramics exhibit transmittance above 60% at 780 nm, $\Delta R_L > 90\%$, and reversible luminescence upon cycling, indicating that alkaline-earth incorporation not only tunes trap states but also stabilizes the energy-level environment of luminescent centers [204]. Regarding response speed, Pr/Sr co-doped ceramics achieve rapid coloration (~3 s) under 405 nm excitation with $\Delta R_L \approx 91\%$, exhibiting wavelength and time-programmable kinetics [50]. Ba/Sm co-doped samples complete significant color changes within 2 s, much faster than their single-doped counterparts [205]. Notably, the Ba/Pr co-doped

system, as verified by both DFT calculations and experiments, showed that a high concentration of oxygen vacancies induces deep-trap clusters, enabling ultrafast coloration within 0.1 s (Fig. 25(e)) while maintaining $\Delta R_T \approx 46\%$ and $\Delta R_L \approx 82\%$, thus supporting real-time optical recording and long-term data retention [111]. Overall, co-doping with rare-earth and alkaline-earth ions builds a graded "shallow–intermediate–deep" trap architecture that integrates high transparency, large modulation amplitude, and ultrafast response. This strategy also enhances emission reversibility and information-storage lifetime, providing a stable and efficient pathway for performance improvement in KNN-based transparent photochromic ceramics and laying a solid materials foundation for optical storage, anti-counterfeiting, and intelligent optoelectronic applications.

In addition, co-doping with multiple rare-earth ions offers a new route to simultaneously enhance photochromic and luminescent performance. Tb/Eu co-doped KNN ceramics exhibit high transparency along with multicolor and multimode emissions (Fig. 25(f)), greatly expanding information-storage capacity and flexibility. Their photochromic cycling stability is also significantly enhanced compared with that of single-doped materials [206]. The Yb/Eu co-doped system employs the sensitization effect of Yb^{3+} to enhance Eu^{3+} emission intensity and optimize the defect-state distribution, thereby improving the luminescence modulation ratio and photochromic contrast without compromising transparency, confirming the effectiveness of energy-level matching. Lin *et al.* [72] fabricated Er-doped $(K_{0.5}Na_{0.5})_{0.985}La_{0.015}NbO_3$ (KNLN–Er) ceramics with ~70% transmittance and modulation parameters of $\Delta R_L \approx 70\%$ and $\Delta R_T \approx 15\%$. Notably, the electrical properties of this material were also modulated during the photo-thermochromic process. Under 395 nm UV illumination (150 mW cm^{-2}), the room-temperature alternating-current impedance, measured with a 0.01 V signal over 10^{-2}–10^6 Hz, decreased markedly after coloration and could be restored by thermal bleaching at 200°C for 10 min (Fig. 25(g)). This reversible optical-electrical modulation indicates that rare-earth doping can couple photochromic and electrical functionalities, providing a basis for multifunctional smart-window devices. Chen *et al.* [207] introduced Ho^{3+}/Yb^{3+}, Er^{3+}/Yb^{3+},

and Tm^{3+}/Yb^{3+} co-doping into KNN ceramics, producing transparent samples with 35–40% transmittance at 750 nm and exhibiting dual photochromic–photoluminescent behavior. Among them, the Tm/Yb co-doped sample exhibited a unique negative thermal-quenching effect, where the upconversion emission intensified with increasing temperature, reaching a maximum fluorescence-intensity-ratio sensitivity of 2.54% K^{-1} at 213 K. It also showed self-recoverable photochromism without external fields and stable cycling performance. Similarly, Ho/Yb and Er/Yb co-doped systems exhibited reversible photochromism and temperature-dependent luminescence, providing experimental evidence for the multifunctional integration of "photochromism–luminescence–temperature sensing". Huang *et al.* [123] reported $Ba^{2+}/Ho^{3+}/Yb^{3+}$ co-doped KNN ceramics with 52% transmittance at 800 nm. This system showed strong green and red upconversion emissions under 980 nm excitation, with stable photochromic modulation ratios ($\Delta R_T \approx 34.1\%$, $\Delta R_L \approx 37.2\%$). Post-annealing treatment further allowed precise control of oxygen-vacancy concentration, achieving a balance between optical and electrical properties (Fig. 25(h)). Overall, multi–rare-earth co-doping enhances luminescence and photochromic coupling through energy-level complementarity and trap-state optimization, while improving cycling stability and multifunctional integration. This strategy opens new avenues for extending the applications of KNN-based transparent ceramics to optical information storage, sensing, and anti-counterfeiting technologies.

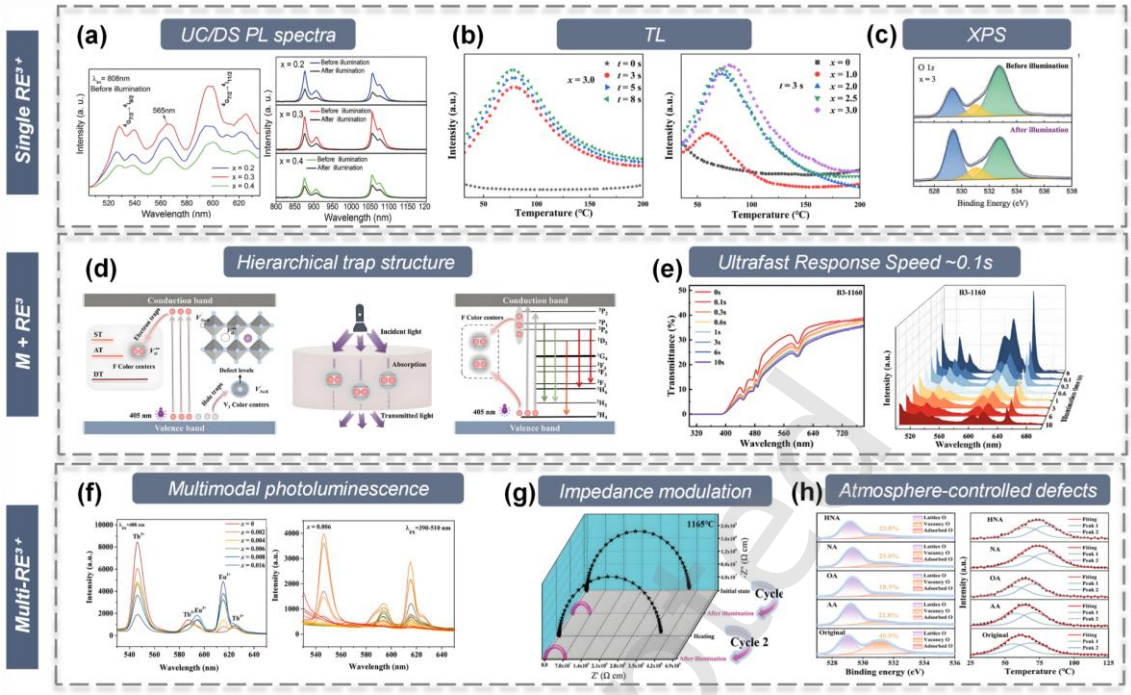

Fig. 25. Rare-earth and co-doping effects in KNN-based transparent photochromic ceramics. (a) Luminescent properties of Nd–KNN ceramics. Reproduced with permission from Ref. [195], © Royal Society of Chemistry 2020. (b) Correlation between thermoluminescence and defect energy levels in Pr–KNN ceramics. Reproduced with permission from Ref. [52], © Royal Society of Chemistry 2023. (c) XPS characterization of oxygen-vacancy evolution before and after irradiation. Reproduced with permission from Ref. [108], © Royal Society of Chemistry 2021. (d) Multilevel trap-well structure. Reproduced with permission from Ref. [50], © Elsevier 2022. (e) Ultrafast photochromism in Ba/Pr–KNN ceramics. Reproduced with permission from Ref. [111], © American Chemical Society 2023. (f) Multicolor emission in Tb/Eu co-doped ceramics. Reproduced with permission from Ref. [206], © Elsevier BV 2021. (g) Photochromism-modulated impedance behavior. Reproduced with permission from Ref. [72], © John Wiley and Sons Inc 2021. (h) Vacancy evolution regulated by annealing treatment. Reproduced with permission from Ref. [123], © Elsevier BV 2023.

3.5.3 Summary

KNN-based transparent ceramics have emerged as the primary platform for photochromic functionality, where light-induced coloration stems from reversible charge trapping at defect centers, including F and V centers. Systematic doping strategies have driven rapid progress: single rare-earth ions tune defect states for strong transmittance and luminescence modulation; co-doping with

alkaline-earth ions creates hierarchical shallow–intermediate–deep trap structures for fast response and long retention; and multi–rare-earth co-doping expands emission modes and information-storage capacity. These advances make KNN-based transparent photochromic ceramics promising for optical storage, anti-counterfeiting, smart windows, and sensing. From the perspective of multifunctional coupling, defect regulation is both the origin of photochromism and a potential reliability risk. Oxygen vacancies, cation vacancies, and rare-earth-related defects provide active traps for color-center formation, but excessive defects may increase optical absorption, leakage current, dielectric loss, and fatigue degradation. Therefore, practical photochromic TFCs should be evaluated not only by initial modulation depth, but also by erasing reversibility, leakage suppression, cycling stability, and long-term retention during repeated light-writing and thermal-erasing cycles.

4. Applications

TFCs couple high optical transmittance with ferroelectric, piezoelectric, electro-optic, energy-storage, luminescent, and photochromic functions. The transition from high-performance materials to functional devices further validates the promise of TFCs and highlights their potential in optoelectronic integration. From an application perspective, transparent ferroelectric materials have been explored in several material forms, including bulk ceramics, single crystals, thin films, and composites. These forms differ in processing route, microstructural length scale, optical homogeneity, electromechanical response, and device-integration strategy; therefore, their device performances should not be regarded as directly interchangeable. In this section, application examples based on transparent ferroelectric ceramics are emphasized where available, while selected single-crystal, thin-film, and composite demonstrations are discussed as benchmarks or model systems that reveal transferable device-design principles for future TFCs development.

4.1. Biomedical Imaging

Photoacoustic imaging (PAI) represents one of the most promising application frontiers of transparent piezoelectric materials. PAI is an emerging non-destructive biomedical imaging

technique that uses pulsed laser excitation to generate ultrasonic signals within biological tissues. It combines the high contrast of optical imaging with the deep penetration of ultrasound imaging, enabling high-resolution, high-contrast visualization of biological structures. With tunable optical and acoustic parameters, PAI enables multiscale imaging from the cellular to organ level, showing great promise for early cancer detection, vascular plaque diagnosis, microcirculation imaging, dermatology, and neuroscience. As a rapidly advancing technique, PAI leverages the complementary advantages of optical and ultrasonic modalities [45]. However, conventional PAI systems rely on separate optical and acoustic coupling components for coaxial alignment of light and sound, which often results in bulky configurations and substantial energy loss during transmission. The emergence of transparent ultrasonic transducers (TUTs) provides a solution to this limitation. By allowing the excitation laser pulse to pass directly through the piezoelectric element, TUTs enable perfect coaxial alignment of optical excitation and acoustic detection. This simplifies probe design, improves signal-to-noise ratio (SNR), and enables miniaturization for endoscopic applications [208].

TUTs fabricated from transparent PIN–PMN–PT ferroelectric single crystals can achieve an operating center frequency at approximately 28–30 MHz. They exhibit a bandwidth of 76–78%, as shown in Fig. 26(a-b). Their pulse–echo sensitivity is approximately four times higher than that of conventional $LiNbO_3$ devices, yielding an SNR improvement of approximately 13 dB in microvascular photoacoustic imaging (Fig. 26(b)). Using this TUT, dynamic monitoring of vasoconstriction and vasodilation in the mouse cortex during epileptic seizures was achieved at 0.8 Hz within a 1.5 × 1.5 mm^2 field of view, demonstrating strong potential for functional neuroscience studies (Fig. 26(c-d)). Compared with traditional mechanically scanned systems, these transparent transducers eliminate complex optical–acoustic coupling structures and significantly improve imaging speed and system compactness [124].

TFCs exhibit additional advantages in machinability, cost control, and array fabrication. With appropriate rare-earth doping, PMN–PT transparent ceramics maintain high optical transmittance

while exhibiting excellent piezoelectric performance. For example, Sm^{3+} or Eu^{3+}-doped 72PMN–28PT ceramics exhibit 68–69% transmittance in the visible–near-infrared range and a piezoelectric coefficient $d_{33} \approx$ 1400-1500 pC N^{-1}, approaching single-crystal levels (Fig. 26(e)). Miniature TUTs fabricated from this material (diameter ≈ 3 mm, center frequency 16–28 MHz; Fig. 26(f)) and their corresponding imaging system (Fig. 26(g)) achieved photoacoustic SNRs above 20 dB through 7.5 mm of ex vivo chicken breast tissue and successfully enabled in vivo imaging of subcutaneous microvasculature in the mouse ear (Fig. 26(h)) [61, 63]. These PMN–PT-based transparent ceramic transducers provide stable impedance matching at approximately 50 Ω and can be readily processed into ultrathin plates, making them particularly suitable for miniaturized applications such as endoscopes, catheters, and wearable probes.

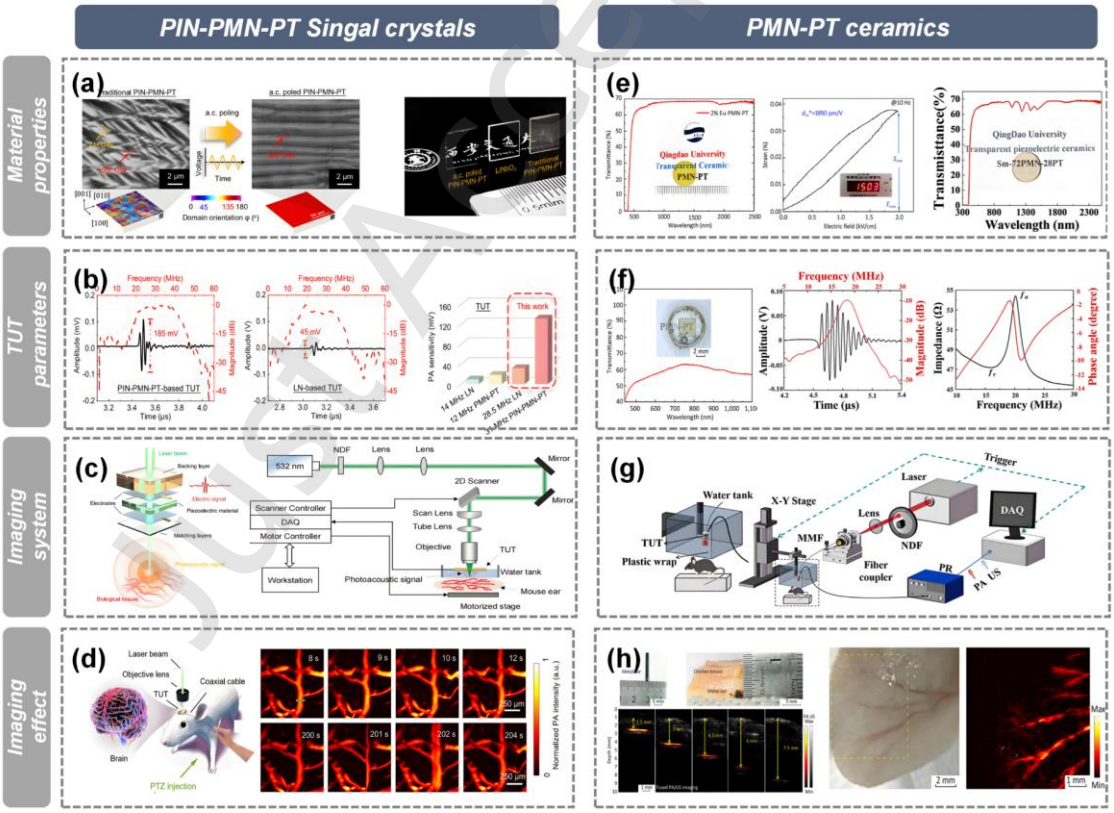

Fig. 26. Applications of transparent PIN–PMN–PT single crystals and PMN–PT–based transparent ceramics in TUT devices and photoacoustic imaging. (a) Transparent piezoelectric PIN–PMN–PT single crystal and its AC-poling engineered domains. Reproduced with permission from Ref. [124], © Springer Nature 2024. (b) TUT performance of the PIN–PMN–PT single crystal. Reproduced with permission from Ref. [124], © Springer Nature

2024. (c) Photoacoustic imaging system based on the PIN–PMN–PT single crystal. Reproduced with permission from Ref. [124], © Springer Nature 2024. (d) Cortical vessel imaging in mice using the single-crystal TUT. Reproduced with permission from Ref. [124], © Springer Nature 2024. (e) Transmittance and piezoelectric performance of PMN–PT ceramics. Reproduced with permission from Ref. [61, 63], © Chinese Ceramic Society 2025; Elsevier BV 2024. (f) TUT performance of PMN–PT ceramics. Reproduced with permission from Ref. [61, 63], © Chinese Ceramic Society 2025; Elsevier BV 2024. (g) Photoacoustic imaging system based on PMN–PT ceramics. Reproduced with permission from Ref. [63], © Elsevier BV 2024. (h) In vivo and ex vivo imaging applications of transparent piezoelectric ceramic TUTs. Reproduced with permission from Ref. [61], © Chinese Ceramic Society 2025.

In summary, transparent ferroelectric single crystals and ceramics play complementary roles in biomedical imaging. Single-crystal TUTs, owing to their superior bandwidth and sensitivity, are well suited to high-resolution and dynamic functional imaging. In contrast, transparent ceramic TUTs offer excellent machinability, short fabrication cycles, and low cost, making them better suited for array implementation and clinical translation. The coordinated development of both material forms is advancing photoacoustic–ultrasound bimodal imaging systems from laboratory prototypes to engineered platforms and preclinical studies. This progress offers new tools for vascular disease monitoring, early tumor diagnosis, and functional neuroimaging.

4.2. Transparent Actuators and Robots

Transparent robots are an important device-level extension of transparent piezoelectric materials. Owing to their high optical transmittance and large field-induced strain (inverse piezoelectricity), these robots function not only as actuators but also as platforms that integrate optical imaging, sensing, and energy-harvesting modules. They offer unique advantages for camouflaged transport, wide-angle visual recording, minimally invasive manipulation, and exploration in low-temperature or specialized environments [125, 209].

In practice, the [011]-oriented PIN–PMN–PT relaxor single crystal exhibits an ultrahigh transverse piezoelectric response ($d_{32}^* \approx 2040$ pm V^{-1}), a T_c of approximately 170°C and 60–70%

transmittance in the visible–near-infrared range, providing a material basis for low-voltage actuation and optical transparency in robotic systems (Fig. 27(a)). Using a biomimetic double-arched beam design (Fig. 27(b)), the transparent robot starts at only 3 V and reaches 276.5 mm s^{-1} (≈ 9.22 body lengths s^{-1}) under 100 V and 1.5 kHz, with power consumption from 85.9 μW to 71.6 mW, significantly outperforming dielectric-elastomer and PVDF-based soft robots [125].

The robot also exhibit remarkable load capacity and stability. With a body mass of only 0.8 g, it can carry up to 78 g (~97.5× body mass) and achieve a turning rate of 51.6° s^{-1} via a dual-unit coupling configuration (Fig. 27(c)). It maintains stable locomotion on inclined surfaces and at ultralow temperatures down to −150°C (Fig. 27(d)). Its optical transparency enables seamless integration with imaging systems, providing a pathway for opto-mechatronic integration in future miniature smart devices.

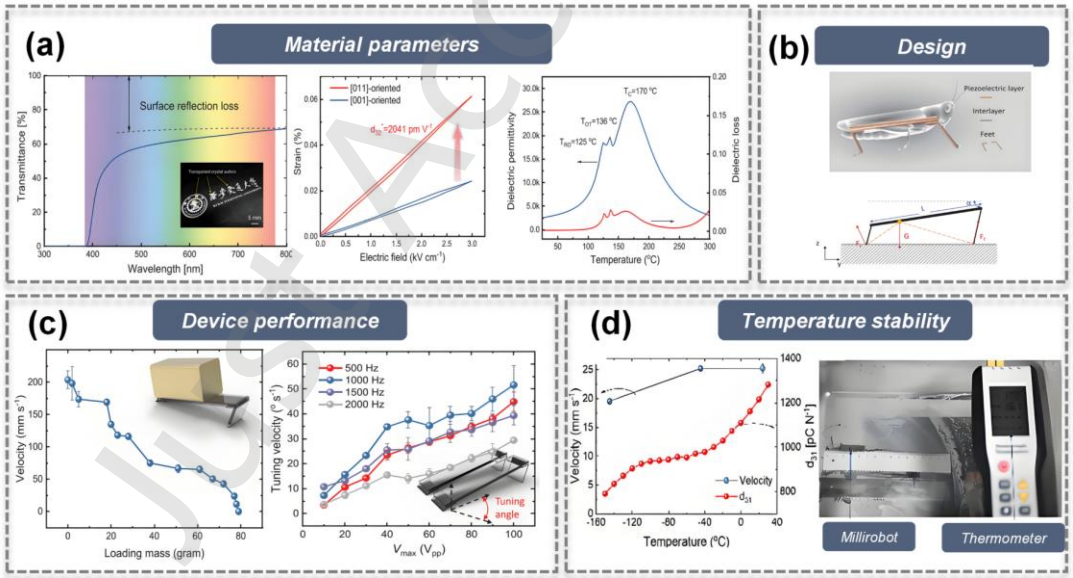

Fig. 27. Transparent robot driven by [011]-oriented PIN–PMN–PT single crystal. Reproduced with permission from Ref. [125], © American Institute of Physics 2022. (a) High transverse piezoelectric response and optical transmittance of the [011]-oriented single crystal. (b) Structural design of the transparent robot based on a double-arched beam configuration. (c) Load-bearing capacity and turning performance of the robot. (d) Stable operation of the transparent robot under low-temperature conditions.

Transparent piezoelectric ceramics enable the creation of "invisible" machines by integrating

actuation, sensing, and optical transmission into a single monolithic structure. These see-through robots, capable of optical camouflage, function as unified platforms where the transparent actuator layer simultaneously serves as a driver, optical window, and potential sensing interface. This architecture permits direct integration with micro-cameras and optical probes, opening scalable pathways for applications in wearable vision, minimally invasive medical manipulation, and stealth robotics. With advances in transparency and energy efficiency, such robots are poised to bridge functional materials and intelligent systems, offering unique solutions for targeted delivery, swarm robotics, and exploration in complex environments.

4.3. Adaptive Transparent Lenses

Conventional adaptive lenses mainly include liquid-crystal lenses and liquid-based lenses, such as electrowetting and dielectric-elastomer types. Liquid-crystal lenses offer a limited focal-tuning range, typically on the millimeter scale. Although structurally simple, electrowetting lenses suffer from slow response (~10 ms), liquid leakage, and optical-axis instability. Dielectric-elastomer lenses can achieve large deformation but require driving voltages exceeding 1 kV, exhibit long response (~10^2 ms), and show poor reliability. These limitations hinder deployment in high-speed imaging, portable devices, and long-term stable operation. Transparent piezoelectric single crystals and ceramics offer a new approach to adaptive lenses. Their high piezoelectric coefficients, excellent optical transmittance, and fast response enable large displacement and wide-range focusing at low voltages while maintaining long-term stability [210].

Using [001]-oriented PIN–PMN–PT transparent single crystals ($d_{33} \approx 1500$ pC N^{-1}, $d_{31} \approx 730$ pC N^{-1}) combined with a radial extension–arching architecture, a high-performance PIN–PMN–PT adaptive lens (PIMNT-ALENS) was developed (Fig. 28(a)) [210]. The device achieves a 53.6 μm displacement and a focal-length tuning range of 57.44 cm^{-1} under 80 Vpp and 4.2 kHz, with a focal sensitivity of 8.5 cm V^{-1} and a rapid response of ~10^2 μs. Notably, the focal sensitivity and response speed outperform those of conventional piezoceramic (10^{-1} cm V^{-1}, 10^3 μs) based and dielectric

elastomer (10^{-2} cm V^{-1}, 10^5 μs) based adaptive lenses by one to two orders of magnitude, underscoring the intrinsic advantages of relaxor ferroelectric single crystals. Moreover, its performance remains stable after more than 4×10^7 operating cycles (Fig. 28(b)).

At the device level, a piezoelectric metasurface based on transparent PIN–PMN–PT single crystals (Fig. 28(c)) enables both linear displacement and rotational motion, supporting autofocus (AF) and optical image stabilization (OIS) [211]. The lens operates stably over 1–400 Hz, with a focal-length range of 35.82 cm to infinity, a displacement of ~5 μm, and a rotational tilt of ~44°, achieving a lightweight design and multifunctional integration (Fig. 28(d)).

Inspired by the human eye and the compound eyes of jumping spiders, solid–liquid-coupled ordered piezoelectric units use a liquid medium to suppress stress transfer, enabling independent cell control and large out-of-plane strain ($\varepsilon_z \approx 1.13\%$) (Fig. 28(e)) [212]. Building on this, a biomimetic piezoelectric adaptive lens (BPAL) achieves wide-range zoom (100.3 mm–∞), ultrahigh diopter sensitivity (70 D mV^{-1}), and ultrafast response (50 μs). When arrayed (BPALA), it provides an almost 180° panoramic field of view and supports multifocal imaging and three-dimensional target focusing (Fig. 28(f)).

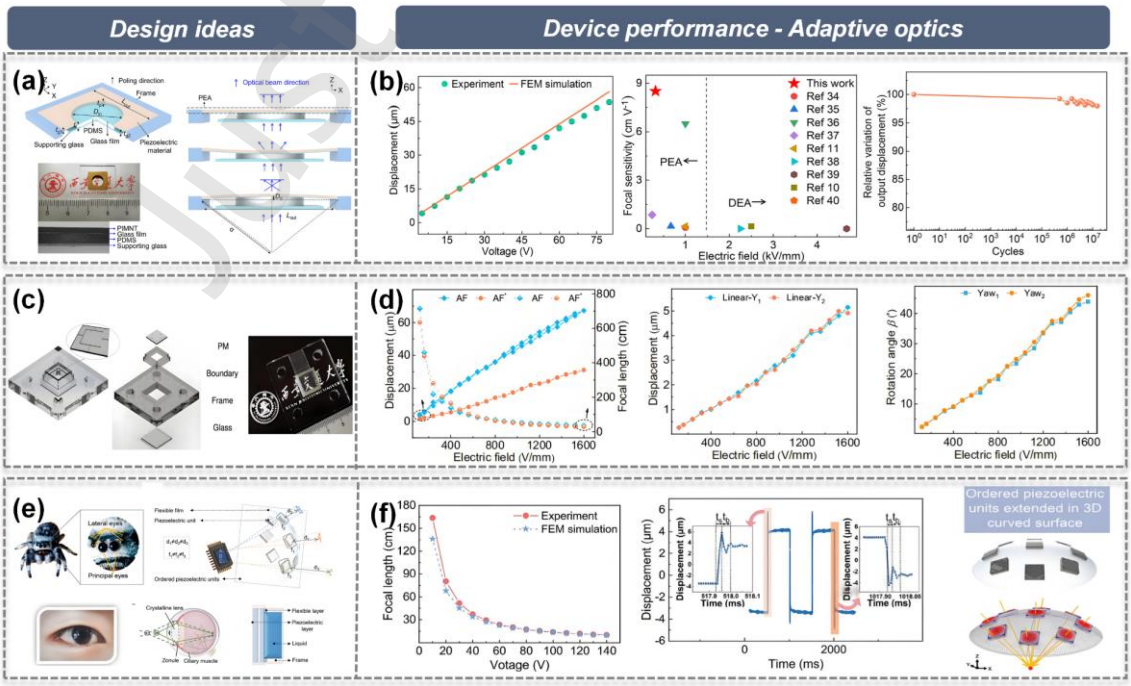

Fig. 28. High-performance adaptive lenses based on transparent PIN–PMN–PT single crystals. (a) Radial stretching–bending structure of a [001]-oriented PIN–PMN–PT adaptive lens (PIMNT-ALENS). Reproduced with permission from Ref. [210], © American Institute of Physics 2022. (b) Displacement and focal length tuning performance of the PIMNT-ALENS. Reproduced with permission from Ref. [210], © American Institute of Physics 2022. (c) Transparent PIMNT single-crystal piezoelectric metasurface structure. Reproduced with permission from Ref. [211], © Springer Nature 2024. (d) Autofocus and optical image stabilization performance of the piezoelectric metasurface lens. Reproduced with permission from Ref. [211], © Springer Nature 2024. (e) Structure of solid–liquid coupled ordered piezoelectric units. Reproduced with permission from Ref. [212], © Wiley-VCH Verlag 2024. (f) Wide field-of-view and three-dimensional focusing imaging of the biomimetic lens and its array. Reproduced with permission from Ref. [212], © Wiley-VCH Verlag 2024.

In summary, transparent ferroelectric adaptive lenses have progressed from high-sensitivity single-crystal actuators to multifunctional metasurfaces and biomimetic, programmable optical arrays. They show strong potential for applications in mobile imaging, wearable vision, micromanipulation, and aerospace optical systems.

4.4. Transparent Loudspeakers

Transparent loudspeakers are a key acoustic application of TFCs. They provide sound output and interactive functions for next-generation transparent electronics, including displays, smart automotive windows, and wearable systems. In conventional electromagnetic speakers, the voice coil and magnet are opaque, complicating their integration with transparent display systems. Although polymer-based piezoelectric films (e.g., PVDF) have good optical transmittance, their limited piezoelectric coefficient ($d_{33} \approx$ -29 pC N^{-1}) yields insufficient sound pressure, requiring high drive voltages to reach audible levels. In contrast, transparent PLZT ceramics combine high optical transmittance with strong piezoelectricity, providing a material basis for efficient, low-voltage transparent acoustic devices.

Recent work reported a transparent PLZT loudspeaker [213]. With composition adjustment near the MPB and oxygen-atmosphere sintering, Lee et al. prepared three ITO-coated and poled PLZT

ceramics showing a clear transparency-piezoelectricity trade-off (Fig. 29(a)). PLZT-S1 (9/68/32) exhibited the highest transmittance of ~65% at 550 nm but a relatively low d_{33} of ~180 pC N^{-1}, whereas PLZT-S2 (9/66/33) and PLZT-S3 (8/66/33) showed higher d_{33} values of ~470 and ~620 pC N^{-1} but lower transmittances of ~42% and ~33%, respectively. Thus, Fig. 29(a) reflects composition- and phase-dependent property variation near the MPB rather than the performance of a single PLZT composition. With ITO electrodes and a transparent glass diaphragm, the PLZT transducer (Fig. 29(b)) delivers up to 105 dB at its 5.6 kHz resonance under a 5 Vpp drive. It has also been used for gas-leak alarms in a transparent cavity, demonstrating potential for high-sensitivity sensing and alarm systems (Fig. 29(c)).

Furthermore, combining PLZT with a flexible PET diaphragm enabled a fully transparent loudspeaker (Fig. 29(d)). Compared with PVDF film speakers, the PLZT speaker requires far lower drive voltage. PVDF, with $d_{33} \approx$ -29 pC N^{-1}, typically needs hundreds of volts to reach 80–100 dB, whereas the PLZT device achieves comparable or higher sound pressure level (SPL) at ~10 Vpp and reproduces voice more faithfully in the 500 Hz–1 kHz band. Compared to commercial PZT speakers, the transparent PLZT speaker maintains similar SPL at mid–high frequencies (> 2 kHz) and provides better waveform fidelity and spectral consistency in the low-frequency voice band, thereby improving speech clarity and naturalness (Fig. 29(e)). Application demonstrations further verified practicality. Mounted on a laptop screen, the transparent PLZT speaker allowed simultaneous video display and audio playback without degrading image clarity, confirming suitability for transparent displays and multifunctional human–machine interaction systems (Fig.29(f)).

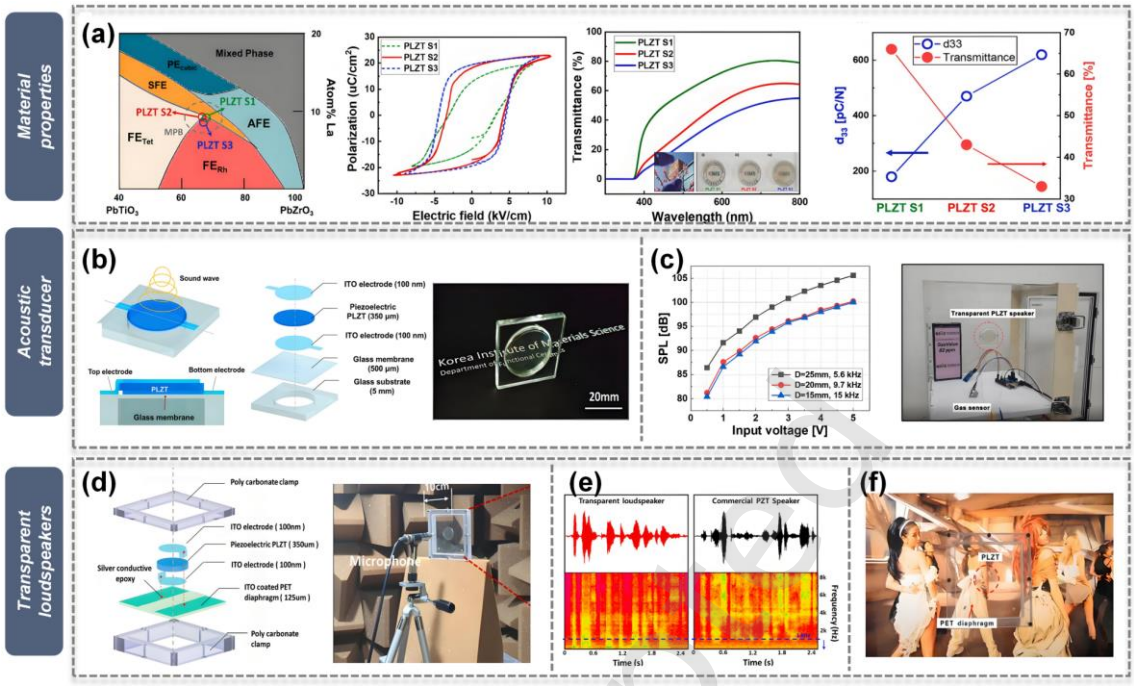

Fig. 29. Fully transparent piezoelectric loudspeaker based on PLZT. Reproduced with permission from Ref. [213], © Multidisciplinary Digital Publishing Institute 2025. (a) Optical transmittance and piezoelectric performance of PLZT ceramics. (b) Structural design of the acoustic transducer. (c) Application of the PLZT transducer in gas-leak alarm systems. (d) Structure of the transparent loudspeaker. (e) Performance comparison among PLZT, PVDF, and PZT loudspeakers. (f) Integration of the PLZT transparent loudspeaker with display and audio systems.

Overall, transparent piezoelectric loudspeakers overcome the limitations of conventional electromagnetic speakers, namely opacity, bulkiness, and high energy consumption. They also address the poor acoustic performance of polymer-based piezoelectric film speakers despite their good transparency. Transparent PLZT ceramics combine high optical transmittance with excellent piezoelectricity, enabling high sound-pressure output at low drive voltages and seamless integration with transparent displays, smart windows, and wearable devices. With further improvements in transparency, lead-free compositions, and system-level integration, transparent loudspeakers are poised to become key components of transparent electronics and multifunctional human–machine interaction systems.

4.5. Information Transmission

TFCs exhibit excellent electro-optic properties, including a large electro-optic coefficient and a

low half-wave voltage, enabling low-drive-voltage, high-speed devices such as electro-optic switches, modulators, optical filters, and polarization controllers. These devices show strong potential for laser modulation, high-speed optical communication, and free-space optical links. For example, in optical switching, traditional MEMS and liquid-crystal switches typically respond on the millisecond scale, whereas magneto-optic switches respond within tens to hundreds of microseconds. In contrast, representative PMN–PT transparent-ceramic electro-optic switches have achieved sub-60 ns response times, demonstrating nanosecond-scale switching capability.

The design and application of optical devices generally require materials with transmittance approaching the theoretical limit. Low transmittance increases insertion loss, causes device heating, and reduces the laser-damage threshold. At present, PMN–PT TFCs that meet application requirements are scarce, which limits research on and deployment of PMN–PT-based electro-optic devices. Optimized PMN–PT transparent electro-optic devices provide both fast response and efficient optical control at relatively low modulation voltages.

Boston Applied Technologies [59] first developed PMN–PT-based electro-optic devices (Fig. 30(a)). Their electro-optic switch features a response time < 60 ns, a 1 MHz repetition rate, insertion loss < 1 dB, and polarization-dependent loss < 0.2 dB. It was the only electro-optic solution among three candidates (the other two were magneto-optic) to pass the European Space Agency's extreme tests. In addition, a low-drive-voltage electro-optic Q-switch (48 V, 200 kHz) was reported, along with a tunable Fabry–Perot optical filter exhibiting 1.6 dB insertion loss, a free-spectral range of 3.5 nm, and a 500 ns tuning time. Under an electric field of 1.0 V μm^{-1}, the filter achieved a 2.1 nm wavelength shift with a maximum tuning range of 6 nm. Variable optical attenuators and polarization controllers have also been developed. Qiao and Zhang [214, 215] subsequently fabricated a high-speed electro-optic switch and a high-power, polarization-independent electro-optic switch based on PMN–PT transparent ceramics, demonstrating the material's potential for electro-optic devices. The former exploited the high electro-optic coefficient, low drive voltage, and weak hysteresis of PMN–

PT to realize a high-speed switch in a Sagnac-interferometer configuration (Fig. 30(b)). The latter used an improved free-space interferometric structure to achieve polarization-independent operation with a 305 V drive voltage, a switching speed of ~180 ns, and an increased laser-damage threshold of 5.79 J cm^{-2}, markedly outperforming conventional $LiTaO_3$ crystals (Fig. 30(c)).

Notably, recent advances in transparent PIN–PMN–PT single crystals have further pushed the performance limits of electro-optic devices. Using a high-temperature poling strategy, Liu et al. [37]eliminated undesired light-scattering domain variants in [011]-oriented PIN–PMN–PT crystals by heating the crystal to ~105–115°C, applying an electric field of 5 kV cm^{-1}, and slowly cooling it under the field. After antireflection coating, the crystal reached a transmittance of 99.6% at 1064 nm. At room temperature, the PIN–PMN–32PT crystal exhibited $r_{33} \approx 910$ pm V^{-1} and an effective EO coefficient $r_c \approx 670$ pm V^{-1}, while r_{33} could reach ~900–2800 pm V^{-1} under different temperature and frequency conditions. The effective rc value is about 30 times higher than those of commercial LN and DKDP crystals ($r_c \approx 21$–24 pm V^{-1}). Based on this material, an ultracompact electro-optic Q-switch was developed, with a volume an order of magnitude smaller than LN or DKDP counterparts and a drive voltage of only 200 V (≈ 1300 V for LN and ≈ 3200 V for DKDP). In a 1064 nm laser cavity, it produced stable pulses with a duration of ~1.8 ns and an energy jitter of 2.7%, demonstrating high repetition rate, low energy consumption, and strong immunity to electromagnetic interference (Fig. 30(d)).

Hu *et al.* [58] developed a three-cavity tunable optical filter (TOF) using PMN–PT transparent ceramics, with a tuning voltage below 30 V and a tuning range of 190–197 THz (Fig. 30(e)). Fang *et al.* [5] demonstrated free-space optical communication at a 200 kHz electro-optic modulation rate with only approximately 200 V of drive, enabling real-time transmission of audio and graphical signals (Fig. 30(f)). Based on this foundation, Tian *et al.* [114] demonstrated a dual-path tunable laser communication system. By adjusting the applied electric field, they continuously controlled the intensity ratio between two optical paths from 160 to 0.01 (Fig. 30(g)) and achieved electric-field-

controlled conversion of the laser polarization state from linear to elliptical to circular (Fig. 30(h)), validating the potential for optical communications and polarization-control devices.

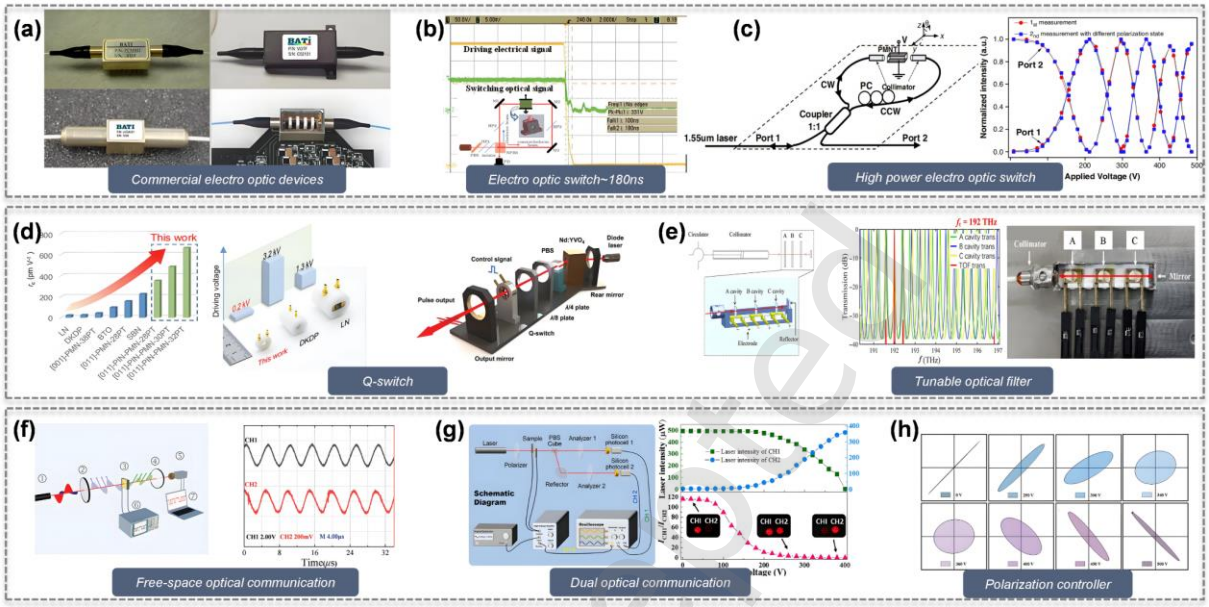

Fig. 30. Electro-optic devices based on PMN–PT and PIN–PMN–PT transparent ferroelectric materials. (a) PMN–PT electro-optic device developed by Boston Applied Technologies. Reproduced with permission from Ref. [59], © SPIE 2005. (b) High-speed electro-optic switch based on a Sagnac interferometer. Reproduced with permission from Ref. [215], © IOP Publishing Ltd 2016. (c) High-power polarization-independent electro-optic switch. Reproduced with permission from Ref. [214], © Elsevier 2011. (d) Electro-optic Q-switch based on PIN–PMN–PT single crystal. Reproduced with permission from Ref. [37], © American Association for the Advancement of Science 2022. (e) PMN–PT transparent ceramic three-cavity tunable optical filter. Reproduced with permission from Ref. [58], © Tsinghua University Press 2023. (f) Free-space optical communication experiment. Reproduced with permission from Ref. [5], © John Wiley and Sons Inc 2021. (g) Dual-path tunable laser communication system. Reproduced with permission from Ref. [114], © Elsevier Ltd 2023. (h) Electric-field-controlled polarization converter. Reproduced with permission from Ref. [114], © Elsevier Ltd 2023.

4.6. Optical Sensors

TFCs, owning to their high optical transmittance and excellent electrical properties, have begun to show unique advantages in optical sensing. Compared with traditional optical-sensing materials, they not only ensure efficient light transmission but also enable multiphysical coupling via

ferroelectric polarization, energy storage, and luminescence. This enables the construction of transparent, self-powered, and optically readable integrated sensors. With these capabilities, transparent ferroelectric ceramics show strong potential for applications in temperature monitoring, energy-storage–sensing integration, smart displays, and environmental monitoring.

Recent studies demonstrated that BNT-based transparent photochromic and upconversion-luminescent ceramics can be used in bioinspired search-and-rescue robots. Designed for complex environments such as fires or earthquakes, where power failure, darkness, and high temperature coexist, these materials operate stably under heat and emit red–green upconversion luminescence through Ho^{3+} doping, improving visibility in dark conditions. Combined with FIR technology, the sensors can monitor ambient temperature in real time, helping rescuers plan optimal escape routes. Upon target detection, the material emits strong pulsed signals to transmit both location and temperature information, greatly improving rescue efficiency and safety in disaster scenarios (Fig. 31(a)) [54]. In electric vehicles and power-electronics safety management, BNT-based transparent energy-storage optical sensors maintain a stable temperature response ($S_r \approx 0.04$ K^{-1}) between 25°C and 220°C. They provide real-time temperature feedback of battery cells and power modules, while featuring rapid energy release (~67 ns) and high power density (243 MW cm^{-3}), enabling them to trigger alarms or circuit cutoffs under overheating. This dual sensing–protection functionality makes them ideal for thermal monitoring and overheat protection in next-generation vehicles and high-power devices (Fig. 31(b)) [56]. Moreover, entropy engineering and defect-dipole modulation endow these ceramics with multiphase relaxor behavior and nanoscale polarization-domain synergy, enhancing polarization reversibility and breakdown strength while reducing hysteresis loss. Consequently, these materials exhibit excellent energy-storage performance ($W_{rec} \approx 11.23$ J cm^{-3}, $\eta \approx 90.9\%$, $E_b \approx 670$ kV cm^{-1}) and display a distinctive negative-thermal-expansion effect in their emission spectra, allowing temperature variations to be visualized directly via optical signals. Based on these properties, researchers proposed their application in implantable defibrillators and

pacemaker capacitors, where the material delivers high-energy pulses for therapy while simultaneously enabling optical temperature monitoring to prevent overheating and secondary tissue damage (Fig. 31(c)). This integrated "energy-storage + sensing" model provides a novel safety-monitoring concept for implantable medical electronics [55].

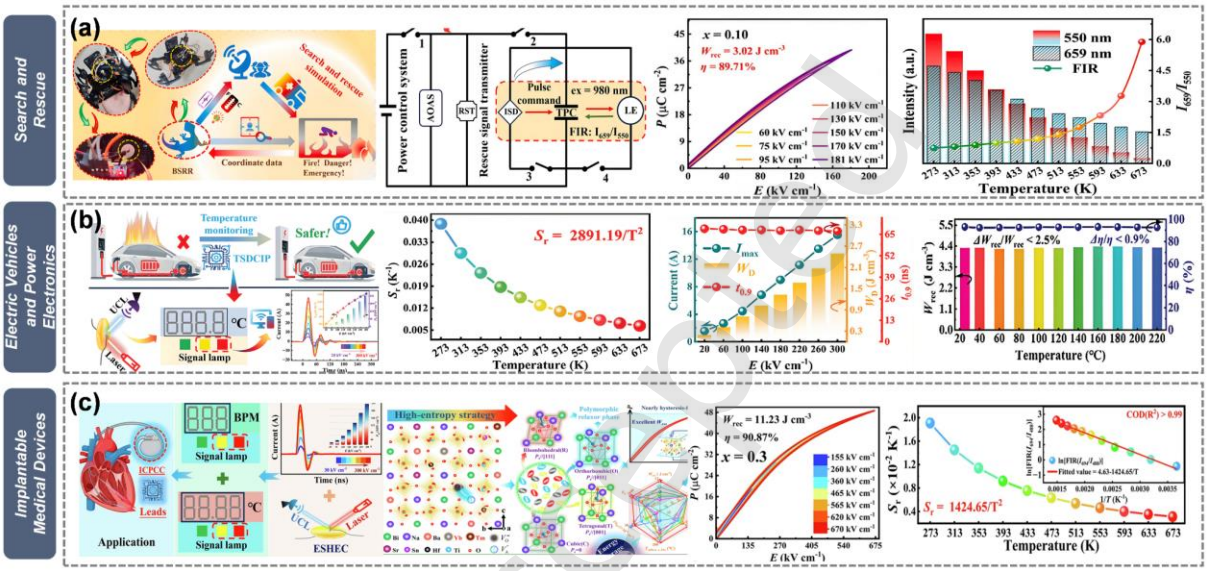

Fig. 31. Optical-sensing strategies and representative applications of transparent ferroelectric ceramic systems. (a) Bioinspired search-and-rescue applications under extreme disaster environments. Reproduced with permission from Ref. [54], © Elsevier 2024. (b) Temperature monitoring and overheating protection in electric vehicles and power electronic systems. Reproduced with permission from Ref. [56], © Wiley-VCH Verlag 2025. (c)Integrated energy-storage and optical temperature-monitoring applications in implantable medical devices. Reproduced with permission from Ref. [55], © Springer Nature 2025.

Overall, transparent ferroelectric optical sensors are advancing from single-function temperature detection to multifunctional integration which combines transparency, energy storage, luminescence, and photochromism. Their advantages include high optical transmittance and sensitivity, as well as strong coupling among energy-storage capability, device stability, and biomedical applicability. Looking ahead, continued advances in rare-earth energy-level engineering, high-entropy structural design, and transparent-electrode fabrication are expected to drive practical breakthroughs in automotive battery safety monitoring, implantable medical devices, smart displays, and extreme-

environment sensing.

4.7. Displays and Intelligent Optical Control

Transparent ferroelectric ceramics with photochromic functionality maintain high optical transmittance while exhibiting reversible color change and tunable luminescence intensity under light stimulation. This dual functionality enables energy-efficient light regulation for smart windows and information-processing operations such as "write–erase–rewrite" for optical storage or encryption, showing strong potential for smart-window and optical-information-storage applications [197-199, 216]. In these application fields, photochromic films and glasses have already provided mature device-level demonstrations, whereas transparent photochromic ceramics are still mainly at the material-demonstration stage. Therefore, in this section, film- and glass-based examples are discussed as application benchmarks, while KNN- and $NaNbO_3$-based transparent ceramics are highlighted as ceramic platforms with potential for future device translation. Existing transparent photochromic ceramics show high transmittance and excellent compositional–structural tunability in the visible and near-infrared regions, demonstrating their feasibility for future window-scale or information-storage applications [50, 194, 203, 205].

In the context of smart windows, photochromic glass and films have already undergone systematic demonstrations and near-industrial validation, serving as representative "real-world" examples. One representative example is a scalable Cu-doped WO_3/PMMA photochromic film. While maintaining high visible transmittance (T_{lum} = 91%), it provides strong modulation of visible light and solar irradiance (ΔT_{lum} = 73%, ΔT_{sol} = 73%, ΔSHGC = 0.5), verified by both simulations and experiments for building-energy savings and glare comfort (Fig. 32(a)). It also shows potential as a coating for electronic-device screens (Fig. 32(b)) [199]. Another class combines passive photochromism with active electrochromism to form "dual-response" smart windows. Based on WO_3-EG-Ag films, the device exhibits large, simultaneous modulation in the visible and near-infrared regions (700 nm: 75.9%, 1000 nm: 76.7%, 2000 nm: 69.2%), a fast reversible response, and

four operation modes ("photodriven bright-cool/dark-cool," "electrically bleached," and "photodriven self-bleaching") for all-weather control of transmittance and thermal radiation (Fig. 32(c)) [217]. Compared with these film- and glass-based benchmarks, transparent photochromic ceramics have not yet been demonstrated as direct window devices. However, their superior thermal and mechanical stability, along with integrable multiphysics coupling (electro-optic, piezoelectric, and luminescent), may provide smart-window solutions where glass falls short, especially under high-temperature, high-stress, or extreme conditions. Moreover, transparent KNN-based ceramics already exhibit "window-grade" appearance with high transmittance and strong photochromism (Fig. 32(d)), providing a solid property basis for future translation from materials to devices [72, 196].

In optical-information storage, research is shifting toward three-dimensional (3D), high-density, and high-security architectures. Currently, glass-based systems provide a mature paradigm. For instance, femtosecond-laser-induced in situ reversible "write-erase" of $CsPbBr_3$ perovskite quantum dots in a transparent glass matrix enables controllable 3D fluorescent patterning that can be cyclically erased and restored, offering high stability and easy integration for high-density 3D storage, optical encryption, and micro-patterning applications (Fig. 32(e)) [216]. In addition, rare-earth–Ag co-doped glass exhibits high-contrast, reversible luminescence modulation and excellent cycling stability under alternating 365 nm excitation and 690 nm bleaching, enabling rewritable 3D information encoding and QR-code encryption/readout, and demonstrating a scalable route from two-dimensional (2D) to 3D optical data storage (Fig. 32(f)) [198]. Correspondingly, transparent photochromic ceramics can realize not only 2D optical-information storage , owing to their intrinsic transparency, but also possess the potential for true 3D information recording, which distinguishes them from opaque ceramic systems. For example, Ba/Pr co-doped KNN transparent ceramics allow real-time "handwriting" recording with a laser pointer, showing long-term pattern retention and visible-light/thermal erasability (Fig. 32(g)) [111]. From a structural-design perspective, the $NaNbO_3:Eu^{3+}$-based rotational-encoding disk introduces the "phase angle" as an additional degree of

freedom in optical encoding, significantly enhancing encryption dimensionality and capacity. The material also exhibits high luminescence efficiency (quantum yield ≈ 38.6%) and strong on/off contrast, providing both material and device-level evidence for high-security, multidimensional optical-data storage (Fig. 32(h)) [218].

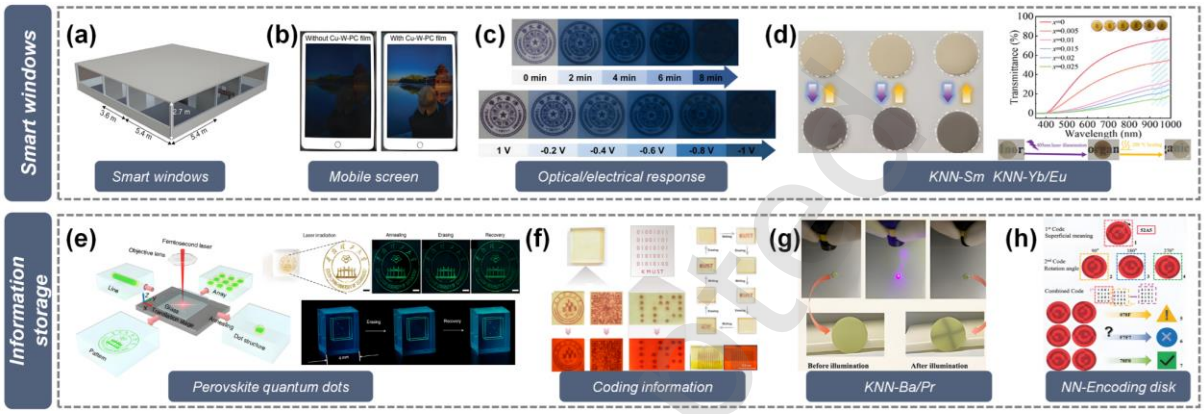

Fig. 32. Benchmark demonstrations and ceramic platforms for smart windows and optical information storage. (a) Application of photochromic films in building energy efficiency. Reproduced with permission from Ref. [199], © Wiley-Blackwell 2024. (b) Potential use of photochromic films on electronic device screens. Reproduced with permission from Ref. [199], © Wiley-Blackwell 2024. (c) Example of a dual-response smart window combining photochromic and electrochromic effects. Reproduced with permission from Ref. [217], © Wiley-VCH Verlag 2025. (d) "Window-grade" appearance and performance of KNN-based transparent photochromic ceramics. Reproduced with permission from Ref. [72, 196], © John Wiley and Sons Inc 2021; American Chemical Society 2024. (e) Femtosecond-laser-induced write–erase 3D information storage. Reproduced with permission from Ref. [216], © Springer Nature 2019. (f) QR code encryption using photochromic glass. Reproduced with permission from Ref. [198], © American Chemical Society 2022. (g) Real-time laser handwriting and erasable behavior of KNN-based transparent photochromic ceramics. Reproduced with permission from Ref. [111], © American Chemical Society 2023. (h) Rotational encoding disk based on $NaNbO_3$ ceramics. Reproduced with permission from Ref. [218], © Wiley-VCH Verlag 2024.

In summary, photochromic films and glasses have established reproducible application routes for energy-saving smart windows and 3D optical information storage and encryption, including high transmittance with large modulation depth, four-mode photoelectrochromic windows, and

femtosecond-laser-written reversible 3D patterns. Transparent photochromic ceramics combine superior thermal stability, fatigue resistance, mechanical strength, and multiphysics-coupling capability, positioning them to extend these applications toward more demanding and high-security conditions. Specifically, they are promising for long-term stable smart windows in architectural and transportation settings, with optional integration of electro-optic or piezoelectric units for coordinated active and passive control, and for multidimensional or 3D information storage and encryption that incorporates rotational degrees of freedom and high-contrast luminescent read/write operations. Experimental studies on KNN-based materials already show high transparency and a window-like appearance, as well as real-time handwriting, reversible erasure, and multidimensional encoding in KNN/NN-based devices. With continued advances in doping and defect engineering, transparent-electrode design, and bulk-writing processes such as femtosecond-laser inscription, transparent photochromic ceramics are expected to progress from material demonstrations to functional devices, enabling complementary and upgraded technological pathways for smart windows, optical encryption, and multidimensional information storage.

5. Summary and Outlook

TFCs have emerged as a transformative research frontier by merging high optical transparency with a suite of functional properties—including ferroelectric, electro-optic, piezoelectric, photoluminescent, and photochromic properties. This review provides a comprehensive overview of material systems, beginning with the fundamental mechanisms that enable transparency and the processing strategies that achieve it. We then systematically map recent progress across five key functional classes—piezoelectric, electro-optic, luminescent, energy-storage, and photochromic ceramics—detailing their material design, underlying physics, and performance benchmarks. The practical potential of TFCs is demonstrated through emerging applications in biomedical photoacoustic imaging, transparent robotics and actuators, adaptive lenses and optical control, transparent acoustic devices optical communication, electro-optic modulation, optical sensing, smart

windows, and optical information storage. This progression from materials to mechanisms to applications underscores the interdisciplinary significance of TFCs as a versatile "transparent multifunctional platform."

Despite considerable promise, the translation of TFCs into engineered products still face several key challenges. Future efforts must prioritize several key directions, as illustrated in Fig. 33, to advance these materials from fundamental research to practical implementation.

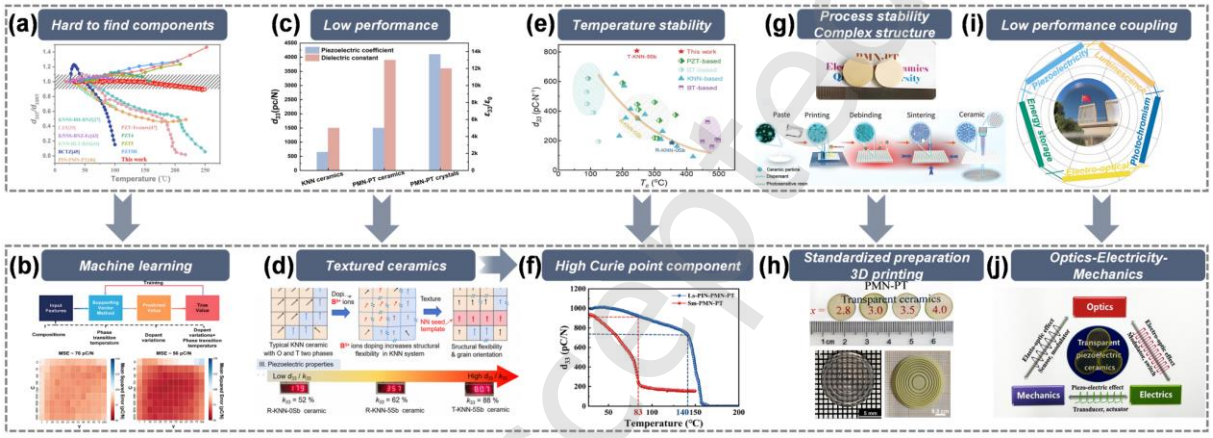

Fig. 33. Future research focuses of transparent ferroelectric ceramics. (a) Complex and difficult-to-control compositions. Reproduced with permission from Ref. [219], © Springer Nature 2024. (b) Machine learning. Reproduced with permission from Ref. [220], © Wiley-VCH Verlag 2025. (c) Ceramic performance is difficult to surpass that of single crystals. (d) Textured ferroelectric ceramics. Reproduced with permission from Ref. [221], © Springer Nature 2025. (e) Poor temperature stability. Reproduced with permission from Ref. [221], © Springer Nature 2025. (f) High-Curie-temperature systems. Reproduced with permission from Ref. [20], © American Institute of Physics 2024. (g) Poor process stability and difficulty in machining complex structures. Reproduced with permission from Ref. [222], © Wiley-Blackwell 2021. (h) 3D printing. Reproduced with permission from Ref. [104, 222], © Elsevier Ltd 2017; Wiley-Blackwell 2021. (i) Difficulty in coupling multiple properties. (j) Multifunctional application scenarios. Reproduced with permission from Ref. [64], © American Chemical Society 2023.

5.1. From trial-and-error to Intelligent Design

Current doping and compositional optimization remain largely empirical with trial-and-error approach, slowing the discovery of new compositions. (Fig. 33(a)). Taking KNN as an example,

high-performance ceramics often require more than five dopant elements, and the doping levels must be finely controlled, resulting in heavy experimental workloads and slower progress [67, 68]. Recent studies indicate that machine learning and computational modeling are changing this situation (Fig. 33(b)) [223]. For example, Zou [220] *et al.* combined machine learning with density functional theory (DFT), phase-field simulations, and STEM to show that Sb doping in KNN weakens local ferroelectric distortions and lowers the polarization-rotation barrier, thereby explaining the origin of its ultrahigh piezoelectricity. Yao *et al.* [224] introduced the concept of "fluctuating local polarization". By quantifying the magnitude and orientational disorder of local polarization vectors, they showed that fluctuating local polarization is a universal fingerprint directly correlated with piezoelectric enhancement in both Pb-based and Pb-free systems. These studies provide atomistic insights and quantitative design metrics for doping. In parallel, machine learning can rapidly identify the key factors that govern performance when supplied with large datasets. Combined with high-throughput computation and experimental platforms, it enables composition–structure–property databases for rapid screening and prediction, shifting TFCs from experience-driven to data-driven design. As data-centric methods converge with atomistic studies, the field is poised to move beyond trial-and-error and to accelerate the discovery and optimization of new high-performance compositions.

5.2. Bridging the Performance gap with single crystals

Transparent ferroelectric single crystals (e.g., PMN–PT and PIN–PMN–PT) exhibit outstanding piezoelectric and electro-optic properties, including higher d_{33} and larger electromechanical-coupling factors (k_{33}). These advantages enable higher sensitivity, spatial resolution, and penetration depth in piezoelectric receiving transducers and photoacoustic imaging devices [225, 226]. At present, PVDF films and LN crystals are relatively mature transparent piezoelectric materials for photoacoustic imaging, benefiting from good optical transparency, acoustic compatibility, and processing reliability [227]. However, their relatively low piezoelectric response still limits ultrasonic detection sensitivity,

especially for high-resolution or deep-tissue imaging. While TFCs offer processing and cost advantages, their functional properties (e.g., piezoelectric coefficients, electromechanical coupling) still generally lag behind those of single crystals due to random grain orientation (Fig. 33(c)) [127, 228]. The shortfall mainly reflects random grain orientation in ceramics, where property averaging over polycrystalline orientations limits polarization alignment and functional anisotropy compared with single-crystal domain alignment.

Texturing engineering—aligning grains along functional crystallographic directions—is a critical pathway to create "quasi-single-crystal" ceramics and bridge the performance gap between ceramics and single crystals (Fig. 33(d)). Using techniques such as templated grain growth, magnetic-field alignment, and electric-field-assisted orientation, grains can be oriented along specific crystallographic directions, allowing macroscopic properties to approach those of single crystals. For example, highly textured PZT ceramics achieved $d_{33} \approx 760$ pC N^{-1}, $g_{33} \approx 100$ mV m N^{-1}, and $k_{33} \approx 0.85$, surpassing the overall performance of some PMN–PT single crystals [18, 229]. In the KNN system, texturing has likewise shown remarkable potential. Introducing structural flexibility via Sb doping and combining it with crystallographic alignment enables textured KNN ceramics to achieve $d_{33} \approx 807$ pC N^{-1}, $k_{33} \approx 0.88$, and $T_c \approx 245$°C [221]. Moreover, a medium-entropy design combined with texturing overcomes the saturation-polarization limitation in KNN. The textured ceramics achieved $d_{33} \approx 680$ pC N^{-1} and $k_p \approx 72.5\%$ while maintaining a high T_c (~260°C). They also showed excellent performance in energy harvesting and ultrasonic-transducer applications, with an output power density of 57.9 μW mm^{-3}, comparable to or exceeding that of some lead-based ceramics [230]. In summary, texturing offers a cost-effective pathway to high-performance TFCs. Integrating compositional design with texture control can simultaneously enhance piezoelectric while maintaining high transparency and scalability. Looking ahead, optimizing texturing techniques under transparency constraints will be crucial to realizing textured TFCs that can replace single crystals in cutting-edge applications, including biomedical imaging, photoacoustic detection, and high-

performance transducers.

5.3. Ensuring operational stability at elevated temperatures

TFCs generally have low T_c, making them susceptible to depolarization at elevated temperatures and directly compromising device lifetime and operational stability (Fig. 33(e)). For example, in newly developed PMN–PT transparent electro-optic switches, increasing the operating temperature from 20°C to 45°C raised the switching threshold from 206 V to 541 V, revealing strong temperature sensitivity [214]. Such limited electrical stability restricts deployment in power electronics, aerospace, and other harsh environments. Overall, lead-based PMN–PT systems exhibit excellent piezoelectric and electro-optic responses but typically have Curie temperatures below ~120°C, resulting in inadequate thermal stability [64]. By contrast, lead-free KNN exhibits an intrinsically high T_c (> 400°C when undoped). However, the compositional modifications required to shift the R–O–T polymorphic phase boundary toward room temperature are typically accompanied by temperature instability, so that the enhanced electrical properties are confined to a limited temperature range [67].

Current improvement strategies principally fall into two categories:

1) High-T_c compositional design for enhanced thermal stability. Recent studies show that PIN–PMN–PT-type TFCs with trace rare-earth modification can maintain high transparency, and improve piezoelectric and electro-optic responses. Compared with conventional PMN–PT, they offer a broader stable operating window and smaller temperature drift (Fig. 33(f)), making them promising for high-power electro-optic modulation and in-vivo/in-situ applications [20, 64].

2) Texture engineering to improve thermal stability. Multiple reports show that combining <00l> preferential orientation with phase-structure tuning (broadening or diffusing the polymorphic phase boundary) converts orientation-averaged polycrystalline properties into quasi-single-crystal-like responses, markedly reducing the temperature dependence of key parameters such as d_{33}. This approach has been validated in KNN-based 1–3 composite transducers and energy-

harvesting/ultrasonic devices, which exhibit flatter temperature–performance curves and more reliable wide-temperature operation than conventional polycrystalline counterparts [19, 219, 231].

When integrating High-T_c compositional, textured processing, and intelligent thermal management can mitigate environmental disturbances and enhance operational robustness, these measures cannot circumvent the intrinsic limitations of a low Curie temperature. Therefore, achieving reliable high-temperature performance fundamentally depends on materials design and processing optimization that prioritize intrinsic thermal stability from the outset.

5.4. Enabling scalable and complex fabrication

The fabrication of TFCs is highly sensitive to processing parameters. Even slight deviations can reduce transmittance, increase porosity or impurity residues, and thereby induce severe optical scattering and electrical losses. Although laboratory techniques such as HPS and SPS can yield high-quality samples, their narrow processing windows and limited reproducibility hinder scale-up to large sizes or batch production. Future progress should focus on several directions. First, standardize powder synthesis to ensure raw-material purity, uniform particle-size distribution, and compositional homogeneity, thereby minimizing batch-to-batch variation in optical and functional performance. Second, optimize sintering and densification to develop wider-window, more tolerant processes—such as HIP, multistep sintering, and liquid-phase-assisted sintering—that achieve high density and low scattering while maintaining scalability. Third, implement in-situ monitoring and feedback control systems, for example real-time tracking of gas atmosphere, temperature gradients, and densification kinetics, to enable precise adjustment of critical parameters and improve reproducibility and yield.

Moreover, additive manufacturing (3D printing) has opened new avenues for designing complex architectures in transparent ceramics (Fig. 33(g)) [222, 232-234]. Combined with HIP or transparency-enhanced sintering, 3D printing preserves high density and optical quality, improves microstructural uniformity, and enables direct fabrication of intricate geometries such as curved

surfaces, microchannels, and integrated components. Representative progress was reported by Zheng *et al.* [235], who fabricated complex structured Sm-doped PMN–PT ceramics via digital light processing. The ceramics exhibited a high d_{33} of 1285 pC N^{-1} together with dense microstructures, and an annular array ultrasonic transducer was successfully constructed with device performance comparable to that of conventionally processed ceramics. This capability is particularly valuable for optoelectronic and electromechanical devices, including transparent electro-optic switches, photoacoustic imaging probes, miniature transducers, and integrated sensors, where miniaturization, structural complexity, and functional customization are required. Integrating 3D printing provides a promising route for prototyping and multifunctional integration, serving as a critical bridge from laboratory research to real-world applications of transparent ceramics (Fig. 33(h)).

5.5. Multi-Property Coupling and System-Level Integration

The unique advantage of TFCs is the combination of optical transparency and multifunctional coupling, yet the interrelationships among these properties are often poorly coordinated (Fig. 33(i)). For example, most TFCs rely on rare-earth-ion doping to introduce luminescence while retaining ferroelectric or electro-optic behavior. However, current research largely focuses on optical characteristics, such as upconversion/downconversion emission and photochromism, while neglecting intrinsic ferroelectricity, namely the ability of an external electric field to induce polarization switching. Looking ahead, future efforts must move beyond simply adding dopants for luminescence or photochromism, toward actively coupling these optical responses with ferroelectric polarization switching. This would enable electric-field-tunable emission, optically-gated memory, or mechanically-responsive coloring—opening entirely new device concepts in smart displays, multimodal sensing, and interactive photonics (Fig. 33(j)). More broadly, coupling electro-optic modulation with mechanical stress or strain may provide an additional route to stabilize or dynamically tune optical responses under varying temperatures. In biomedical applications, transparent piezoelectric detection could also be integrated with electro-optic light-intensity control,

enabling compact photoacoustic platforms that combine imaging, optical-dose regulation, and laser-assisted therapy.

In summary, TFCs are transitioning from a focus on individual property optimization to holistic co-design of transparency, functionality, stability, and integrability. Success in this endeavor will depend on converging advances in computational materials science, precision processing, and cross-disciplinary device engineering. By tackling these outlined challenges, TFCs are set to mature from a compelling research topic into an enabling technology platform, driving innovation in biomedical imaging, transparent electronics, adaptive optics, and the broader ecosystem of intelligent, interactive material systems.

List of Abbreviations and Symbols

Abbreviation	Full name or definition	Abbreviation	Abbreviation/Symbol
TFCs	Transparent ferroelectric ceramics	P phase	Pseudocubic phase
PMN–PT	$Pb(Mg_{1/3}Nb_{2/3})O_3$–$PbTiO_3$	MPB	Morphotropic phase boundary
KNN	$(K,Na)NbO_3$	PPB	Polymorphic phase boundary
BTO	$BaTiO_3$	PNRs	Polar nanoregions
PZT	$Pb(Zr,Ti)O_3$	T_c	Curie temperature
BNT	$Bi_{0.5}Na_{0.5}TiO_3$	d_{33}	Piezoelectric coefficient
PLZT	$(Pb,la)(Zr,Ti)O_3$	K_p	Planar electromechanical coupling coefficient
PVDF	Polyvinylidene fluoride	DCP	Direct-current poling
LN	$LiNbO_3$	ACP	Alternating-current poling
HIP	Hot isostatic pressing	EO	Electro-optic
HPS	Hot-press sintering	r_c	Effective electro-optic coefficient
SPS	Spark plasma sintering	E_b	Breakdown electric field
R phase	Rhombohedral phase	η	Energy storage efficiency
O phase	Orthorhombic phase	W_{rec}	Recoverable energy-storage density
T phase	Tetragonal phase	E_g	Band gap
C phase	Cubic phase	ΔR_T	Transmittance modulation ratio

Funding (if applicable)

This work was financially supported by the National Natural Science Foundation of China (Grant Nos. 52272116 and 12132020), the Taishan Scholar Program of Shandong Province (Grant No. tstp20240511) and the Guangxi Key Technologies R&D Program (Grant No. 2024AB09025).

Author contributions (mandatory)

Yaqi Wang: Conceptualization, Data curation, Writing – original draft. Chengwu Li: Investigation, Writing – original draft. Jianyi Liu: Resources, Supervision. Zhiyan Chen: Resources, Supervision. Yalin Qin: Supervision, Writing – review & editing. Yongcheng Zhang: Resources, Supervision, Writing – review & editing. Shujun Zhang: Supervision, Writing – review & editing.

Availability of data and materials (mandatory)

The data that support the findings of this study are available from the corresponding author upon reasonable request.

Competing interests (mandatory)

The authors have no competing interests to declare that are relevant to the content of this article.

References

[1] Scott JF. Ferroelectric memories today. *Ferroelectrics* 2000, **236**: 247-58.

[2] Jin HN, Gao XY, Ren KL*, et al.* Review on Piezoelectric Actuators Based on High-Performance Piezoelectric Materials. *IEEE Trans Ultrason Ferroelectr Freq Control* 2022, **69**: 3057-69.

[3] Lin DM, Kwok KW. Piezoelectric Properties of $K_{0.47}Na_{0.47}Li_{0.06}NbO_3$-$NaSbO_3$ Lead-Free Ceramics for Ultrasonic Transducer Applications. *Int J Appl Ceram Technol* 2011, **8**: 684-90.

[4] Pithan C, Hennings D, Waser R. Progress in the Synthesis of Nanocrystalline $BaTiO_3$ Powders

for MLCC. *Int J Appl Ceram Technol* 2005, **2**: 1-14.

[5] Fang Z, Jiang XD, Tian X*, et al.* Ultratransparent PMN-PT Electro-Optic Ceramics and Its Application in Optical Communication. *Adv Opt Mater* 2021, **9**: 2002139.

[6] Peng XW, Yang B, Deng DJ*, et al.* Lead-free KNN-based ceramics incorporated with $Bi(Zn_{2/3}Nb_{1/3})O_3$ possessing excellent optical transmittance and superior energy storage density. *Mater Res Bull* 2023, **165**: 112294.

[7] Xu QQ, Tao Y, Wang ZX*, et al.* Highly Flexible, High-Performance, and Stretchable Piezoelectric Sensor Based on a Hierarchical Droplet-Shaped Ceramics with Enhanced Damage Tolerance. *Adv Mater* 2024, **36**: e2311624.

[8] Zhang GZ, Zhao P, Zhang XS*, et al.* Flexible three-dimensional interconnected piezoelectric ceramic foam based composites for highly efficient concurrent mechanical and thermal energy harvesting. *Energy Environ Sci* 2018, **11**: 2046-56.

[9] Su HX, Wang XB, Li CY*, et al.* Enhanced energy harvesting ability of polydimethylsiloxane-$BaTiO_3$-based flexible piezoelectric nanogenerator for tactile imitation application. *Nano Energy* 2021, **83**: 105809.

[10] Yu D, Zheng ZP, Liu JD*, et al.* Superflexible and Lead-Free Piezoelectric Nanogenerator as a Highly Sensitive Self-Powered Sensor for Human Motion Monitoring. *Nanomicro Lett* 2021, **13**: 117.

[11] Vopson MM, Tan XL. Four-State Anti-Ferroelectric Random Access Memory. *IEEE Electron Device Lett* 2016, **37**: 1551-4.

[12] Ning YT, Pu YP, Wu CH*, et al.* Enhanced capacitive energy storage and dielectric temperature stability of A-site disordered high-entropy perovskite oxides. *Journal of Materials Science & Technology* 2023, **145**: 66-73.

[13] Chu LW, Prakash KN, Tsai M-T*, et al.* Dispersion of nano-sized $BaTiO_3$ powders in nonaqueous suspension with phosphate ester and their applications for MLCC. *J Eur Ceram Soc* 2008, **28**: 1205-12.

[14] Batra AK, Aggarwal MD, Edwards ME*, et al.* Present Status of Polymer: Ceramic Composites for Pyroelectric Infrared Detectors. *Ferroelectrics* 2010, **366**: 84-121.

[15] Zhang SJ, Li F, Jiang XN*, et al.* Advantages and Challenges of Relaxor-$PbTiO_3$ Ferroelectric Crystals for Electroacoustic Transducers- A Review. *Prog Mater Sci* 2015, **68**: 1-66.

[16] Wang HR, Chen ZF, Xie HK. A high-SPL piezoelectric MEMS loud speaker based on thin ceramic PZT. *Sens Actuators, A* 2020, **309**: 112018.

[17] Wang WJ, Jiang Y, Thomas PJ. Structural Design and Physical Mechanism of Axial and Radial Sandwich Resonators with Piezoelectric Ceramics: A Review. *Sensors* 2021, **21**.

[18] Li JL, Qu WB, Daniels J*, et al.* Lead zirconate titanate ceramics with aligned crystallite grains. *Science* 2023, **380**: 87-93.

[19] Yang HR, Tang LM, Han SP*, et al.* Ultra-Stable Thermal Piezoelectricity up to 200 °C in High-Performance KNN-Based Textured Piezoceramics. *Adv Funct Mater* 2025: 2507702.

[20] Fu DS, Wang YQ, Zheng WJ*, et al.* Enhanced piezoelectricity and temperature stability in La-doped PIN-PMN-PT transparent ceramics by composition regulation. *Appl Phys Lett* 2024, **125**: 242905.

[21] Li F, Wang B, Chen L-Q. Phase-field-guided design of record-high piezoelectricity and discovery of simultaneous high light transparency and high piezoelectricity in relaxor ferroelectrics. *MRS Bull* 2024, **49**: 626-35.

[22] Li F, Wang B, Gao XY*, et al.* Ferroelectric materials toward next-generation electromechanical technologies. *Science* 2025, **389**: eadn4926.

[23] Xi GY, Lin SS, Shen TJ*, et al.* Transparent Ceramic@Sapphire Composites for High-Power Laser-Driven Lighting. *Adv Sci* 2025, **12**: e2505232.

[24] Xi GY, Zhou ZZ, Li J*, et al.* Transparent Composite Ceramic@aluminum with Ultra-High Thermal Conductivity for High-Brightness Laser-Driven Lighting. *Adv Funct Mater* 2024, **34**: 2401026.

[25] Liu GC, Chen WB, Xiong Z*, et al.* Laser-driven broadband near-infrared light source with watt-level output. *Nat Photonics* 2024, **18**: 562-8.

[26] Ha MY, Kim J, Lee J*, et al.* A handheld photoacoustic microscopic probe integrating a transparent ultrasound transducer and a fiber scanner. *Nat Commun* 2025, **17**: 1409.

[27] Milisavljevic I, Zhang M, Jiang QH*, et al.* Transparent electro-optic ceramics: Processing, materials, and applications. *J Materiomics* 2025, **11**: 100872.

[28] Lin JF, Wang Y, Xiong R*, et al.* Tailoring micro-structure of eco-friendly temperature-insensitive transparent ceramics achieving superior piezoelectricity. *Acta Mater* 2022, **235**: 118061.

[29] Huang C, Xu JM, Fang Z*, et al.* Effect of preparation process on properties of PLZT (9/65/35) transparent ceramics. *J Alloys Compd* 2017, **723**: 602-10.

[30] Hu M, Wu Y, Chen L*, et al.* Effects of rare earth dopants on the EO properties and domain configurations in PMN-PT transparent ceramics. *J Mater Sci: Mater Electron* 2024, **35**: 656.

[31] Ishitobi Y, Shimada M, Koizumi M. Fabrication of Translucent Pb $(Zr_{0.8}Ti_{0.2})O_3$ Ceramics by Isostatic Hot-Pressing. *J Am Ceram Soc* 1974, **57**: 458-.

[32] Li GR, Ruan W, Zeng JT*, et al.* The effect of domain structures on the transparency of PMN–PT Transparent Ceramics. *Opt Mater* 2013, **35**: 722-6.

[33] Ren XD, Peng ZH, Chen B*, et al.* A compromise between piezoelectricity and transparency in KNN-based ceramics: The dual functions of Li_2O addition. *J Eur Ceram Soc* 2020, **40**: 2331-7.

[34] De Greve K, Yu L, McMahon PL*, et al.* Quantum-dot spin-photon entanglement via frequency downconversion to telecom wavelength. *Nature* 2012, **491**: 421-5.

[35] Cai L, Kang Y, Hu H. Electric-optical property of the proton exchanged phase modulator in single-crystal lithium niobate thin film. *Opt Express* 2016, **24**: 4640-7.

[36] Chiles J, Fathpour S. Mid-infrared integrated waveguide modulators based on silicon-on-lithium-niobate photonics. *Optica* 2014, **1**: 350.

[37] Liu X, Tan P, Ma X*, et al.* Ferroelectric crystals with giant electro-optic property enabling

ultracompact Q-switches. *Science* 2022, **376**: 371-7.

[38] Yang ZT, Du HL, Qu SB*, et al.* Significantly enhanced recoverable energy storage density in potassium–sodium niobate-based lead free ceramics. *J Mater Chem A* 2016, **4**: 13778-85.

[39] Yang ZT, Du HL, Jin L*, et al.* High-performance lead-free bulk ceramics for electrical energy storage applications: design strategies and challenges. *J Mater Chem A* 2021, **9**: 18026-85.

[40] Dai ZH, Li DY, Zhou ZJ*, et al.* A strategy for high performance of energy storage and transparency in KNN-based ferroelectric ceramics. *Chem Eng J* 2022, **427**: 131959.

[41] Liu CX, Dai ZH, Zheng YY*, et al.* Transparent KNN-based ceramics for energy storage: A Review. *Chem Eng J* 2026, **538**: 176745.

[42] Chen XY, Chen RM, Chen ZY*, et al.* Transparent Lead lanthanum zirconate titanate (PLZT) ceramic fibers for High-frequency Ultrasonic Transducer Applications. *Ceram Int* 2016, **42**: 18554-9.

[43] Chen HY, Mirg S, Osman M*, et al.* A High Sensitivity Transparent Ultrasound Transducer based on PMN-PT for Ultrasound and Photoacoustic Imaging. *IEEE Sens Lett* 2021, **5**: 1-4.

[44] Thalhammer G, McDougall C, MacDonald MP*, et al.* Acoustic force mapping in a hybrid acoustic-optical micromanipulation device supporting high resolution optical imaging. *Lab Chip* 2016, **16**: 1523-32.

[45] Wang LV. Multiscale photoacoustic microscopy and computed tomography. *Nat Photonics* 2009, **3**: 503-9.

[46] Park J, Park B, Kim HH*, et al.* Versatile Optical and Ultrasound Imaging Platforms using Transparent Ultrasound Transducers. Optical Tomography and Spectroscopy: Optica Publishing Group; 2022. p. OM2D. .

[47] Park B, Han M, Park J*, et al.* A photoacoustic finder fully integrated with a solid-state dye laser and transparent ultrasound transducer. *Photoacoustics* 2021, **23**: 100290.

[48] Chen HY, Osman M, Mirg S*, et al.* Transparent ultrasound transducers for multiscale photoacoustic imaging. Photons Plus Ultrasound: Imaging and Sensing; 2021. p. 142.

[49] Park J, Park B, Kim TY, *et al.* Quadruple ultrasound, photoacoustic, optical coherence, and fluorescence fusion imaging with a transparent ultrasound transducer. *Proc Natl Acad Sci U S A* 2021, **118**: e1920879118.

[50] Yu FY, Wang P, Lin JF, *et al.* $(K_{0.5}Na_{0.5})NbO_3$-based photochromic transparent ceramics for high-security dynamic anti-counterfeiting and optical storage applications. *J Lumin* 2022, **252**: 119345.

[51] Lin JF, Zhou Y, Lu QL, *et al.* Reversible modulation of photoenergy in Sm-doped $(K_{0.5}Na_{0.5})NbO_3$ transparent ceramics via photochromic behavior. *J Mater Chem A* 2019, **7**: 19374-84.

[52] Wang YQ, Guo PK, Wang YN, *et al.* Enhancement of the photoluminescence modulation ratio in highly transparent KNN-based ceramics for optical information storage. *J Mater Chem C* 2023, **11**: 4775-83.

[53] Jia QN, Zhang QW, Sun HQ, *et al.* High transmittance and optical storage behaviors in Tb^{3+} doped $K_{0.5}Na_{0.5}NbO_3$-based ferroelectric materials. *J Eur Ceram Soc* 2021, **41**: 1211-20.

[54] Zeng XF, Jiang XG, Lin JF, *et al.* Excellent low-E energy storage and fluorescence temperature sensing features in $Bi_{0.5}Na_{0.5}TiO_3$-based transparent ceramics. *Chem Eng J* 2024, **496**: 154150.

[55] Zeng XF, Lin JF, Dong GL, *et al.* Polymorphic relaxor phase and defect dipole polarization co-reinforced capacitor energy storage in temperature-monitorable high-entropy ferroelectrics. *Nat Commun* 2025, **16**: 1870.

[56] Zeng XF, Zhang YD, Shen J, *et al.* Superior Temperature Sensing and Capacitive Energy-Storage Performance in Pb-Free Ceramics. *Small* 2025, **21**: e2406080.

[57] Shi GQ, Wang YQ, Sang MH, *et al.* Investigating the temperature-dependent electro-optic behaviors in La-doped PMN-PT transparent ceramics. *Appl Phys Lett* 2025, **126**: 241903.

[58] Hu M, Chang ZC, Nie N, *et al.* La-doped PMN–PT transparent ceramics with ultra-high electro-optic effect and its application in optical devices. *J Adv Ceram* 2023, **12**: 1441-53.

[59] Jiang H, Zou YK, Chen Q*, et al.* Transparent electro-optic ceramics and devices. Optoelectronic Devices and Integration 2005.

[60] Yan PK, Qin YL, Xu ZY*, et al.* Highly Transparent Eu-Doped 0.72PMN-0.28PT Ceramics with Excellent Piezoelectricity. *ACS Appl Mater Interfaces* 2021, **13**: 54210-6.

[61] Guo PK, Gao W, Lin RQ*, et al.* Advancement in PMN-PT transparent piezoelectric ceramic for photoacoustic/ultrasound dual-mode imaging. *J Materiomics* 2025, **11**: 100932.

[62] Tang H, Zhang MF, Zhang SJ*, et al.* Investigation of dielectric and piezoelectric properties in $Pb(Ni_{1/3}Nb_{2/3})O_3$–$PbHfO_3$–$PbTiO_3$ ternary system. *J Eur Ceram Soc* 2013, **33**: 2491-7.

[63] Gao W, Wang XT, Zhang JM*, et al.* Achieving coaxial photoacoustic/ultrasound dual-modality imaging by high-performance Sm: 0.72PMN-0.28PT transparent piezoelectric ceramic. *Nano Energy* 2024, **132**: 110390.

[64] Zheng FJ, Tian X, Fang Z*, et al.* Sm-Doped PIN-PMN-PT Transparent Ceramics with High Curie Temperature, Good Piezoelectricity, and Excellent Electro-Optical Properties. *ACS Appl Mater Interfaces* 2023, **15**: 7053-62.

[65] Zeng JT, Ling ZQ, Zhao KY*, et al.* Origin of the high piezoelectric and optical properties of Pr-PMN-PT100*x*/70/30 transparent ceramics. *J Alloys Compd* 2024, **984**: 173847.

[66] Li CC, Xu B, Lin DB*, et al.* Atomic-scale origin of ultrahigh piezoelectricity in samarium-doped PMN-PT ceramics. *Physical Review B* 2020, **101**: 140102.

[67] Wu JG, Xiao DQ, Zhu JG. Potassium-sodium niobate lead-free piezoelectric materials: past, present, and future of phase boundaries. *Chem Rev* 2015, **115**: 2559-95.

[68] Lv X, Zhu JG, Xiao DQ*, et al.* Emerging new phase boundary in potassium sodium-niobate based ceramics. *Chem Soc Rev* 2020, **49**: 671-707.

[69] Rahman A, Jiang MH, Rao GH*, et al.* Improved ferroelectric, piezoelectric, and dielectric properties in pure KNN translucent ceramics by optimizing the normal sintering method. *Ceram Int* 2022, **48**: 20251-9.

[70] Kwok KW, Li FL, Lin DM. A Novel Lead-Free Transparent Ceramic with High Electro-Optic Coefficient. *Funct Mater Lett* 2012, **04**: 237-40.

[71] Li FL, Kwok KW. Fabrication of transparent electro-optic $(K_{0.5}Na_{0.5})_{1-x}Li_xNb_{1-x}Bi_xO_3$ lead-free ceramics. *J Eur Ceram Soc* 2013, **33**: 123-30.

[72] Lin JF, Wang P, Wang HJ, *et al.* Significantly Photo-Thermochromic KNN-Based "Smart Window" for Sustainable Optical Data Storage and Anti-Counterfeiting. *Adv Opt Mater* 2021, **9**: 2100580.

[73] Qin YL, Yan PK, Han FX, *et al.* The piezoelectric properties of transparent $0.75Pb(Mg_{1/3}Nb_{2/3})O_3$-$0.25PbTiO_3$:$Pr^{3+}$ ceramics. *J Alloys Compd* 2022, **891**: 161959.

[74] Chen YJ, Sun DZ, Zhu YY, *et al.* The effect of Sn^{4+} doping on the electrostrictive property of PLZT (9/65/35) transparent electro-optical ceramics. *Ceram Int* 2020, **46**: 6738-44.

[75] Dupuy AD, Kodera Y, Garay JE. Unprecedented Electro-Optic Performance in Lead-Free Transparent Ceramics. *Adv Mater* 2016, **28**: 7970-7.

[76] Yan K, Chen XL, Wang FF, *et al.* Large piezoelectricity and high transparency in fine-grained $BaTiO_3$ ceramics. *Appl Phys Lett* 2020, **116**: 082902.

[77] Luo WX, Wu MX, Han YF, *et al.* Enhanced optical transmittance and energy-storage performance in $NaNbO_3$-modified $Bi_{0.5}Na_{0.5}TiO_3$ ceramics. *J Am Ceram Soc* 2023, **106**: 4723-31.

[78] Luo W, Ma P, Xie TF, *et al.* Fabrication and spectroscopic properties of Co:$MgAl_2O_4$ transparent ceramics by the HIP post-treatment. *Opt Mater* 2017, **69**: 152-7.

[79] Wang SF, Zhang J, Luo DW, *et al.* Transparent ceramics: Processing, materials and applications. *Prog Solid State Chem* 2013, **41**: 20-54.

[80] Penilla EH, Hardin CL, Kodera Y, *et al.* The role of scattering and absorption on the optical properties of birefringent polycrystalline ceramics: Modeling and experiments on ruby (Cr:Al_2O_3). *J Appl Phys* 2016, **119**: 023106.

[81] Goldstein A, Krell A, Kleebe A. Transparent Ceramics at 50: Progress Made and Further

Prospects. *J Am Ceram Soc* 2016, **99**: 3173-97.

[82] Kuna L, Mangeri J, Gorzkowski EP*, et al.* Mesoscale modeling of light transmission modulation in ceramics. *Acta Mater* 2020, **193**: 261-9.

[83] Zhao XM, Fang QL, Xia CJ*, et al.* Evaluation of pore scattering in transparent ceramics: A simplified model for nanometric spherical pores. *J Am Ceram Soc* 2022, **106**: 527-37.

[84] Apetz R, van Bruggen MPB. Transparent Alumina: A Light-Scattering Model. *J Am Ceram Soc* 2003, **86**: 480-6.

[85] Hulst HC, van de Hulst HC. Light scattering by small particles: Courier Corporation; 1981.

[86] Zhao XM, Chao XL, Wu D*, et al.* Evaluation of birefringence contribution to transparency in (1-*x*)KNN-*x*Sr($Al_{0.5}Ta_{0.5}$)O_3 ceramics: A phase structure tailoring. *J Alloys Compd* 2019, **798**: 669-77.

[87] Peelen JGJ, Metselaar R. Light scattering by pores in polycrystalline materials: Transmission properties of alumina. *J Appl Phys* 1974, **45**: 216-20.

[88] Bohren CF, Huffman DR. Absorption and scattering of light by small particles: John Wiley & Sons; 2008.

[89] Xiong ZX, Zhu J, Ma JX*, et al.* Domain wall scattering determining the transmittance of transparent ferroelectric crystals. *Appl Phys Lett* 2025, **126**: 191901.

[90] Li K, Sun EW, Zhang YC*, et al.* High piezoelectricity of Eu^{3+}-doped $Pb(Mg_{1/3}Nb_{2/3})O_3$–$0.25PbTiO_3$ transparent ceramics. *J Mater Chem C* 2021, **9**: 2426-36.

[91] Koizumi M, Kodaira K, Ishitobi Y*, et al.* Fabrication of translucent ceramics by isostatic hot-pressing. *Ceramurgia Int* 1976, **2**: 67-71.

[92] Alberta EF, Bhalla AS. Piezoelectric and dielectric properties of transparent Pb $(Ni_{1/3}Nb_{2/3})_{1-x-y}Zr_xTi_yO_3$ ceramics prepared by hot isostatic pressing. *Int J Inorg Mater* 2001, **3**: 987-95.

[93] Ishitobi Y, Shimada M, Koizumi M. Fabrication of Translucent Pb (Zr0. 8Ti0. 2) O3 Ceramics by Isostatic Hot-Pressing. *J Am Ceram Soc* 1974, **57**: 458-.

[94] Li K, Li FL, Wang Y*, et al.* Hot-pressed $K_{0.48}Na_{0.52}Nb_{1-x}Bi_xO_3$ (x=0.05–0.15) lead-free ceramics

for electro-optic applications. *Mater Chem Phys* 2011, **131**: 320-4.

[95] Li FL, Kwok KW, Gupta S. $K_{0.5}Na_{0.5}NbO_3$-Based Lead-Free Transparent Electro-Optic Ceramics Prepared by Pressureless Sintering. *J Am Ceram Soc* 2013, **96**: 3557-62.

[96] Wu YJ, Li J, Chen XM*, et al.* Effects of La2O3 Addition and PbO Excess on the Transmittance of $PbZrO_3$–PbTiO3–$Pb(Zn_{1/3}Nb_{2/3})$O3 Ceramics by Spark Plasma Sintering. *J Am Ceram Soc* 2007, **91**: 13-6.

[97] Wu YJ, Li J, Kimura R*, et al.* Effects of Preparation Conditions on the Structural and Optical Properties of Spark Plasma-Sintered PLZT (8/65/35) Ceramics. *J Am Ceram Soc* 2005, **88**: 3327-31.

[98] Londoño F, do Nascimento WJ, Viana DSF*, et al.* Novel insights into PLMN-13PT ceramics: impact of spark plasma sintering on compositional and dielectric properties. *Emergent Mater* 2024, **8**: 905-12.

[99] Fujii I, Yoshida R, Imai T*, et al.* Fabrication of Transparent $Pb(Mg_{1/3}Nb_{2/3})O_3$–$PbTiO_3$ Based Ceramics by Conventional Sintering. *J Am Ceram Soc* 2013, **96**: 3782-7.

[100] Chen X, Chen S, Clequin P-M*, et al.* Combustion synthesis of lead oxide nanopowders for the preparation of PMN–PT transparent ceramics. *Ceram Int* 2015, **41**: 755-60.

[101] Chen X, Chen S, Bruner A*, et al.* Effects of dopants on the microstructure and phase-purity control in PMN-PT ceramics. *Ceram Int* 2018, **44**: 17909-13.

[102] Zeng JT, Wei ZH, Huang YL*, et al.* NIR to Visible Up-conversion Luminescence of Er^{3+}-Doped PMN-PT Transparent Ceramics. *J Am Ceram Soc* 2012, **95**: 2573-8.

[103] Wei ZH, Tsuboi T, Nakai Y*, et al.* The synthesis of Er^{3+}-doped PMN–PT transparent ceramic and its infrared luminescence. *Mater Lett* 2012, **68**: 57-9.

[104] Song ZZ, Zhang YC, Lu CJ*, et al.* Fabrication and ferroelectric/dielectric properties of La-doped PMN-PT ceramics with high optical transmittance. *Ceram Int* 2017, **43**: 3720-5.

[105] Gao W, Wang YQ, Tian X*, et al.* Significantly enhanced piezoelectric properties in PMN-PT transparent ceramics by Sm/Pr co-doping. *J Alloys Compd* 2025, **1010**: 177640.

[106] Zhao XM, Chao XL, Wu D*, et al.* Simultaneous realization of high transparency and piezoelectricity in low symmetry KNN-based ceramics. *J Am Ceram Soc* 2018, **102**: 3498-509.

[107] Zhao XM, Chai QZ, Chen B*, et al.* Improved transmittance and ferroelectric properties realized in KNN ceramics via SAN modification. *J Am Ceram Soc* 2018, **101**: 5127-37.

[108] Zhou Y, Wang P, Lin JF*, et al.* High-contrast photochromic Eu-doped $K_{0.5}Na_{0.5}NbO_3$ ceramics with prominent pellucidity. *Dalton Trans* 2021, **50**: 4914-22.

[109] Lin JF, Zhai JW, Wu X*, et al.* Simultaneously improved transparency, photochromic contrast and Curie temperatureviarare-earth ion modification in KNN-based ceramics. *Inorg Chem Front* 2021, **8**: 2027-35.

[110] Lin JF, Zhai JW, Wu X*, et al.* Expedient Red Emitting and Transparency Dual Modulation in KNN-Based Transparent Ceramics via Sensitive Photothermochromic Behavior. *ACS Appl Electron Mater* 2021, **3**: 1394-402.

[111] Wu X, Yu FY, Xiong RX*, et al.* How to Realize Ultrahigh Photochromic Performance for Real-Time Optical Recording in Transparent Ceramics. *ACS Appl Mater Interfaces* 2023, **15**: 16828-41.

[112] Zhou YB, Zhao KY, Ruan W*, et al.* Electric Field-Induced Light Scattering in Eu-Doped PMN-PT Transparent Ceramics. *J Am Ceram Soc* 2016, **99**: 3993-9.

[113] Ruan W, Li GR, Zeng JT*, et al.* Origin of the giant electro-optic Kerr effect in La-doped 75PMN-25PT transparent ceramics. *J Appl Phys* 2011, **110**: 074109.

[114] Tian X, Fang Z, Zheng FJ*, et al.* Continuous control of polarization state and tunable dual-channel optical communication based on highly transparent PMN-PT electro-optic ceramics. *Ceram Int* 2023, **49**: 23967-74.

[115] Geng ZM, Li K, Shi DL*, et al.* Effect of Sr and Ba-doping in optical and electrical properties of KNN based transparent ceramics. *J Mater Sci: Mater Electron* 2015, **26**: 6769-75.

[116] Wu X, Lu SB, Kwok KW. Photoluminescence, electro-optic response and piezoelectric properties in pressureless-sintered Er-doped KNN-based transparent ceramics. *J Alloys Compd* 2017,

695: 3573-8.

[117] Zeng X, Ding AL, Zheng XS*, et al.* Effects of excess ZnO addition on La-doped PZN–PZT ceramics prepared by hot pressing. *Ceram Int* 2007, **33**: 883-5.

[118] Deng GC, Ding AL, Zeng X*, et al.* Optical and Piezoelectric Properties of Transparent PZN-PLZT Ceramics. *Integr Ferroelectr* 2011, **80**: 125-32.

[119] Yin QR, Ding AL, Zheng XS*, et al.* Preparation and characterization of transparent PZN–PLZT ceramics. *J Mater Res* 2004, **19**: 729-32.

[120] Londono FA, Eiras JA, Garcia D. Optical and electro-optical characteristics of hot-pressing $(Pb_{1-x}La_x)TiO_3$ ferroelectric ceramics. *Bol Soc Esp Ceram Vidrio* 2012, **51**: 353-8.

[121] Kong LB, Ma J, Zhu W*, et al.* Translucent PMN and PMN-PT ceramics from high-energy ball milling derived powders. *Mater Res Bull* 2002, **37**: 23-32.

[122] Bartscherer E, Braun A, Wolff M*, et al.* Improved preparation of transparent PLZT ceramics by electrophoretic deposition and hot isostatic pressing. 27th annual cocoa beach conference on advanced ceramics and composites: B: Ceramic engineering and science proceedings: Wiley Online Library; 2003. p. 169-74.

[123] Huang HQ, Yu FY, Zhang YD*, et al.* Defect engineering by annealing: Managing the trade-off relationship between photochromic and electrical properties in KNN-based translucent ceramics. *J Alloys Compd* 2024, **1005**: 176010.

[124] Qiu CR, Zhang ZQ, Xu ZQ*, et al.* Transparent ultrasonic transducers based on relaxor ferroelectric crystals for advanced photoacoustic imaging. *Nat Commun* 2024, **15**: 10580.

[125] Gao XY, Qiao L, Qiu CR*, et al.* A robust, low-voltage driven millirobot based on transparent ferroelectric crystals. *Appl Phys Lett* 2022, **120**: 032902.

[126] Liu Y-H, Lin F-S, Chen L-X*, et al.* Wearable transparent PVDF transducer for photoacoustic imager in body sensor network. 2020 IEEE International Ultrasonics Symposium (IUS): IEEE; 2020. p. 1-3.

[127] Li F, Lin DB, Chen ZB, *et al.* Ultrahigh piezoelectricity in ferroelectric ceramics by design. *Nat Mater* 2018, **17**: 349-54.

[128] Qiu CR, Wang B, Zhang N, *et al.* Transparent ferroelectric crystals with ultrahigh piezoelectricity. *Nature* 2020, **577**: 350-4.

[129] Guo QH, Hou LT, Li F, *et al.* Investigation of dielectric and piezoelectric properties in aliovalent Eu^{3+}-modified $Pb(Mg_{1/3}Nb_{2/3})O_3$-$PbTiO_3$ ceramics. *J Am Ceram Soc* 2019, **102**: 7428-35.

[130] Yu H-L, Kang W-S, Lee J-H, *et al.* Transparent high-performance piezoceramics through pressureless sintering. *J Adv Ceram* 2024, **13**: 561-7.

[131] Qi Y, Wang YQ, Fu DS, *et al.* High piezoelectricity of Sm-doping PIN-PMN-PT transparent ceramics and its potential application in transparent transducers. *Ceram Int* 2025, **51**: 39319-27.

[132] Jiang QH, Zhao WG, Zhang M, *et al.* Dynamic Atomistic Polar Structure Underpins Ultrahigh Linear Electro-Optic Coefficient in Transparent Ferroelectric Ceramics. *JACS* 2025, **147**: 42909-17.

[133] Fan HL, Luo ZH, Meng YZ, *et al.* Synergistic enhancement of Curie temperature and piezoelectric properties in PIN–PMN–PT transparent ceramics. *J Am Ceram Soc* 2025: e70274.

[134] Yuan M, Fu DS, Wang YQ, *et al.* Enhancing the performance of PMN-PT transparent piezoelectric ceramics by multi-rare earth doping based on the high-entropy strategy. *Ceram Int* 2026, **52**: 12726-34.

[135] Zhu L, Li CW, Wang YQ, *et al.* Transparent Eu-PIN-PMN-PT piezoelectric ceramics with high curie temperature and superior thermal stability. *J Alloys Compd* 2026, **1065**: 188133.

[136] Yang D, Ma C, Yang ZP, *et al.* Optical and electrical properties of pressureless sintered transparent $(K_{0.37}Na_{0.63})NbO_3$-based ceramics. *Ceram Int* 2016, **42**: 4648-57.

[137] Deng DJ, Irshad MS, Kong X, *et al.* Potassium sodium niobate-based transparent ceramics with high piezoelectricity and enhanced energy storage density. *J Alloys Compd* 2023, **953**: 170081.

[138] Chen Y, Zhang DL, Luo HF, *et al.* 3D printed Er^{3+} doped KNNLN piezoelectric ceramics for transparent ultrasonic transducer application. *Ceram Int* 2024, **50**: 9979-84.

[139] Lin QF, Zeng XF, Huang X, *et al.* Multiscale reconfiguration achieving high electromechanical performance in $K_{0.5}Na_{0.5}NbO_3$-based transparent ceramics for pressure-warning smart window. *Chem Eng J* 2025, **520**: 165886.

[140] Lin QF, Shen J, Zeng XF, *et al.* Breaking the Transparency-Piezoelectricity Trade-Off in Lead-Free Ceramics via Tailoring Local Polarization Configuration. *ACS Nano* 2026.

[141] Guo PK, Wang YN, Zhu L, *et al.* Effect of DC poling on transparency and photoluminescence in Pr:PMN-PT transparent ceramics. *J Alloys Compd* 2024, **994**: 174739.

[142] Wang YQ, Wang YN, Yan PK, *et al.* Determining AC polarization conditions of ferroelectric materials by dynamic scaling method. *Appl Phys Express* 2023, **16**: 011003.

[143] Li DF, Gu W, Irshad MS, *et al.* Simultaneously achieving high transparency and applicable piezoelectricity in Sm-modified KNN-based lead-free ceramics. *J Alloys Compd* 2023, **955**: 170209.

[144] Lv YG, Wang CL, Zhang JL, *et al.* Tantalum influence on physical properties of $(K_{0.5}Na_{0.5})(Nb_{1-x}Ta_x)O_3$ ceramics. *Mater Res Bull* 2009, **44**: 284-7.

[145] Zuo RZ, Fu J, Lv DY, *et al.* Antimony Tuned Rhombohedral-Orthorhombic Phase Transition and Enhanced Piezoelectric Properties in Sodium Potassium Niobate. *J Am Ceram Soc* 2010, **93**: 2783-7.

[146] Wang RP, Bando H, Kidate M, *et al.* Effects of A-Site Ions on the Phase Transition Temperatures and Dielectric Properties of $(1-x)(Na_{0.5}K_{0.5})NbO_3$–$xAZrO_3$ Solid Solutions. *Jpn J Appl Phys* 2011, **50**: 09nd10.

[147] Matsuura Y, Hirano T, Sakai K. Friction torque reduction by ultrasonic vibration and its application to electromagnetically spinning viscometer. *Jpn J Appl Phys* 2014, **53**: 07kc12.

[148] Wu B, Wu HJ, Wu JG, *et al.* Giant Piezoelectricity and High Curie Temperature in Nanostructured Alkali Niobate Lead-Free Piezoceramics through Phase Coexistence. *J Am Chem Soc* 2016, **138**: 15459-64.

[149] Ren PR, Liu ZC, Wei MY, *et al.* Temperature-insensitive dielectric and piezoelectric properties

in (1-*x*)$K_{0.5}Na_{0.5}Nb_{0.997}Cu_{0.0075}O_3$-*x*$SrZrO_3$ ceramics. *J Eur Ceram Soc* 2017, **37**: 2091-7.

[150] Haertling GH. Ferroelectric ceramics: history and technology. *J Am Ceram Soc* 1999, **82**: 797-818.

[151] Gao M, Ye Q, Dong ZR*, et al.* Beam steering of external cavity diode laser by an intracavity electro-optic ceramic deflector. *Chinese Optics Letters* 2011, **9**: 081406.

[152] Zhang F, Chou H-H, Crossland WA. PLZT-Based Shutters for Free-Space Optical Fiber Switching. *IEEE Photonics J* 2016, **8**: 1-12.

[153] Uchino K. Electro-optic ceramics and their display applications. *Ceram Int* 1995, **21**: 309-15.

[154] Ruan W, Li GR, Zeng JT*, et al.* Large Electro-Optic Effect in La-Doped 0.75Pb($Mg_{1/3}Nb_{2/3}$)O_3–0.25$PbTiO_3$ Transparent Ceramic by Two-Stage Sintering. *J Am Ceram Soc* 2010, **93**: 2128-31.

[155] Londoño FA, Eiras J, Milton FP*, et al.* Preparation and Microstructural, Structural, Optical and Electro-Optical Properties of La Doped PMN-PT Transparent Ceramics. *Optics and Photonics Journal* 2012, **02**: 157-62.

[156] Ji WL, He XY, Cheng WX*, et al.* Influences of Excess PbO on Optical Properties and Microstructures of La Modified 0.75Pb ($Mg_{1/3}Nb_{2/3}$)O_3-0.25$PbTiO_3$ Electro-Optic Transparent Ceramics. *Mater Sci Forum* 2013, **745-746**: 555-9.

[157] Ji WL, He XY, Cheng WX*, et al.* Effect of La content on dielectric, ferroelectric and electro-optic properties of Pb($Mg_{1/3}Nb_{2/3}$)O_3–$PbTiO_3$ transparent ceramics. *Ceram Int* 2015, **41**: 1950-6.

[158] Fujii I, Nakashima S, Wada T. Fabrication and electro-optic properties of 0.9Pb[$(Mg,Zn)_{1/3}Nb_{2/3}$]O_3–0.1$PbTiO_3$ transparent ceramics by a conventional sintering technique. *Jpn J Appl Phys* 2017, **56**: 10pc04.

[159] Jiang LJ, Cheng HJ, Sun DZ*, et al.* Effects of Ba^{2+}doping on microstructure and properties of PLMNT electro-optic ceramics fabricated by hot-pressed sintering process. *Ceram Int* 2022, **48**: 35259-66.

[160] Kroupa J, Petzelt J, Malic B*, et al.* Electro-optic properties of KNN–STO lead-free ceramics. *J Phys D: Appl Phys* 2005, **38**: 679-81.

[161] Liu ZY, Fan HQ, Peng BL. Enhancement of optical transparency in Bi_2O_3-modified $(K_{0.5}Na_{0.5})_{0.9}Sr_{0.1}Nb_{0.9}Ti_{0.1}O_3$ ceramics for electro-optic applications. *J Mater Sci* 2015, **50**: 7958-66.

[162] Chai QZ, Zhang FD, Zhou QY*, et al.* Superior Energy Storage Properties and Optical Transparency in $K_{0.5}Na_{0.5}NbO_3$ -Based Dielectric Ceramics via Multiple Synergistic Strategies. *Small* 2023, **19**: e2207464.

[163] Qu BY, Du HL, Yang ZT. Lead-free relaxor ferroelectric ceramics with high optical transparency and energy storage ability. *J Mater Chem C* 2016, **4**: 1795-803.

[164] Chai QZ, Yang D, Zhao XM*, et al.* Lead-free (K,Na)NbO_3-based ceramics with high optical transparency and large energy storage ability. *J Am Ceram Soc* 2018, **101**: 2321-9.

[165] Xing J, Huang YL, Wu B*, et al.* Energy Storage Behavior in $ErBiO_3$-Doped (K,Na)NbO_3 Lead-Free Piezoelectric Ceramics. *ACS Appl Electron Mater* 2020, **2**: 3717-27.

[166] Zhang M, Yang HB, Li D*, et al.* Excellent energy density and power density achieved in $K_{0.5}Na_{0.5}NbO_3$-based ceramics with high optical transparency. *J Alloys Compd* 2020, **829**: 154565.

[167] Ren XD, Jin L, Peng ZH*, et al.* Regulation of energy density and efficiency in transparent ceramics by grain refinement. *Chem Eng J* 2020, **390**: 124566.

[168] Xing J, Huang YL, Xu Q*, et al.* Realizing High Comprehensive Energy Storage and Ultrahigh Hardness in Lead-Free Ceramics. *ACS Appl Mater Interfaces* 2021, **13**: 28472-83.

[169] Li CX, Huan Y, Wang XZ*, et al.* Amelioration on energy storage performance of KNN-based transparent ceramics by optimizing the polarization and breakdown strength. *J Am Ceram Soc* 2022, **105**: 6158-67.

[170] Lin JF, Ge GL, Zhu K*, et al.* Simultaneously achieving high performance of energy storage and transparency via A-site non-stoichiometric defect engineering in KNN-based ceramics. *Chem Eng J* 2022, **444**: 136538.

[171] Hou J, Dai ZH, Liu CX, *et al.* Enhanced photoelectric properties for $BiZn_{0.5}Zr_{0.5}O_3$ modified KNN-based lead-free ceramics. *J Alloys Compd* 2023, **960**: 170639.

[172] Chai QZ, Peng ZH, Wu D, *et al.* Significant improvement of comprehensive energy storage performance and transparency in $Sr_{0.7}La_{0.2}TiO_3$-doped $(K,Na)NbO_3$ lead-free ceramics. *J Alloys Compd* 2023, **968**: 171908.

[173] Sun ZX, Zhao SB, Wang T, *et al.* Achieving high overall energy storage performance of KNN-based transparent ceramics by ingenious multiscale designing. *J Mater Chem A* 2024, **12**: 16735-47.

[174] Bi WJ, Li Y, Du J, *et al.* Superior energy storage performance and transparency in $(K_{0.5}Na_{0.5})(Nb_{0.97}Ta_{0.03})O_3$-based ceramics. *J Mater Chem C* 2024, **12**: 17439-47.

[175] Song JW, Jiang MH, Ouyang YJ, *et al.* Transparency and energy-storage characteristics of potassium tantalate niobate relaxorferroelectric ceramics. *Ceram Int* 2025, **51**: 3864-73.

[176] Bi WJ, Li Y, Tian G, *et al.* Energy storage properties, transmittance and hardness of Er doped $K_{0.5}Na_{0.5}NbO_3$-based ceramics. *J Eur Ceram Soc* 2025, **45**: 116851.

[177] Gong ZC, Yue HJ, Fang KL, *et al.* Multifunctional energy storage and photoluminescence of Er-modified KNN-based transparent ferroelectric ceramics. *J Materiomics* 2025, **11**: 100993.

[178] Sun ZX, Zhao SB, Wang ZY, *et al.* Significantly improving the energy storage capability of transparent ceramics via a voltage endurance double enhancement strategy. *Chem Eng J* 2025, **504**: 158943.

[179] Yang YL, Liu ZY, Gao LL, *et al.* Mediating the Confliction of Energy Storage Performance and Transparency in KNN-Based Ceramics via Synergistic Optimization Strategy. *ACS Appl Mater Interfaces* 2025, **17**: 22963-73.

[180] Wang F, Han Y, Lim CS, *et al.* Simultaneous phase and size control of upconversion nanocrystals through lanthanide doping. *Nature* 2010, **463**: 1061-5.

[181] Hao JH, Zhang Y, Wei XH. Electric-Induced Enhancement and Modulation of Upconversion Photoluminescence in Epitaxial $BaTiO_3$:Yb/Er Thin Films. *Angewandte Chemie* 2011, **123**: 7008-12.

[182] Wang HQ, Batentschuk M, Osvet A, *et al.* Rare-earth ion doped up-conversion materials for photovoltaic applications. *Adv Mater* 2011, **23**: 2675-80.

[183] Lv ZL, Qin YL, Zhang YC, *et al.* Efficient upconversion photoluminescence in transparent Pr^{3+}/Yb^{3+} co-doped $0.75Pb(Mg_{1/3}Nb_{2/3})O_3$–$0.25PbTiO_3$ ferroelectric ceramics. *Ceram Int* 2019, **45**: 10924-9.

[184] Zheng M, Li X-Y, Ni H, *et al.* van der Waals epitaxy for highly tunable all-inorganic transparent flexible ferroelectric luminescent films. *J Mater Chem C* 2019, **7**: 8310-5.

[185] Qin YL, Han FX, Yan PK, *et al.* Fluorescence intensity ratio (FIR) analysis of the temperature sensing properties in transparent ferroelectric PMN-PT:Pr^{3+} ceramic. *Ceram Int* 2021, **47**: 24092-7.

[186] Wei ZH, Huang YL, Tsuboi TJ, *et al.* Optical characteristics of Er^{3+}-doped PMN–PT transparent ceramics. *Ceram Int* 2012, **38**: 3397-402.

[187] Liang Z, Sun EW, Liu ZY, *et al.* Electric field induced upconversion fluorescence enhancement and its mechanism in Er^{3+} doped $0.75Pb(Mg_{1/3}Nb_{2/3})O_3$-$0.25PbTiO_3$ transparent ceramic. *Appl Phys Lett* 2016, **109**: 132904.

[188] Yao YJ, Luo LH, Li WP, *et al.* An intuitive method to probe phase structure by upconversion photoluminescence of Er^{3+} doped in ferroelectric $Pb(Mg_{1/3}Nb_{2/3})O_3$-$PbTiO_3$. *Appl Phys Lett* 2015, **106**: 082906.

[189] Shi SY, Wu HT, Liu X, *et al.* Er^{3+}–doped $0.94KNN–0.06Ca(Bi_{0.5}Nb_{0.5})O_3$: a fluorescent transparent ceramic with optoelectronic multi-functionality. *J Mater Sci: Mater Electron* 2023, **34**: 1691.

[190] Zhang Q, Yang ZT, Wang MY, *et al.* A strategy for enhancing luminescence thermometry via Ta^{5+}-triggered $K_{0.5}Na_{0.5}NbO_3$: Er^{3+} transparent ceramics. *J Materiomics* 2024, **10**: 984-94.

[191] Liu H, Yang SQ, Mo XY, *et al.* $K_{0.5}Na_{0.5}NbO_3$-based multifunctional transparent ceramics for ultrahigh sensitive optical thermometry. *J Adv Ceram* 2025, **14**: 9221045.

[192] Wu LJ, Tan Z, Zheng T, *et al.* KNN–Eu transparent ferroelectrics: Local structure and

luminescent property. *J Am Ceram Soc* 2023, **106**: 6664-74.

[193] Ma YM, Yang SX, Zhao CL*, et al.* Photochromic and Electric Field-Regulating Luminescence in High-Transparent (K,Na)NbO_3-Based Ferroelectric Ceramics with Two-Phase Coexistence. *ACS Appl Mater Interfaces* 2022, **14**: 35940-8.

[194] Lin C, Wang HJ, Wang P*, et al.* Smart white lighting and multi-mode optical modulations via photochromism in Dy-doped KNN-based transparent ceramics. *J Am Ceram Soc* 2020, **104**: 903-16.

[195] Wang HJ, Lin JF, Deng BY*, et al.* Reversible multi-mode modulations of optical behavior in photochromic-translucent Nd-doped $K_{0.5}Na_{0.5}NbO_3$ ceramics. *J Mater Chem C* 2020, **8**: 2343-52.

[196] Huang H, Wu LJ, Zheng T*, et al.* Reversible Multimode Luminescence Modulations in Photochromic-Translucent Yb^{3+}/Eu^{3+} Codoped $K_{0.5}Na_{0.5}NbO_3$ Ceramics. *Inorg Chem* 2024, **63**: 2005-14.

[197] Armistead W, Stookey S. Photochromic Silicate Glasses Sensitized by Silver Halides: Their characteristic of changing color reversibly, in combination with other properties, suggests many uses. *Science* 1964, **144**: 150-4.

[198] Zhao HP, Cun YK, Bai X*, et al.* Entirely Reversible Photochromic Glass with High Coloration and Luminescence Contrast for 3D Optical Storage. *ACS Energy Lett* 2022, **7**: 2060-9.

[199] Meng WH, Kragt AJJ, Gao Y*, et al.* Scalable Photochromic Film for Solar Heat and Daylight Management. *Adv Mater* 2024, **36**: e2304910.

[200] Xia D-X, Wang X, Sun W-Q*, et al.* Chameleon-inspired supramolecular materials based on cucurbit[7]uril and viologens exhibiting full-color tunable photochromic behavior. *Chem Eng J* 2024, **484**: 149551.

[201] Zhao HP, Li YW, Mi C*, et al.* NIR regeneration and visible luminescence modification in photochromic glass: A novel encryption and 3D optical storage medium. *InfoMat* 2024, **6**: e12546.

[202] Huang HQ, Zhang S, Yu FY*, et al.* Dy/Sr-codoped $(K_{0.5}Na_{0.5})NbO_3$ multifunctional transparent-ferroelectric ceramics with adjustable white-light emission. *J Am Ceram Soc* 2023, **107**:

1137-47.

[203] Yu FY, Ma BW, Xie ZQ*, et al.* Developing "smart windows" for optical storage and temperature sensing based on KNN transparent ceramics. *J Eur Ceram Soc* 2023, **43**: 4408-18.

[204] Yu FY, Deng LX, Chen Y*, et al.* Sr/Ho-codoped $(K_{0.5}Na_{0.5})NbO_3$ photochromic-transparent ceramics in non-destructive optical data storage and multi-modal anti-counterfeiting. *J Mater Chem C* 2025, **13**: 10321-31.

[205] Yu FY, Chi Y, Wang P*, et al.* Highly responsive photochromic behavior with large coloration contrast in Ba/Sm co-doped $(K_{0.5}Na_{0.5})NbO_3$ transparent ceramics. *Ceram Int* 2022, **48**: 18899-908.

[206] Jia QN, Zhang QW, Sun HQ*, et al.* Multicolor and multimode luminescent modulation via energy transfer engineering in Tb^{3+}/Eu^{3+} co-doped $(K_{0.5}Na_{0.5})NbO_3$ transparent photochromic materials. *J Alloys Compd* 2021, **873**: 159852.

[207] Chen Y, Yu FY, Zhong SQ*, et al.* KNN-based optical temperature sensing ceramics integrating negative thermal quenching and photochromic self-recovery behavior. *J Lumin* 2023, **263**: 120141.

[208] Wang LV, Yao J. A practical guide to photoacoustic tomography in the life sciences. *Nat Methods* 2016, **13**: 627-38.

[209] Piccone A. Robust grasshopper-inspired millirobot operates at low voltages. *Scilight* 2022, **2022**.

[210] Qiao L, Gao XY, Jin HN*, et al.* Ultrahigh focal sensitivity in a relaxor ferroelectric crystal-based piezoelectric adaptive lens. *Appl Phys Lett* 2022, **121**: 082902.

[211] Qiao L, Gao XY, Ren KL*, et al.* Designing transparent piezoelectric metasurfaces for adaptive optics. *Nat Commun* 2024, **15**: 805.

[212] Ren KL, Gao XY, Jin HN*, et al.* Conformal Ordered Solid–Liquid Coupled Piezoelectric Units for Programmable Adaptive Optics. *Adv Funct Mater* 2024, **34**: 2410173.

[213] Lee Y, Choi H, Jang J. Fabrication and characterization of lead lanthanum zirconate titanate ceramic-based fully transparent piezoelectric loudspeakers for next-generation electronic devices.

Sens Actuators, A 2025, **382**: 116087.

[214] Qiao L, Ye Q, Gan JL*, et al.* Optical characteristics of transparent PMNT ceramic and its application at high speed electro-optic switch. *Opt Commun* 2011, **284**: 3886-90.

[215] Zhang X-J, Ye Q, Qu R-H*, et al.* High-power electro-optic switch technology based on novel transparent ceramic. *Chin Phys B* 2016, **25**: 034202.

[216] Huang XJ, Guo QY, Yang DD*, et al.* Reversible 3D laser printing of perovskite quantum dots inside a transparent medium. *Nat Photonics* 2019, **14**: 82-8.

[217] Zhang YQ, Ding YL, Lan F*, et al.* A Photo- and Electrochromic Dual-Responsive Smart Window for Full-Day Photothermal Management. *Small* 2025, **21**: e2501977.

[218] Li XY, Liu M, Shao J*, et al.* High-Capacity Photochromic Rotary Encoder for Information Encryption and Storage. *Adv Funct Mater* 2024, **34**: 2402603.

[219] Xu LH, Lin JF, Yang YX*, et al.* Ultrahigh thermal stability and piezoelectricity of lead-free KNN-based texture piezoceramics. *Nat Commun* 2024, **15**: 9018.

[220] Zou JZ, Wei TX, Song M*, et al.* Unveiling the Origin of Ultrahigh Piezoelectricity in Sb Doped KNN Based Piezoceramics. *Adv Funct Mater* 2025, **35**: 2425080.

[221] Zhu LF, Liu D, Shi XM*, et al.* Ultrahigh piezoelectric performances of (K,Na)NbO_3 based ceramics enabled by structural flexibility and grain orientation. *Nat Commun* 2025, **16**: 901.

[222] Wang HM, Liu LY, Ye PC*, et al.* 3D Printing of Transparent Spinel Ceramics with Transmittance Approaching the Theoretical Limit. *Adv Mater* 2021, **33**: e2007072.

[223] Ma BW, Wu X, Zhao CL*, et al.* An interpretable machine learning strategy for pursuing high piezoelectric coefficients in $(K_{0.5}Na_{0.5})NbO_3$-based ceramics. *npj Comput Mater* 2023, **9**: 229.

[224] Yao YH, Liu H, Hu YH*, et al.* Fluctuating local polarization: a generic fingerprint for enhanced piezoelectricity in Pb-based and Pb-free perovskite ferroelectrics. *Nat Commun* 2025, **16**: 7442.

[225] Li F, Cabral MJ, Xu B*, et al.* Giant piezoelectricity of Sm-doped Pb $(Mg_{1/3}Nb_{2/3})O_3$-$PbTiO_3$ single crystals. *Science* 2019, **364**: 264-8.

[226] Liu JF, Gao XY, Jin HN, *et al.* Miniaturized electromechanical devices with multi-vibration modes achieved by orderly stacked structure with piezoelectric strain units. *Nat Commun* 2022, **13**: 6567.

[227] Kim D, Ha MY, Cho S, *et al.* Fabrication of optically transparent ultrasound transducers to integrate light and sound in multimodal biomedical systems. *Nat Protoc* 2026: 1-20.

[228] Tao H, Wu HJ, Liu Y, *et al.* Ultrahigh Performance in Lead-Free Piezoceramics Utilizing a Relaxor Slush Polar State with Multiphase Coexistence. *J Am Chem Soc* 2019, **141**: 13987-94.

[229] Liu X, Tang MY, Zhang YL, *et al.* High Piezoelectricity and Strong Field Endurance in $Pb(Zr,Ti)O_3$-Rich Textured Ceramics. *Adv Funct Mater* 2025: e15940.

[230] Lin JF, Qian J, Ge GL, *et al.* Multiscale reconfiguration induced highly saturated poling in lead-free piezoceramics for giant energy conversion. *Nat Commun* 2024, **15**: 2560.

[231] Hua Y, Qian J, Yang YX, *et al.* Broad Temperature Plateau for High Piezoelectric Coefficient by Embedding PNRs in Singe-Phase KNN-Based Ceramics. *Adv Funct Mater* 2024, **35**: 2414348.

[232] Nguyen DT, Meyers C, Yee TD, *et al.* 3D-Printed Transparent Glass. *Adv Mater* 2017, **29**: 1701181.

[233] Cheng ZL, Ye F, Liu YS, *et al.* Mechanical and dielectric properties of porous and wave-transparent Si_3N_4-Si_3N_4 composite ceramics fabricated by 3D printing combined with chemical vapor infiltration. *J Adv Ceram* 2019, **8**: 399-407.

[234] Cooperstein I, Indukuri S, Bouketov A, *et al.* 3D Printing of Micrometer-Sized Transparent Ceramics with On-Demand Optical-Gain Properties. *Adv Mater* 2020, **32**: e2001675.

[235] Zheng K, Quan Y, Ma WG, *et al.* 3D Printing High-Performance Piezoelectric Ceramic with Complex Structure for Ultrasonic Array Transducer. *Adv Mater* 2025: e14520.